

**Determination of the photopeak detection efficiency of a  
HPGe detector, for volume sources, via Monte Carlo  
simulations**

**By**

***Raphael Wesley Damon***

Dissertation submitted in fulfilment of the requirements for the Master of  
Science Degree in Physics at the University of the Western Cape



**Supervisors: Prof. R. Lindsay and Dr. R.T. Newman**

## List of Figures

Figure 1.1:	$^{40}\text{K}$ decay series	5
Figure 1.2:	$^{238}\text{U}$ decay series	6
Figure 1.3:	$^{232}\text{Th}$ decay series	7
Figure 1.4:	The process of photoelectric absorption	8
Figure 1.5:	Photoelectric cross – section for germanium	10
Figure 1.6:	The process of Compton scattering	12
Figure 1.7:	The process of pair production/annihilation	16
Figure 1.8:	Interaction process of photons with matter	17
Figure 1.9:	Point source located along the axis of a right circular cylindrical detector, illustrating the angle subtended with detector at a distant d	24
Figure 2.1:	Cross – section diagram of HPGe detector with liquid nitrogen reservoir	32
Figure 2.2:	A photograph of the HPGe detector with accompanying lead castle used by the ERL	33
Figure 2.3:	A photograph of the top view of the HPGe detector with built – in preamplifier. The lead castle and copper lining are clearly visible	33
Figure 2.4:	HPGe detector with accompanying lead castle and data acquisition system at iThemba LABS' <b>E</b> nvironmental <b>R</b> adioactivity <b>L</b> aboratory (ERL)	34
Figure 2.5:	Schematic of electronic setup	34
Figure 2.6:	Cross – section view of germanium detector chamber	36
Figure 2.7:	A picture of the Marinelli beaker used in this work showing its dimensions	39
Figure 2.8:	Top view of HPGe detector with and without Marinelli beaker	40

Figure 2.9: Sand sample sealed with copper disk and silicon in Marinelli beaker	41
Figure 2.10: Spectrum of vineyard soil sample used to investigate the effect of coincidence summing on photopeak efficiency	43
Figure 2.11: Spectrum of 400 ml beach sand sample in Marinelli beaker used to investigate the effect of volume on photopeak efficiency	44
Figure 2.12: Spectrum of 1000 ml beach sand sample in Marinelli beaker used to investigate the effect of volume on photopeak efficiency	44
Figure 2.13: Spectrum of liquid standard source containing the radionuclides $^{60}\text{Co}$ , $^{137}\text{Cs}$ and $^{152}\text{Eu}$	45
Figure 2.14: Spectrum of 1000 ml tap water sample used for background correction	46
Figure 2.15: Spectrum of 1 litre KCl sample in Marinelli beaker	46
Figure 3.1: Schematic representation of radiation transport in Monte Carlo simulations. All processes are based on equations and all decisions are based on random numbers and cross – section tables	51
Figure 3.2: The energy deposited ( $E_{\text{dep}}$ ) in a cell calculated by tally f8	54
Figure 3.3: Schematic of geometry used in intercomparison exercise	55
Figure 3.4: Improvement of absolute efficiency with nsp	57
Figure 3.5: Spectra of 662 keV point source in the centre of 5 cm germanium sphere, showing the statistical fluctuation for MCNPX when 10 million and 100000 histories are simulated	58
Figure 3.6: MCNPX simulated spectra for a 662 keV point source in germanium spheres of different radii	59
Figure 3.7: Flowchart of C++ program	61
Figure 3.8: Coordinates of photons as they are randomly transported through a 1 cm germanium sphere.	62

Figure 3.9: Simulated C++ spectra for a 662 keV point source in germanium spheres of different radii	63
Figure 3.10: Fitted curve to the linear attenuation coefficients obtained from the NIST mass attenuation coefficients for germanium, as function of photon energy (MeV)	65
Figure 3.11: Plot of PE cross – section for Ge in the energy range of interest	67
Figure 3.12: Ratio of the cross – section values to determine scattering probability	67
Figure 3.13: Absolute efficiency curves for $^{152}\text{Eu}$ point and $^{137}\text{Cs}$ source in a germanium sphere of radius in 5 cm	69
Figure 3.14: Ratio of absolute detection efficiency values of C++ and MCNPX simulations	70
Figure 3.15: Spectra showing the larger number of Compton events in MCNPX	71
Figure 3.16: Schematic of close geometry used in simulations	72
Figure 3.17: Normalised pulse height distribution as calculated in MCNPX (section 3.1.4) for the energy (2202.9 keV) of the radionuclide $^{214}\text{Bi}$ , from the decay series of $^{238}\text{U}$ , in a generic soil sample of density $1.2 \text{ g.cm}^{-3}$ in a 1 litre Marinelli beaker	75
Figure 3.18: Schematic of Marinelli beaker illustrating different filling heights	76
Figure 3.19: Simulated spectrum at 1460.8 keV for 400 ml KCl sample in Marinelli beaker illustrating the double and single escape peaks	77
Figure 3.20: Simulated spectrum at 1460.8 keV for 1000 ml KCl sample in Marinelli beaker illustrating the double and single escape peaks	77

Figure 4.1:	Flowchart illustrating the absolute photopeak efficiency determination procedure	79
Figure 4.2:	Fit to the relative efficiency data as determined from the lines associated with the decay series of $^{238}\text{U}$	80
Figure 4.3:	Relative efficiency curve of $^{238}\text{U} + ^{232}\text{Th}$ showing its parameters	81
Figure 4.4:	Location of peaks in soil sample for the radionuclides $^{238}\text{U}$ , $^{232}\text{Th}$ and $^{40}\text{K}$	83
Figure 4.5:	Absolute efficiency curve of soil sample showing its parameters	83
Figure 4.6:	Relative efficiency curve as a function of volume for beach sand sample	85
Figure 4.7:	Absolute efficiency curves for the natural gamma energies at different volumes	86
Figure 4.8:	Absolute efficiency curve for KCl standard as function of volume	88
Figure 4.9:	The measured absolute efficiency curve for $^{40}\text{K}$ standard at different densities	89
Figure 4.10:	Location of peaks in liquid standard that were used in efficiency determination	90
Figure 4.11:	Absolute efficiency curve fitted through experimental values measured using the liquid standard source. The data points are associated with the decay of $^{60}\text{Co}$ , $^{137}\text{Cs}$ and $^{152}\text{Eu}$	93
Figure 5.1:	Absolute photopeak efficiency curve showing the turnover region. The data points are associated with the decay of $^{60}\text{Co}$ , $^{137}\text{Cs}$ and $^{152}\text{Eu}$	94
Figure 5.2:	Relative photopeak efficiency curve with respect to the 662 keV efficiency value	95
Figure 5.3:	Simplified decay scheme for $^{152}\text{Eu}$	98

Figure 5.4:	Sum peaks in the liquid standard source spectrum due to coincidence summing	99
Figure 5.5:	Ratio of experimental to simulated relative photopeak efficiency values	101
Figure 5.6:	Absolute efficiency curves for 1 litre liquid source in Marinelli beaker showing the decrease in efficiency as the dead layer of the detector crystal increases	104
Figure 5.7:	Ratio of experimental to simulated efficiency values for the different detector crystal dead layers	104
Figure 5.8:	Absolute efficiency curves for 1 litre standard liquid source in Marinelli beaker for different detector core dimensions	106
Figure 5.9:	Absolute photopeak efficiency curve as function of volume for standard KCl sample	107
Figure 5.10:	Absolute photopeak efficiency curves for $^{40}\text{K}$ standards as function of density	109
Figure 5.11:	Relative efficiency curves at 1460.8 keV with respect to the efficiency value at $0.66 \text{ g.cm}^{-3}$	110
Figure 5.12:	Relative percentage drop in efficiency as function of density for the $^{40}\text{K}$ standards	111
Figure 5.13:	Absolute photopeak efficiency curves showing the turnover region. The data points are associated with the decay of $^{238}\text{U}$ , $^{232}\text{Th}$ and $^{40}\text{K}$	112
Figure 5.14:	Relative photopeak efficiency curve with respect to the 1460.8 keV efficiency value	113
Figure 5.15:	Peaks in soil sample spectrum that show evidence of coincidence summing	115
Figure 5.16:	Ratio of simulated to experimental relative photopeak efficiency values	116
Figure 5.17:	Relative photopeak efficiency curve at 1460.8 keV as a function of volume for beach sand sample	119

Figure 5.18: Absolute photopeak efficiency curves for 500 ml beach sand sample in Marinelli beaker	120
Figure 5.19: Absolute photopeak efficiency curves for 800 ml beach sand sample in Marinelli beaker	121
Figure 5.20: Absolute photopeak efficiency curves for 1000 ml beach sand sample in Marinelli beaker	121
Figure 5.21: Absolute efficiency curves for soil sample when there is 15 % moisture in the volume sample	122
Figure 5.22: Absolute efficiency curves for sand sample when there is 15 % moisture in the volume sample	123
Figure 5.23: Absolute efficiency curves for generic soil 1 sample and when there is a change of one element (Al to Pb) in its composition	125
Figure 5.24: Absolute efficiency curves for generic soil samples 1 and 2	125
Figure 5.25: Absolute efficiency curve for generic soil sample 1, when Al is changed to Pb, and generic soil sample 2	126
Figure 5.26: Ratio of the efficiency values of the absolute photopeak efficiency curves for the different generic soil compositions	128
Figure A1: Measured efficiency curves for liquid sources in a 1 litre Marinelli beaker	153
Figure A2: Results of the efficiency transfer for the point sources located at 2cm, 5 cm, and 20 cm from the detector window	155
Figure A3: Results of the efficiency transfer for the cylindrical sources	157

## List of Tables

Table 2.1:	Dimensions of ERL HPGe detector	37
Table 2.2:	Data recorded of soil and sand samples used in this study	41
Table 2.3:	Masses of materials and KCl used in study	42
Table 2.4:	Sample reference data from ERL sample database for samples used in this study	47
Table 3.1:	Specifications of Computer and Operating System used for this study	56
Table 3.2:	Optimal parameters used in equation 3.2 to predict linear attenuation coefficients	65
Table 3.3:	Parameters used to determine scattering probability	68
Table 3.4:	Comparison between absolute detection efficiency values of C++ and MCNPX simulations of $\gamma$ – rays from a $^{152}\text{Eu}$ and $^{137}\text{Cs}$ point source located at the centre of a germanium sphere of radius 5 cm	69
Table 3.5:	Dimensions of HPGe detector used in simulations	73
Table 3.6:	Dimensions of Marinelli beaker used in simulations	73
Table 3.7:	Composition of generic soil 1 used in simulations	74
Table 3.8:	Composition of generic soil 2 used in simulations	74
Table 4.1:	Some gamma – ray energies of naturally occurring radionuclides in soil	82
Table 4.2:	Summary of data on beach sand samples at different volumes	84
Table 4.3:	The natural gamma lines and absolute photopeak efficiencies for different volumes	86
Table 4.4:	Absolute efficiency and filling heights for KCl standard at different volumes	88
Table 4.5:	Absolute efficiency values for $^{40}\text{K}$ standards at different densities	89



Table 4.6:	$\gamma$ – ray energies and corrected activity concentration values for the decay of radionuclides in the standard liquid source	91
Table 4.7:	Associated branching ratios of radionuclides and photopeak efficiencies obtained using equation 2.1	92
Table 5.1:	Combinations of gamma – rays (keV) that undergo coincidence summing	100
Table 5.2:	Detector dimensions for the different dead layers	103
Table 5.3:	Dimensions of detector with core increases by 10 % of its original size	105
Table 5.4:	Absolute photopeak efficiencies and filling heights for KCl sample	108
Table 5.5:	Absolute photopeak efficiencies calculated with equation 5.1 and parameters	110
Table 5.6:	Combination of gamma – rays (keV) that undergo coincidence summing in $^{238}\text{U}$ series	115
Table 5.7:	Combination of gamma – rays (keV) that undergo coincidence summing in $^{232}\text{Th}$ series	116
Table 5.8:	The natural gamma – ray energies simulated at different volumes for beach sand sample	120
Table 5.9:	The effective atomic numbers calculated from equation 5.2 for the generic soils and KCl used in this study	127

## Table of Contents

### Chapter 1

Introduction	1
1.1 Decay of nuclei and origin of gamma – rays in the environment	2
1.2 Interaction of gamma – rays with matter	8
1.2.1 Photoelectric Absorption	8
1.2.2 Compton Scattering and the Conservation Laws	11
1.2.3 Pair Production	16
1.2.4 Attenuation of gamma – rays in Medium	18
1.2.5 Detecting gamma – rays	21
1.3 Monte Carlo Methods	25
1.4 Examples of Monte Carlo simulations of gamma – ray interactions in detectors	26
1.5 Motivation for this study	28
1.6 Aim and Objectives of study	30
1.7 Thesis outline	31

### Chapter 2

Experimental Aspects	32
2.1 HPGe detector system	32
2.1.1 Detector specifications	36
2.1.2 Energy Calibration	37
2.1.3 Detector efficiency determination	38
2.2 Sample preparation	39
2.2.1 Soil and sand samples	40
2.2.2 KCl samples	42
2.3 Measurements	43

### Chapter 3

Simulations	48
3.1 MCNPX	48
3.1.1 History of MCNPX	48
3.1.2 MCNPX's method for solving R – T problems	50
3.1.3 Physics models used in MCNPX for this study	52
3.1.4 Pulse – Height Estimator	53
3.2 Intercomparison exercise	55
3.2.1 Geometry and physical properties	55
3.2.2 MCNPX approach	56
3.2.3 C++ approach	59
3.2.3.1 Assumptions and Simplifications	59
3.2.3.2 The Conceptual Model	60
3.2.3.3 Important Physics Processes considered in simulations	63
3.2.3.4 Path length	63

3.2.3.5 Probability of scattering	66
3.2.3.6 Intercomparison results and discussion	68
3.3 ERL Marinelli geometry	72
3.3.1 MCNPX input specifications	72
3.3.2 Soil and sand	74
3.3.3 KCl	76
<b>Chapter 4</b>	
Derivation of experimental results	78
4.1 Soil and sand measurements	78
4.1.1 Absolute photopeak efficiency	78
4.1.2 Volume effect	84
4.2 KCl measurements	87
4.2.1 Volume effect	87
4.2.2 Density effect	89
4.3 Liquid source	90
4.3.1 Absolute photopeak efficiency - CSIR standard liquid source	90
<b>Chapter 5</b>	
Results and Discussion	94
5.1.1 Liquid source	94
5.1.2 Sensitivity exercise	102
5.1.2.1 Dead layer of detector crystal	102
5.1.2.2 Core of detector crystal	105
5.2 KCl samples	106
5.2.1 Volume effect	106
5.2.2 Density effect	109
5.3 Soil and Sand samples	112
5.3.1 Coincidence Summing effect	112
5.3.2 Volume effect	118
5.3.3 Sensitivity exercise	122
5.3.3.1 Moisture in volume source	122
5.4 Z effect	124
<b>Chapter 6</b>	
Summary and Outlook	129
6.1 Summary	129
6.2 Outlook	133
<b>Appendices</b>	
Appendix A – MCNPX input file for intercomparison exercise	135
Appendix B – MCNPX input files for Marinelli geometry	136
1.0 litre soil sample	136
0.4 litre soil sample	140
Appendix C – C++ source code	144

Appendix D – Coincidence summing corrections	154
Appendix E – Efficiency transfer Method	155
E.1 Reference point source	155
E.2 Cylindrical samples	157
<b>References</b>	<b>159</b>

**Declaration:**

I, the undersigned, declare that the work contained herein is my own original work and has not previously in its entirety or in part been submitted at any university for a degree.



Signature: .....

Date: **15 July 2005**.....

## **Acknowledgements**

Thanks be to **God** for giving me the strength, knowledge and wisdom to succeed.

I am truly thankful to the following people for their contribution towards making this thesis possible:

To **my parents and family** for allowing me the opportunity to fulfil my dreams and ambitions,

**Prof. Robbie Lindsay** (University of the Western Cape), supervisor, for his continuous guidance and support throughout the years of my studies,

**Dr. Richard T. Newman** (iThemba LABS), supervisor, for his valuable guidance and support throughout this study,

**Prof. Rob J. de Meijer** (Kernfysisch Versneller Instituut), for his sound advice and the knowledge that he has imparted towards this study,

To **my friends** of the **E**nvironmental **R**adioactivity **L**aboratory (ERL) group; **Angelo Joseph, Wilcot Speelman, Tiro Modisane** and **Pogiso Maine** for their moral support and the data that they have provided for this study,

**UWC Physics Department, iThemba LABS** and the **NRF** for both financial and moral support over the years of my study,

And finally but not least, thanks to **my friends** and those that I have come into contact with over the years for their constant motivation.

# Determination of the photopeak detection efficiency of a HPGe detector, for volume sources, via Monte Carlo simulations

*Raphael Wesley Damon*

Department of Physics, University of the Western Cape, P/Bag 17, Bellville  
7535, July 2005

## **Abstract**

The Environmental Radioactivity Laboratory (ERL) at iThemba LABS undertakes experimental work using a high purity germanium (HPGe) detector for laboratory measurements. In this study the Monte Carlo transport code, MCNPX, which is a general-purpose Monte Carlo N – Particle code that extends the capabilities of the MCNP code, developed at the Los Alamos National Laboratory in New Mexico, was used. The study considers how various parameters such as (1) coincidence summing, (2) volume, (3) atomic number (Z) and (4) density, affects the absolute photopeak efficiency of the ERL's HPGe detector in a close geometry (Marinelli beaker) for soil, sand, KCl and liquid samples. The results from these simulations are presented here, together with an intercomparison exercise of two MC codes (MCNPX and a C++ program developed for this study) that determine the energy deposition of a point source in germanium spheres of radii 1 cm and 5 cm.

A sensitivity analysis on the effect of the detector dimensions (dead layer and core of detector crystal) on the photopeak detection efficiency in a liquid sample and the effect of moisture content on the photopeak detection efficiency in sand and soil samples, was also carried out. This study has shown evidence that the dead layer of the ERL HPGe detector may be larger than stated by the manufacturer, possibly due to warming up of the detector crystal. This would result in a decrease in the photopeak efficiency of up to 8

% if the dead layer of the crystal were doubled from its original size of 0.05 cm.

This study shows the need for coincidence summing correction factors for the gamma lines (911.1 keV and 968.1 keV) in the  $^{232}\text{Th}$  series for determining accurate activity concentrations in environmental samples. For the liquid source the gamma lines, 121.8 keV, 244.7 keV, 444.1 keV and 1085.5 keV of the  $^{152}\text{Eu}$  series, together with the 1173.2 keV and 1332.5 keV gamma lines of the  $^{60}\text{Co}$ , are particularly prone to coincidence summing. In the investigation into the effects of density and volume on the photopeak efficiency for the KCl samples, it has been found that the simulated results are in good agreement with experimental data. For the range of sample densities that are dealt with by the ERL it has been found that the drop in photopeak efficiency is less than 5 %. This study shows that the uncertainty of the KCl sample activity measurement due to the effect of different filling volumes in a Marinelli beaker is estimated in the range of 0.6 % per mm and is not expected to vary appreciably with photon energy. In the case of the effect of filling height on the efficiency for the soil sample, it was found that there is a large discrepancy in the trends of the simulated and experimental curves. This discrepancy could be a result of the use of only one sand sample in this study and therefore the homogeneity of the sample has to be investigated. The effect of atomic number has been found to be negligible for the soil and sand compositions for energies above 400 keV, however if the composition of the heavy elements is not properly considered when simulating soil and sand samples, the effect of atomic number on the absolute photopeak efficiency in the low energy (< 400 keV) region can make a 14 % difference.

Keywords: Monte Carlo, MCNPX, photopeak efficiency, Marinelli beaker



# Chapter 1

## Introduction

The use of germanium detectors in high-resolution gamma-ray spectrometry is one of the most widely used procedures for the identification and quantification of unknown gamma-ray emitting radionuclides in environmental samples. It is a non-destructive technique that has the advantage of not requiring laborious sample preparation. This technique however, requires prior knowledge of the photopeak efficiency of the detector in the counting geometry for each photon energy. This is usually obtained by an efficiency calibration using standard radioactive sources of very similar geometrical dimensions, density and chemical composition to the sample that is being studied [Var03]. However in many cases these conditions cannot be fulfilled and standard radioactive samples, even if available, are costly and would need to be renewed, especially when the radionuclides have short half-lives.



One useful way to overcome these difficulties is the use of Monte Carlo simulations, which takes into account the detailed characteristics of the detector and sample, in calculating the photopeak efficiency. This approach however, is limited in its accuracy due to the inaccuracy in the parameters associated with the detector's geometrical dimensions and the material composition of the sample [Gar00]. The accuracy is also affected by the uncertainty in nuclear data and the calculation uncertainties of the MC code [Man01], but these are expected to be as important as the parameters associated with the detector's geometrical dimensions and the material composition of the sample. The physical dimensions provided by suppliers are usually insufficient for accurate efficiency calculations because any slight change in some of these geometrical parameters can cause significant deviations from experimental values.

Several studies of the response of high-resolution  $\gamma$ -ray spectrometers using Monte Carlo calculations have been published. Most of the authors report agreement with experimentally obtained efficiency values within 10% [Deb82, Sán91]. In recent years the simulation techniques have improved, decreasing the errors to about 3% [Dec92, Ove93], except in the low energy range. Monte Carlo studies are seldom discussed for energies below 88 keV. However this energy region is very interesting in environmental studies as several radionuclides of the  $^{238}\text{U}$  and  $^{232}\text{Th}$  series emit  $\gamma$ -rays at these energies [Gar00].

### **1.1 Decay of nuclei and origin of gamma – rays in the environment**

The discovery of high-energy electromagnetic radiation began in Germany in 1895 with the discovery of X-rays by Wilhelm Roentgen, after observing that a zinc sulphide screen glowed when it was placed near a cathode-ray discharge tube. Roentgen found that the radiation that caused the glow was dependent on the electrode materials and the tube voltage. He also found that it was not bent by electric or magnetic fields, and that it could readily penetrate dense matter [Tyk95].

Henri Becquerel discovered natural radioactivity in 1896 in France, when he observed that uranium salts gave off natural radiation that blackened a photographic plate. Marie and Pierre Curie isolated and identified the radioactive elements polonium and radium in 1897. They determined that the phenomena were characteristic of the atomic properties of the element [Tyk95].

In 1899, Ernest Rutherford discovered that 95 % of the radiation was stopped by 0.02 mm of aluminium and 50 % of the remaining radiation was stopped by 5 mm of aluminium or 1.5 mm of copper. Rutherford named these components “alpha ( $\alpha$ )” and “beta ( $\beta$ )” respectively, “beta” being the more penetrating radiation.

These radiations were both deflected by electric and magnetic fields, though in opposite directions, therefore indicating that they carried opposite electric charges.

In 1900, Paul Villard and Henri Becquerel noted that radioactive materials blackened a photographic plate even when the plate was shielded by 20 cm of iron or 2 cm – 3 cm of lead. They also observed that this penetrating radiation was not deflected by magnetic fields. In 1903, Rutherford named this type of radiation “gamma ( $\gamma$ )” and stated “gamma-rays are probably Roentgen-rays”. Thus the three major types of radiation, now known to be  $^4\text{He}$  nuclei, electrons and electro-magnetic radiation from the nucleus, were identified and named after the first three letters of the Greek alphabet:  $\alpha$ ,  $\beta$  and  $\gamma$  [Tyk95].

Nuclei in excited states may decay to a lower state by emitting a photon with an energy equal to the difference between the energies of the initial and final states. The energies (MeV) in the range of the photons emitted in this way from a nucleus, called gamma-rays ( $\gamma$ -rays), are usually much greater than the energies (keV) in the range of photons originating from electronic transitions, called X-rays.

A nucleus in an excited state can also lose its excitation energy by internal conversion. In this process, the excitation energy of the nucleus is transferred into the kinetic energy of one of the inner most atomic electrons, which is ejected from the atom with an energy equal to the energy of the nuclear transition less the ionisation energy of the electron. Internal conversion thus competes with  $\gamma$ -ray emission in the decay of the excited states.

The hole remaining in the electron cloud after the departure of the electron in internal conversion is later filled by one of the outer atomic electrons. This transition is accompanied either by the emission of an X-ray or by the ejection of another electron in a process similar to internal conversion. Electrons originating in this way are called *Auger electrons*.

In nature, most elements are stable and those few that are not (naturally occurring parent radionuclides) have long half-lives and their decay products are also present in nature. The radioactive elements:  $^{238}\text{U}$  ( $T_{1/2} = [4.468 \pm 0.003] \cdot 10^9$  years),  $^{232}\text{Th}$  ( $T_{1/2} = [1.405 \pm 0.006] \cdot 10^{10}$  years) and  $^{40}\text{K}$  ( $T_{1/2} = [1.277 \pm 0.008] \cdot 10^9$  years) are present in rocks that have condensed with the earth 4500 million years ago [Fir96]. These nuclei and their daughters decay either by alpha ( $\alpha$ ), beta ( $\beta$ ) or gamma ( $\gamma$ ) emission, until a stable lighter nucleus is reached. The series of  $\alpha$ ,  $\beta$  and  $\gamma$  decays of the natural radioactive elements are shown in Figures 1.1 – 1.3.

Each decay chain involves the emission of alphas (vertical lines), betas (diagonal lines) and gammas (shaded boxes) in competing modes. The statistical chance that a gamma-ray is emitted per decaying nucleus, the branching ratio, is given in Table 4.1. In the  $^{238}\text{U}$  decay series, radon ( $^{222}\text{Rn}$ ) is the only radionuclide found in the gaseous state and it can therefore emanate naturally from soil. The  $\gamma$ -emitting decay products of  $^{222}\text{Rn}$  are lead ( $^{214}\text{Pb}$ ) and bismuth ( $^{214}\text{Bi}$ ), which are found in radioactive secular equilibrium with radium ( $^{226}\text{Ra}$ ) only if sealed to stop radon from escaping. From these decay products the estimated activity concentration ( $\text{Bq}\cdot\text{kg}^{-1}$ ) of  $^{238}\text{U}$  can be obtained [Cle94].

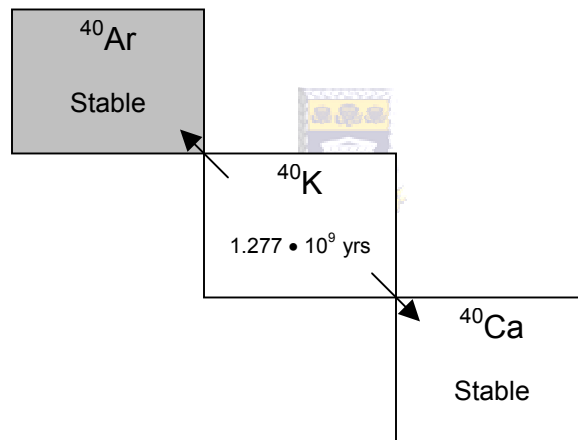


Figure 1.1:  $^{40}\text{K}$  decay series [Tyk95]. The grey boxes represent  $\gamma$  emitting nuclei.

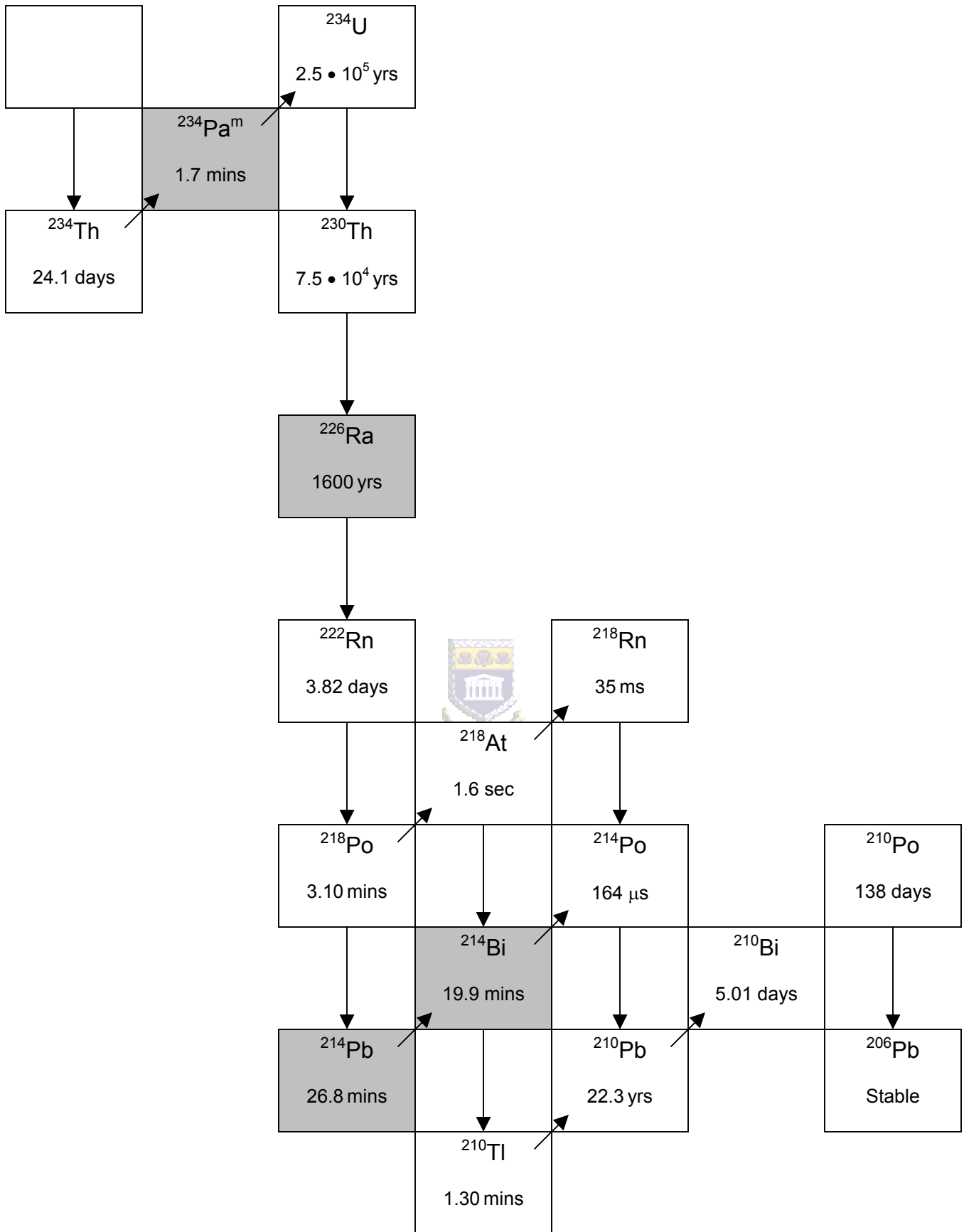


Figure 1.2:  $^{238}\text{U}$  decay series [Tyk95]. The grey boxes represent  $\gamma$  emitting nuclei.

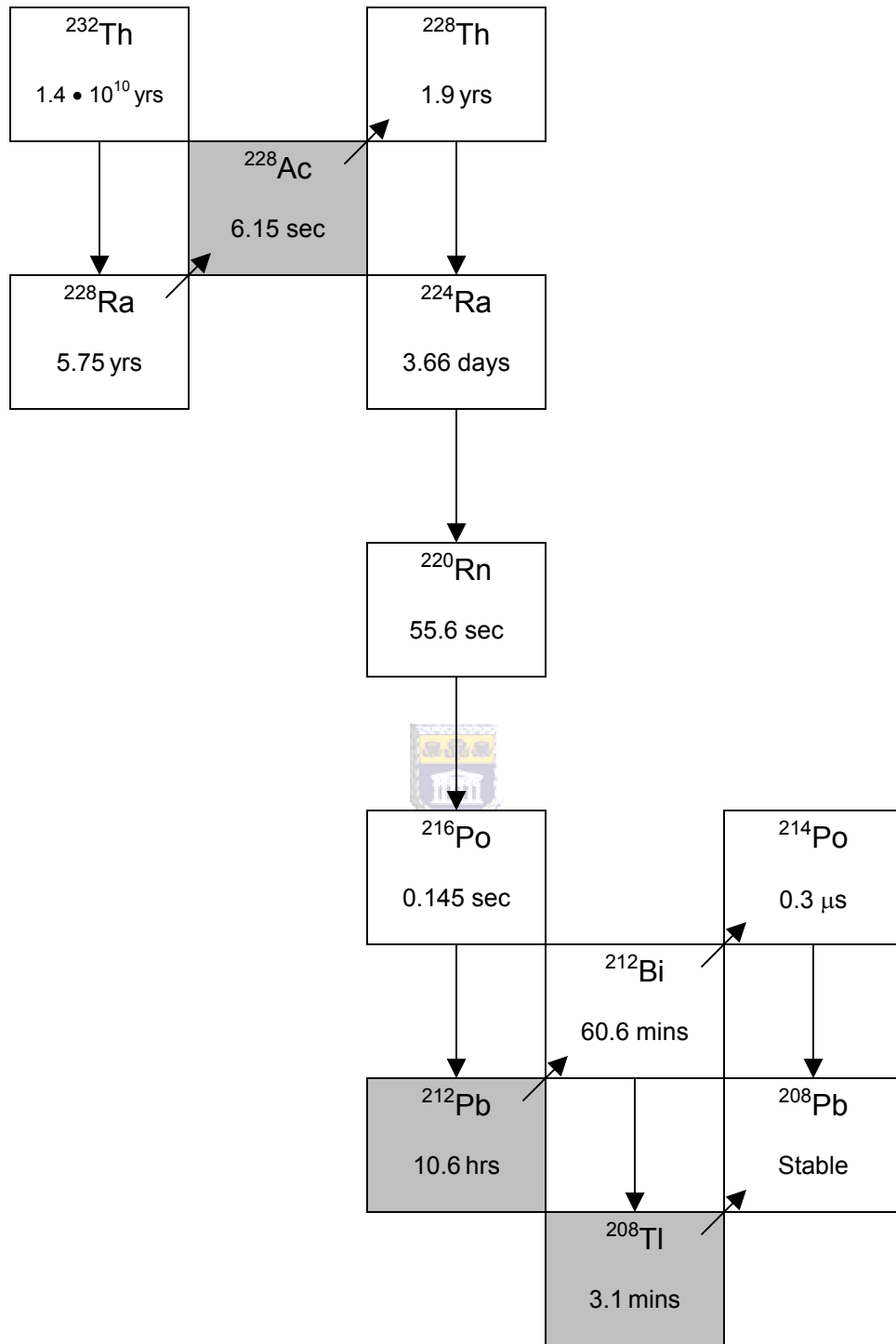


Figure 1.3:  $^{232}\text{Th}$  decay series [Tyk95]. The grey boxes represent  $\gamma$  emitting nuclei.

## 1.2 Interaction of gamma – rays with Matter

The detection of  $\gamma$ -rays depends on the interaction of  $\gamma$ -rays with matter and these interaction mechanisms therefore play an integral part in the work discussed in this thesis.

### 1.2.1 Photoelectric Absorption

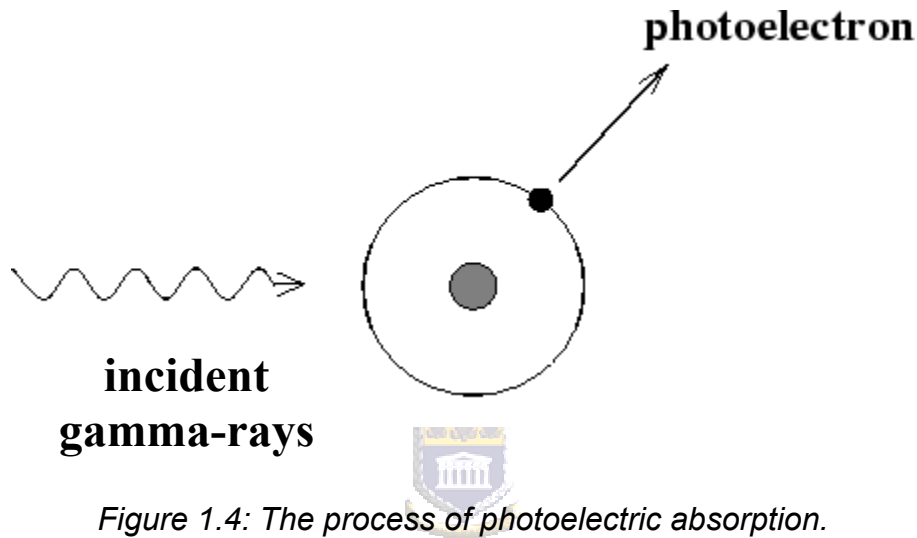


Figure 1.4: The process of photoelectric absorption.

An incident photon cannot be totally absorbed by a free electron, from considerations of the conservation of momentum. However, total absorption can take place if the electron is initially bound to the atom (Figure 1.4). By the recoil of the atom momentum is conserved, hence the most tightly bound electrons have the most likely probability of absorbing an incident photon. It has been found that 80 % of the photoelectric absorption process takes place in the K-shell of the atom (Figure 1.5), provided that the incident photon energy  $E_{\gamma} = h\nu$  exceeds the binding energy of the K-shell.

Due to the fact that the entire atom participates in the process, it may be visualized as an interaction of the primary photon with the electron cloud of the atom (Figure 1.4). The entire photon energy  $E_{\gamma} = h\nu$  is absorbed and an electron is ejected, usually from the K- or L-shell of the atom with energy



$$T_e = E_\gamma - B_e \quad (1.1)$$

where  $B_e$  is the binding energy of the ejected electron. The remainder of the energy appears as characteristic X-rays and Auger electrons from the filling of the vacancy left in the inner shell [Eva55].

The photoelectric process is the predominant mode of interaction for gamma-rays of relatively low energies and is enhanced for materials of high atomic number  $Z$ . There is no single analytic expression that is valid for the probability ( $\sigma$ ) of photoelectric absorption per atom over all ranges of  $E_\gamma$  and  $Z$ , but a first order approximation is

$$\sigma \propto \frac{Z^n}{E_\gamma^{3.5}} \quad (1.2)$$


where the exponent  $n$  varies between 4 and 5 over the energy region of interest. This dependence of the photoelectric absorption probability on the atomic number of the absorber material is the primary reason for the use of high- $Z$  materials (such as lead) in gamma-ray shielding and detectors.

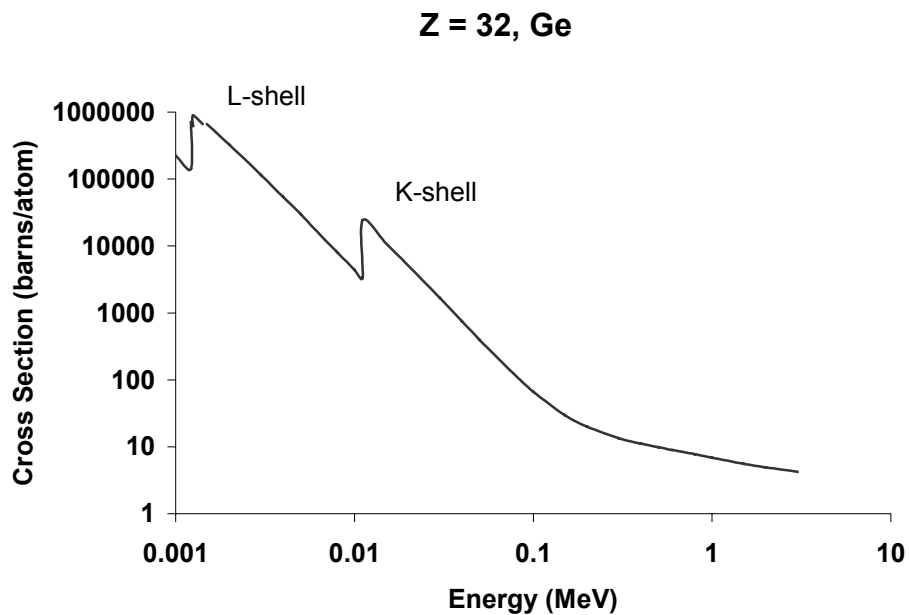


Figure 1.5: Photoelectric cross-section for germanium (data from [Hub82]).

Figure 1.5 shows the photoelectric absorption cross-section for a common  $\gamma$ -ray detector material, germanium. In the low-energy region, discontinuities in the curve or “absorption edges” appear at  $\gamma$ -ray energies which correspond to the binding energies of the electrons in the various shells of the absorber atom. The edge lying highest in energy corresponds to the binding energy of the K-shell electron. For gamma-ray energies slightly above the edge, the photon energy is just sufficient to undergo a photoelectric interaction in which a K-electron is ejected from the atom. For gamma-ray energies slightly below the edge, this process is no longer energetically possible and therefore the interaction probability drops rapidly. Similar absorption edges occur at lower energies for the L, M... electron shells of the atom [Kno79].

## 1.2.2 Compton Scattering and the Conservation Laws

The scattering of very low energy photons  $h\nu \ll m_0c$  by a free electron is described fairly well by the non-relativistic classical theory of J. J. Thomson. This theory however does not hold as  $h\nu$  approaches  $m_0c^2 = 0.511\text{MeV}$ . It was therefore necessary to develop a relativistic theory of scattering. Arthur Compton first introduced this theory of Compton Scattering, in 1922 [Bei95].

When the incident photon has an energy  $h\nu_0$ , which cannot be neglected in comparison with  $m_0c^2$ , a new and complex set of phenomena occurs. The momentum of the photon  $\frac{h\nu_0}{c}$  can no longer be neglected. This incident momentum must be shared between the scattered photon and the electron that is bound to the atom. Except for the case where the scattering angle is zero, the direction of the scattered photon is not parallel to the direction of the incident photon. The scattered photon therefore has a smaller momentum, and hence smaller energy, than the incident photon. The remaining momentum and energy is given to the struck electron.

In this case we consider the struck electron to be at rest and unbound. This simply limits the theory to those cases for which the binding energy of the electron is small when compared with  $h\nu_0$ . In those cases where the photon energy is comparable to the binding energy of the electron, the photoelectric cross-section usually greatly exceeds the Compton scattering cross-section so that Compton scattering is of minor importance.

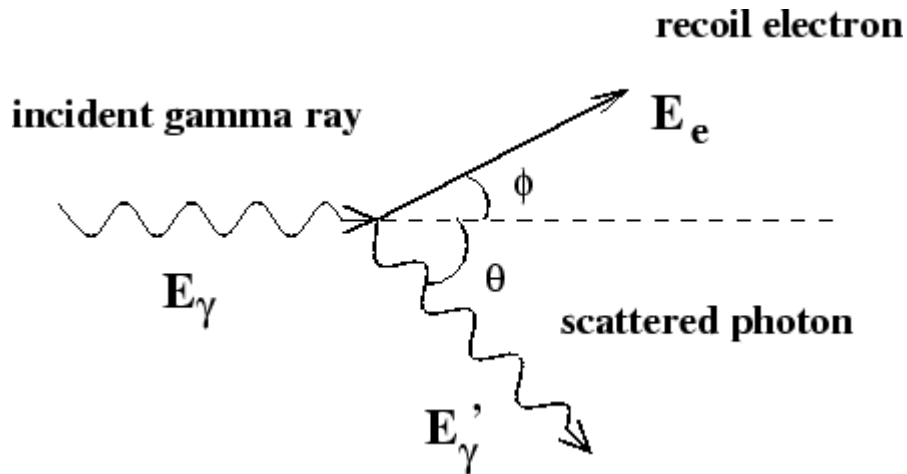


Figure 1.6: The process of Compton scattering.

The energy of the incident photon  $E_\gamma = h\nu_0$  is represented by the dimensionless parameter  $\alpha = \frac{h\nu_0}{m_0c}$ . The incident photon collides with the electron and scatters at an angle  $\theta$  with an energy of  $E'_\gamma$  (Figure 1.6), and the electron recoils at an angle  $\phi$  with a momentum  $p$  and kinetic energy  $T$ . The *scattering plane* is defined by the incident and scattered photon. The momentum normal to this plane is zero; therefore the path of the recoiling electron must also lie in the same plane. The three paths are therefore co-planar, as shown in Figure 1.6. Polarization has no influence on these momentum relationships.

We can now write the relation for conservation of momentum of this process, in the direction of the incident  $\gamma$ -ray as

$$\frac{h\nu_0}{c} = \frac{h\nu' \cos \theta}{c} + p \cos \phi$$

while conservation of momentum normal to this direction gives

$$0 = \frac{h\nu' \sin \theta}{c} - p \sin \phi$$

From the conservation of energy we get the expression

$$h\nu_0 = h\nu' + T$$

or using the relativistic relationship

$$pc = \sqrt{T(T + 2m_0c^2)}.$$

It should be noted that these equations represent the fundamental conservation laws as applied to a two-body collision. They must, therefore, be obeyed regardless of the details of the interaction at the scene of the collision. A number of useful relations follow directly from the above-mentioned equations. These include the following,

*The Compton shift*



$$\frac{c}{\nu'} - \frac{c}{\nu_0} = \lambda' - \lambda_0 = \frac{h(1 - \cos \theta)}{m_0c}$$

*Energy of the scattered photon*

$$h\nu' = \frac{m_0c^2}{1 - \cos \theta + \left(\frac{1}{\alpha}\right)}$$

$$\frac{\nu'}{\nu_0} = \frac{1}{1 + \alpha(1 - \cos \theta)}$$

Note that for a high-energy incident photon,  $\alpha \gg 1$ , the energy of the backscattered photon approaches  $\frac{m_0 c^2}{2} = 0.25 \text{ MeV}$  at  $\theta = 180^\circ$ , while energy of photons scattered at  $\theta = 90^\circ$  approaches  $m_0 c^2 = 0.511 \text{ MeV}$ .

The energy,  $T$ , transferred to the electron when it interacts with the incident photon at an angle  $\theta$  is given by equation 1.3:

$$\begin{aligned}
 T &= h\nu_0 - h\nu' \\
 T &= \frac{h\nu_0 2\alpha \cos^2 \theta}{(1 + 2\alpha)^2 - \alpha^2 \cos^2 \theta} \\
 T &= \frac{h\nu_0 \alpha (1 - \cos \phi)}{1 + \alpha (1 - \cos \phi)} \quad (1.3)
 \end{aligned}$$



The maximum energy that can be transferred,  $T_{\max}$ , to the electron (i.e. Compton edge) is given by:

$$T_{\max} = \frac{h\nu_0}{1 + \left(\frac{1}{2\alpha}\right)}$$

OR

$$h\nu_0 = \frac{1}{2} T_{\max} \left( 1 + \sqrt{\frac{1 + 2m_0 c^2}{T_{\max}}} \right)$$

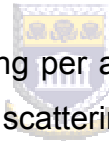
The relationship between the scattered angle  $\phi$  of the electron and the angle  $\theta$  of the scattered photon is given as:

$$\cot \theta = (1 + \alpha) - \frac{\cos \phi}{\sin \phi} = (1 + \alpha) \tan \frac{\phi}{2}$$

The length  $\frac{h}{m_0 c} = 2.426 \times 10^{-12}$  m is the *Compton wavelength*  $\lambda_c$  for an electron. It is equal to the wavelength of a photon whose energy is equal to the rest energy of the electron  $m_0 c^2 = 0.511 \text{ MeV}$ . In the domain of nuclear  $\gamma$ -rays, the Compton shift can be visualized more readily when the incident and scattered photons are described by the energies, rather than by their wavelengths.

$$\frac{1}{h\nu'} - \frac{1}{h\nu_0} = \frac{1}{m_0 c^2} (1 - \cos \theta)$$

The Compton shift in wavelength, in any particular direction, is independent of the energy of the incident photon. In contrast, the Compton shift in energy is very strongly dependent upon  $h\nu_0$ . Low-energy photons are scattered with only a moderate energy change, but high-energy photons undergo a very large change in energy [Eva55].



The probability of Compton scattering per atom of the absorber depends on the number of electrons available as scattering targets, and therefore increases linearly with  $Z$ . The dependence on  $\gamma$ -ray energy generally falls off gradually with increasing energy.

The angular distribution of scattered gamma-rays is predicted by the Klein-Nishina formula for the differential scattering cross-section  $\frac{d\sigma}{d\Omega}$ :

$$\frac{d\sigma}{d\Omega} = r_0^2 \left[ \frac{1}{1 + \alpha (1 - \cos \theta)} \right]^3 \left[ 1 + \cos^2 \frac{\theta}{2} \right] \cdot \left[ 1 + \frac{\alpha^2 (1 - \cos \theta)^2}{(1 + \cos^2 \theta) [1 + \alpha (1 - \cos \theta)]} \right]$$

where  $r_o = \frac{e^2}{4\pi\epsilon_0 mc^2}$  is the classical electron radius. This distribution shows a strong tendency for forward scattering at high gamma-ray energies [Kno79].

### 1.2.3 Pair Production

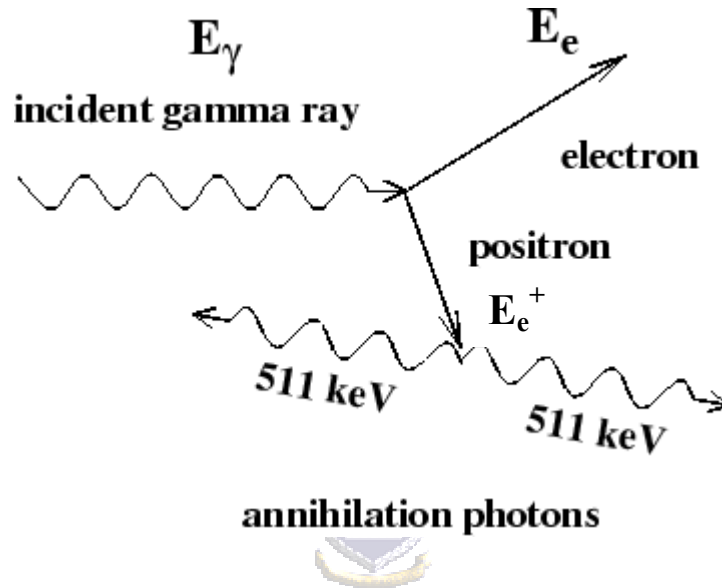


Figure 1.7: The process of pair production/annihilation.

If the gamma-ray energy exceeds twice the rest mass energy of an electron (1.02 MeV), the process of pair production is possible. The probability of this interaction occurring remains zero until the gamma-ray energy equals or exceeds twice the rest mass energy of an electron. In this process the gamma-ray disappears and is replaced by an electron-positron pair. All the excess energy carried by the photon above the 1.02 MeV required to create the pair, goes into kinetic energy shared by the positron ( $T_+$ ) and electron ( $T_-$ ):

$$h\nu_o = \left(T_- + m_o c^2\right) + \left(T_+ + m_o c^2\right).$$



Because the positron will subsequently annihilate after slowing down in the absorbing medium, two annihilation photons of energy 511 keV each are normally produced as secondary products of the interaction (Figure 1.7). These  $\gamma$ -rays can then either be absorbed or escape the crystal. The so-called **escape peaks**, observed in the  $\gamma$ -ray spectra is evidence of this. If one of the 511 keV photons escapes the detector crystal, then a peak is observed at  $E_\gamma - m_0c^2$  (single escape peak). If both escape, then a peak is observed at  $E_\gamma - 2m_0c^2$  (double escape peak). These peaks are evident in Figures 3.19 and 3.20. The process of pair production only becomes important for high-energy  $\gamma$ -rays ( $\geq 2$  MeV).

No simple expression exists for the probability of pair production per nucleus, but its magnitude varies approximately as the square of the absorber atomic number and increases sharply with energy.

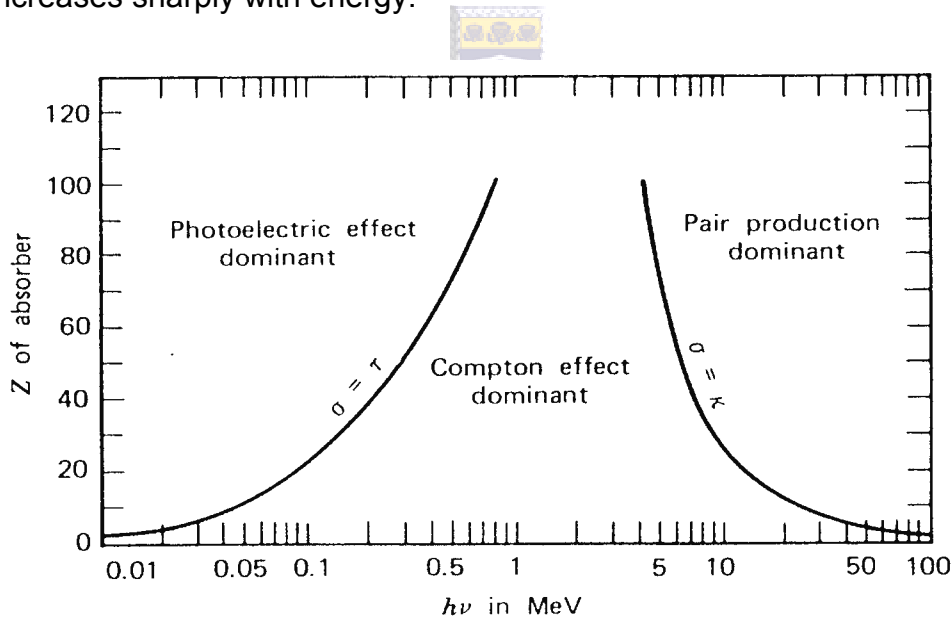


Figure 1.8: Interaction processes of photons with matter [Kra88].

The relative importance of the three processes described, as function of Z and gamma-ray energies is conveniently shown in Figure 1.8. The three areas are thus defined in the figure within which photoelectric absorption, Compton

scattering and pair production each predominate [Kno79]. The importance of photoelectric absorption at energies below 400 keV and the strong Z dependence of this interaction are important in explaining the discrepancies found at lower energies in the simulations described later in thesis.

#### 1.2.4 Attenuation of gamma-rays in a Medium

Gamma-rays have no definite range in a medium; they cannot be stopped completely in any medium unless photoelectric absorption takes place. The intensity of gamma-rays is reduced when it interacts with a medium. The equation that governs the reduction of the intensity is

$$I = I_0 e^{-\mu t} \quad (1.4)$$

where

$I_0$  = Initial gamma-ray intensity of a parallel beam of  $\gamma$ -rays with energy  $E_\gamma$  impinging perpendicular on a medium.

$t$  = medium thickness,

$I$  = gamma-ray intensity of parallel beam of  $\gamma$ -rays with energy  $E_\gamma$  transmitted through a medium of thickness  $t$ ,

$\mu$  = attenuation coefficient.

If the medium thickness is measured in centimetres, then the fraction of a beam of gamma-rays that is absorbed or scattered per unit thickness of the medium is called the **linear attenuation coefficient**,  $\mu_l$ , with dimension,  $\text{cm}^{-1}$ . If the medium

thickness is given in  $\frac{g}{cm^2}$ , then the attenuation coefficient is called **the mass attenuation coefficient**,  $\mu_m$  [Kno79].

The numerical relationship between  $\mu_l$  and  $\mu_m$  is given by the equation

$$\mu_l (cm^{-1}) = \mu_m \left( \frac{cm^2}{g} \right) \times \rho \left( \frac{g}{cm^3} \right) \quad (1.5)$$

where  $\rho$  is the density of the medium in  $g.cm^{-3}$ .

Let us designate the number of photons per square centimetre per second as  $\varphi$ . The quantity  $\varphi$  is called the flux ( $cm^{-2}.s^{-1}$ ) of the incident photons. The fraction of incident energy locally attenuated per centimetre is called the **energy-attenuation coefficient**,  $\mu_{en}$ . The mass energy-attenuation coefficient,  $\frac{\mu_{en}}{\rho}$ , is obtained by dividing the energy-attenuation coefficient by the density. The product  $\frac{\mu_{en}}{\rho}$ ,  $\varphi$  and E gives the energy locally attenuated per unit mass per unit time:

$$E_{abs} = \frac{\mu_{en}}{\rho} \cdot \varphi \cdot E$$

The *total attenuation coefficient*  $\mu_T$  is the sum of the attenuation coefficients of each of the interaction processes in the medium. The equation for  $\mu_T$  is given as

$$\mu_T = \mu_{PE} + \mu_{CS} + \mu_{PP} \quad (1.6)$$

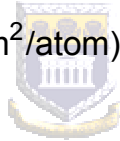
where PE, PP, and CS indicate photoelectric absorption, pair production, and Compton scattering, respectively [Kno79].

The average distance travelled by a gamma-ray photon in the medium before an interaction occurs is defined as the mean free path,  $\lambda$ , given as

$$\lambda = \frac{\int_0^{\infty} x e^{-\mu x} dx}{\int_0^{\infty} e^{-\mu x} dx} = \frac{1}{\mu}$$

Another parameter that is also useful in gamma interactions is the microscopic cross-section,  $\sigma$ , of the medium. It is defined as the fraction of an incident gamma-ray beam that is attenuated by a single atom [Kno79]. The unit for cross-section is the *barn*; (1 barn =  $10^{-24}$  cm<sup>2</sup>) and is symbolized by  $\sigma$ , while the linear attenuation coefficient is often called the macroscopic cross-section and is given the symbol  $\Sigma$

$$\Sigma(\text{cm}^{-1}) = \sigma(\text{cm}^2/\text{atom}) \times N(\text{atoms}/\text{cm}^3)$$



where N is the atom density given as

$$N = \frac{\rho N_A}{M}$$

where

$\rho$  = density of the medium

M = gram atomic weight of the medium

$N_A$  = Avogadro's number.

### 1.2.5 Detecting gamma-rays

In principle, all detectors give rise to an output pulse or signal for a quantum of radiation, which interacts within its active volume. Radiation such as  $\gamma$ -rays must first undergo a considerable interaction in the detector crystal before detection is possible. Because photons can travel large distances between interactions, detectors are usually less than 100 percent efficient. It is therefore necessary to have a precise value for the detector efficiency to relate the number of pulses counted to the number of photons incident on the detector.

Two efficiencies are usually defined:

*Absolute efficiency:*

$$\epsilon_{\text{ABS}} = \frac{\text{no. of pulses recorded in photopeak}}{\text{no. of radiation quanta emitted by source}}$$

The absolute efficiency is dependent not only on detector properties but also on the details of the counting geometry (i.e. distance from the source to detector).

*Intrinsic efficiency:*

$$\epsilon_{\text{INT}} = \frac{\text{no. of pulses recorded in photopeak}}{\text{no. of radiation quanta incident on detector}}$$

The intrinsic efficiency does not include the solid angle subtended by the detector as an implicit factor.

For isotropic sources the two efficiencies are simply related by

$$\epsilon_{\text{INT}} = \epsilon_{\text{ABS}} \times \frac{4\pi}{\Omega}$$

where  $\Omega$  is the solid angle of the detector seen from the actual source position. The intrinsic efficiency of a detector is a detector property and independent of the geometry, therefore it is much more convenient to tabulate values for intrinsic efficiencies. The intrinsic efficiency of a detector usually depends primarily on the detector material, the radiation energy, and the physical thickness of the detector in the direction of the incident radiation.

Counting efficiencies are also categorised by the nature of the event recorded. The *total efficiencies* in the detector include all interaction events, irrespective of their energy deposition. In terms of a pulse height distribution the entire area under the spectrum is a measure of the total efficiency. The *photopeak efficiency*, however, assumes that only those interactions, which deposit the full energy of the incident photon, are counted. In a pulse height distribution, a peak is normally evidence of these full-energy events.

The number of full-energy events can be obtained by integrating the total area under the peak. The total and peak efficiencies are related by the “peak-to-total” ratio  $r = \frac{\epsilon_{\text{Peak}}}{\epsilon_{\text{Total}}}$ . It is often preferable from an experimental standpoint to use only the *peak efficiencies*, because the number of full-energy events can be attributed to photoelectric absorption.

The most common type of efficiency tabulated for gamma-ray detectors are the “*intrinsic peak efficiency*”. A detector with known efficiency can be used to measure the absolute activity of a radioactive source. Let us assume a detector with an *intrinsic peak efficiency*  $\epsilon_{\text{ip}}$  records  $N$  events under the photopeak in the detector spectrum. For simplicity we assume that the source emits radiation isotropically at a rate of  $S$  photons per unit of time, and that no attenuation takes

place between the source and the detector. Then from the definition of intrinsic peak efficiency, the number of photons  $N$  in the photopeak over a period,  $\Delta T$ , is

$$N = S \varepsilon_{ip} \cdot \frac{\Omega}{4\pi} \cdot \Delta T$$

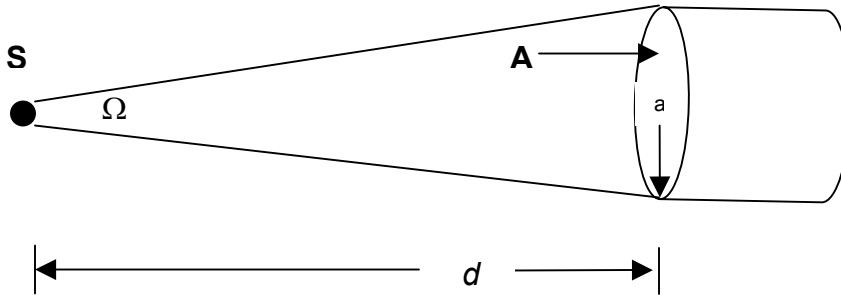
The solid angle subtended by the detector at the source position is defined by an integral over a detector surface, which faces a source,

$$\Omega = \int_A \frac{\cos \alpha}{r^2} dA$$

where  $r$  represents the distance between the source and a surface element  $dA$ , and  $\alpha$  is the angle between its normal and the source direction. If the volume of the source is not negligible, then a second integration must be carried out over all volume elements of the source. For the common case of a point source located along the axis of a right circular cylindrical detector,  $\Omega$  is given by:

$$\Omega = 2\pi \left( 1 - \frac{d}{\sqrt{d^2 + a^2}} \right)$$

where the source-detector distance ( $d$ ) and the detector radius ( $a$ ) are shown in Figure 1.9:



*Figure 1.9: Point source located along the axis of a right circular cylindrical detector, illustrating the angle subtended with detector at a distant  $d$  [Kno79].*

For  $d \gg a$ , the solid angle reduces to the ratio of the detector plane frontal area  $A$  visible at the source to the square of the distance

$$\Omega \cong \frac{A}{d^2} = \frac{\pi a^2}{d^2}$$

Published values for  $\Omega$  can sometimes be found for more complicated geometries involving off-axis or volumetric sources, or detectors with more complex shapes [Kno79].



### **1.3 Monte Carlo Methods**

**M**onte **C**arlo (MC) methods are used to model random processes and only in the past several decades has the technique gained the status of a developed numerical method capable of addressing the most complex applications. The name “Monte Carlo” was devised by Metropolis during the Manhattan Project (a collaboration between the USA, UK and Canadian governments to development the atomic bomb) of World War II [Met56], because of the similarity of statistical simulation to games of chance, and because the capital of Monaco was a centre for gambling and similar activities. The MC method is now used routinely in various fields, from the simulation of complex physical phenomena such as radiation transport in the earth's atmosphere and the simulation of the difficult to understand sub-nuclear processes in high-energy physics experiments, to the ordinary, such as the simulation of a Bingo game [WWW01].

Statistical simulation methods may be compared to predictable numerical discrimination methods, which typically are applied to ordinary or partial differential equations that describe some underlying physical or mathematical system. In many applications of MC, the physical process is simulated directly, and there is no need to even write down the differential equations that describes the behaviour of the system. The only condition is that the physical (or mathematical) system be described by **p**robability **d**ensity **f**unctions (pdfs). Once the pdfs are known, the Monte Carlo simulation can proceed by random sampling from the pdfs [WWW02]. Many simulations are then performed (multiple “histories”) and the desired result is taken as an average over the number of observations (which may be a single observation or perhaps millions of observations). In many practical applications, one can predict the statistical error (the “variance”) in this average result, and hence an estimate of the number of MC trials that are needed to achieve a given error.

Assuming that the progress of the physical system can be described by pdfs, then the MC simulation can proceed by sampling from these pdfs, which requires a fast and effective way to generate random numbers uniformly distributed on the interval [0,1]. The outcomes of these random samplings, or histories, must be accumulated or tallied in an appropriate manner to produce the desired result. The essential characteristic of the MC method is the use of random sampling techniques (and perhaps other algebra to manipulate the outcomes) to arrive at a solution of the physical problem.

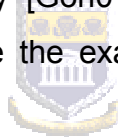
#### **1.4 Examples of Monte Carlo simulations of gamma-ray interactions in detectors**

Modelling codes such as MCNP and MCNPX are used to predict the response of detectors in a wide range of detector-source geometries. The Nuclear Geophysics Division of **K**ernfysisch **V**ersneller **I**nstituut (KVI) has simulated the  $\gamma$ -ray spectra of natural radionuclides for a BGO detector in a borehole geometry using the Monte Carlo code, MCNP [Hen02]. The models that were described in their work are used for various applications such as the calibration and optimisation of the geological core-analyser PHAROS [Rig02] and the assessment of correction factors for experimental conditions occurring in borehole measurements such as non-axial positioning of the detector, presence of casings and borehole diameters [Hen02].

The MCNP code has been used for photopeak efficiency determination for various source-detector geometries, complex source shapes and Marinelli beaker models for a HPGe detector and have yielded results that deviate from experimental data by between 0.2 to 12 % [Ewa01].

The Monte Carlo code GEANT, developed at CERN, was used by Garci-Talavera in a systematic study on the influence of different source configurations on the reliability of MC calculations of the response of Ge detectors in the energy range 46 – 1800 keV. Analysis of the deviations between experimental and calculated results for the different configurations, led to detection of inaccuracies in the description of the detector and source characteristics (density, chemical composition). By reducing these inaccuracies, the deviation was found to be about 4 % from experimental data [Gar00].

The behaviour of highly segmented HPGe detectors was studied, using the Monte Carlo detector simulation tool, GEANT, in conjunction with experimental data. It was found that the simulated detector was more efficient when compared with the actual detector. It was suggested, from a series of simulations, that it was possible that the inner hole of the detector could be larger than specified, thereby explaining the discrepancy [Gon01]. This result indicates a common problem in MC calculations, where the exact dimensions and make-up of the detector is not precisely known.



The GEANT code was used by Laborie to calculate a photopeak efficiency calibration curve and coincidence summing corrections in low-energy gamma-ray spectrometry with well-type HPGe detectors. He reports deviations of less than 10 % from experimental data [Lab00].

The MC simulation package PENELOPE, with a cylindrical geometry tool was used by Garcia-Torano to model volume sources and to calculate the detection efficiency of  $\gamma$ -emitters affected by coincidence summing effects. These efficiencies were then used to calculate correction factors that lead to deviations between experimental and simulated values of less than 3 % [Tor05].

## **1.5 Motivation for this study**

A research collaboration between UWC and the applied radiation group at iThemba LABS has led to the establishment of the **E**nvironmental **R**adioactivity **L**aboratory (ERL), which embarks on research in the field of environmental radioactivity. This research includes radiation monitoring (radon and related source term studies) and applications in the fields of mining and agriculture. These studies involve the measurement of the activity concentrations of radionuclides in liquid ( $\text{Bq.l}^{-1}$ ) and soil ( $\text{Bq.kg}^{-1}$ ) samples, using a sensitive in – situ detector system (MEDUSA) and a high-purity germanium (HPGe) detector.

Monte Carlo simulations can play a role in improving many of the measurements made in the ERL. The ERL routinely measures the activity concentration of anthropogenic radionuclides in water (from ponds on the iThemba LABS site). A programme has also been initiated to measure the concentration of radon in ground water. For these measurements the photopeak detection efficiency is determined as a function of energy by measuring a 1 litre water sample (in a Marinelli geometry) that was spiked with  $^{152}\text{Eu}$ ,  $^{60}\text{Co}$  and  $^{137}\text{Cs}$ . There is however a problem associated with this approach – namely that of coincidence summing. The lifetime of the discrete nuclear levels of nuclei with complex decay schemes ( $^{152}\text{Eu}$ ) are much shorter than the resolving time of the spectrometer system. Therefore, each decay of nucleus will release a number of gamma-rays, and possibly X-rays, and there is a high probability that the detector will detect more than one of these simultaneously. This simultaneous recording of gamma-rays is called coincidence summing. This effect will introduce a systematic error while determining activity concentrations. We hope to assess the magnitude of this effect by carefully comparing experimental and simulated (via MC methods) photopeak efficiencies, in particular for lines associated with the decay of  $^{152}\text{Eu}$  and  $^{60}\text{Co}$ .

The most common type of measurements of the ERL HPGe is that of the activity concentrations of primordial radionuclides in soil and sand. Again a Marinelli geometry is used. In this case the photopeak efficiency is determined by first calculating the relative photopeak efficiency from lines associated with the decay of  $^{238}\text{U}$  and  $^{232}\text{Th}$ . The relative efficiency curve is then set on an absolute scale by a measurement of the absolute efficiency at 1461 keV for a potassium chloride (KCl) sample having the same volume as that of the soil/sand sample in question.

It is known that coincidence summing is also a problem in gamma-ray measurements made in a close-geometry arrangement (as is the case for ERL Marinelli geometry). A further motivation for this study is to attempt to gauge the magnitude of this effect for different gamma-ray lines, by again comparing experimental and simulated results.

Since the density and volume of soil and sand samples measured can vary, the variation of photopeak efficiency with volume and density (at 1461 keV) was studied experimentally. A further motivation for this study was to compare simulations with these experimental values.

On a more general level a motivation for this study is to introduce Monte Carlo simulations as an analytical approach in ERL. In particular, the code MCNPX, which was available at iThemba LABS when this study commenced, was used. The Monte Carlo code, MCNPX, is an extension of the general-purpose **M**onte **C**arlo **N** – **P**article (MCNP) code that can be used for neutron, photon, electron, or coupled neutron/photon/electron transport. MCNPX can also be used to transport 31 additional particles, with the ability to use physics models to calculate interactions for energies beyond tabular data and where data tables are unavailable. It also contains new source, tallying and variance reduction options. Los Alamos National Laboratory in USA developed and continues to improve the MCNPX code.

## **1.6 Aims and Objectives of study**

The aim of this study is to establish the use of computer-based calculations (i.e. MCNPX simulations) in the ERL at iThemba LABS. This study focuses on the simulation of the HPGe photopeak detector efficiency for various environmental and standard samples (liquid and different soil and sand types) in the hope of obtaining answers to questions that arise from experimental work carried out in the ERL. The specific objectives of this work are to study:

- (1) the effect of coincidence summing for primordial and anthropogenic radionuclides;
- (2) the volume effect in close geometry measurements for sand samples;
- (3) the density effect in close geometry measurements for  $^{40}\text{K}$  calibration standards; and
- (4) the Z effect in close geometry measurements for generic soil samples.



## **1.7 Thesis Outline**

In Chapter 2, the experimental aspects such as the HPGe detector system used, sample preparation, and measurements involved in this study are discussed. Chapter 3 is a discussion of the MC simulations done in this study. This chapter includes background into the code, MCNPX, and how it was used to determine the photopeak efficiency for different volume sources. An intercomparison exercise between MCNPX and a C++ program, to determine the energy deposition efficiency is also presented in this chapter. The next two chapters (Chapter 4 and 5) focus on the experimental and simulation results and interpretation of the data, respectively, that are presented in this study. Chapter 5 also contains a sensitivity analysis on the effect of detector crystal parameters (dead layer and core) and moisture (in the volume source) on the photopeak efficiency. Thereafter a summary of findings and conclusions, together with an outlook are given in Chapter 6.



## Chapter 2

### Experimental aspects

#### 2.1 HPGe detector system

The detector used in the Environmental Radiation Laboratory (ERL) at iThemba LABS, is a HPGe with a built-in preamplifier (Figure 2.1). To attenuate cosmic and other outside radiation, a lead castle of approximately 10 cm thick, with a copper lining on the inside to absorb any lead X-rays that are produced, shields the detector (Figures 2.2 and 2.3). The detector system and electronic setup used and assembled by the ERL group, for the analysis of radioactivity in environmental samples is shown in Figures 2.4 and 2.5.

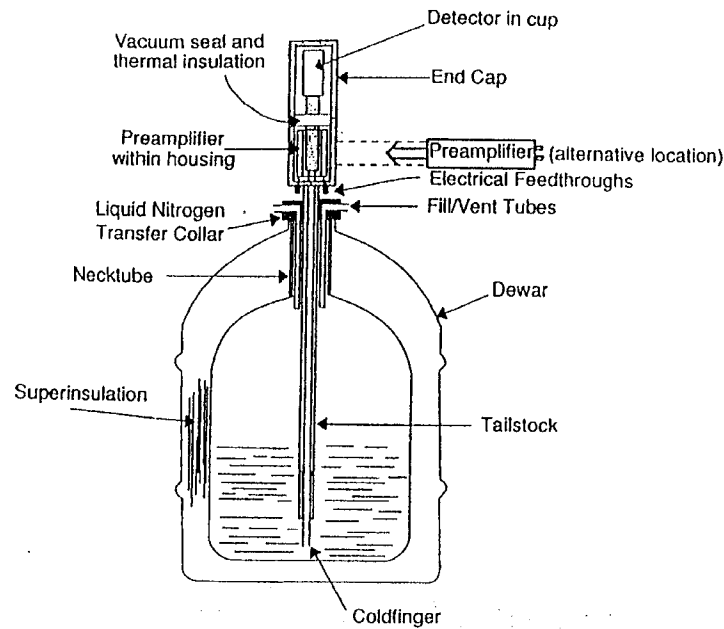


Figure 2.1: Cross-section diagram of HPGe detector with liquid nitrogen reservoir [Gil95].





*Figure 2.2: A photograph of the HPGe detector with accompanying lead castle used by the ERL.*



*Figure 2.3: A photograph of the top view of the HPGe detector with built-in preamplifier. The lead castle and copper lining are clearly visible.*

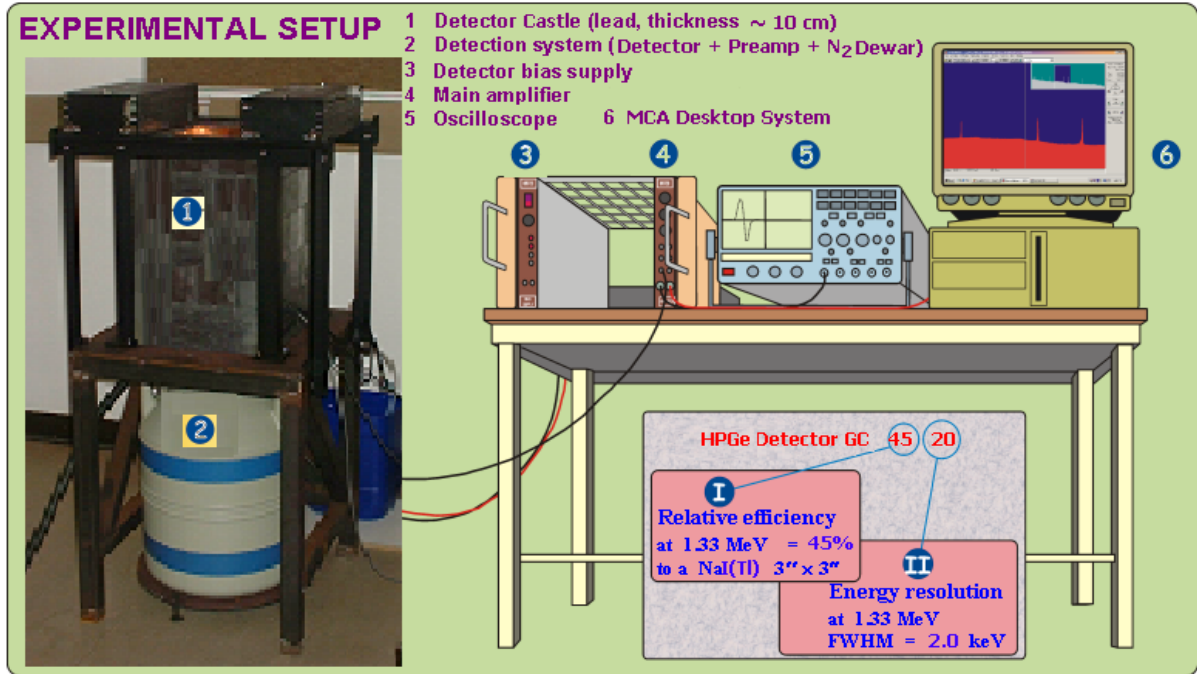


Figure 2.4: HPGe detector with accompanying lead castle and data acquisition system at iThemba LABS' Environmental Radioactivity Laboratory (ERL).

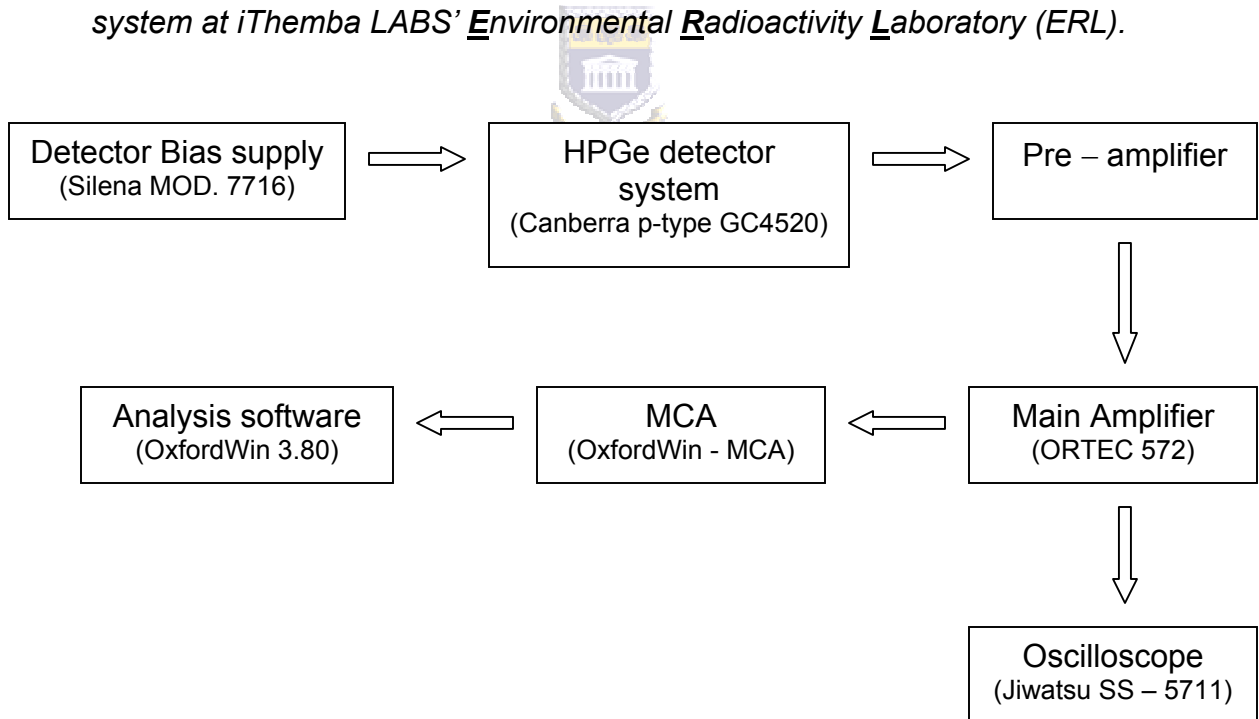


Figure 2.5: Schematic of electronic setup.

A  $\gamma$ -ray is emitted from the sample and enters the detector, where it undergoes a number of interactions resulting in the ionisation of the germanium atoms in the detector crystal. The detector crystal operates under a vacuum and therefore small amounts of moisture, which may leak into the system, could contaminate the crystal. Liquid nitrogen ( $\text{LN}_2$ ) is used to drastically reduce detector thermal noise and to harmlessly freeze any moisture in the system in order to maintain the vacuum. It is therefore very important that the  $\text{LN}_2$  supply is continuously maintained, to prevent the system from warming up, which would cause moisture and short-circuiting of the system, damaging the detector.

The pulse that is produced due to the ionisation is converted into an electronic pulse by the semi-conducting germanium crystal. The electronic pulse is however very weak and is separated from the detector crystal by a preamplifier. The output of the preamplifier occurs as discrete analog pulses, with the amplitude of the pulse corresponding to the energy of the individual  $\gamma$ -rays. These pulses serve as input to an amplifier, which can be used to adjust the peak shape. The unipolar output from the amplifier serves as input to the oscilloscope, which is used while making the amplifier pole-zero adjustment. The pulses from the amplifier are processed by a computer system called a multi-channel analyser (MCA). The analog pulse is converted to digital form by an analog-to-digital converter (ADC).

The ADC signal is stored in the MCA memory, where the digital pulses are counted in specific channels of the MCA, according to the amplitudes of the pulses that reach the ADC. The data acquisition and analysis software used in the ERL, OxfordWin-MCA, consists of 8192 individual channels storing digital values. Each channel records the number of pulses of a given pulse energy.

Before the analysis and data acquisition was done, an energy calibration was performed using reference  $\gamma$ -ray emitting sources [Map05].

### 2.1.1 Detector specifications

The detector used in the ERL, for this study, is a GC 4520 p-type Canberra HPGe detector (Figure 2.6). The specifications provided by the manufacturer for this detector are given in Table 2.1.

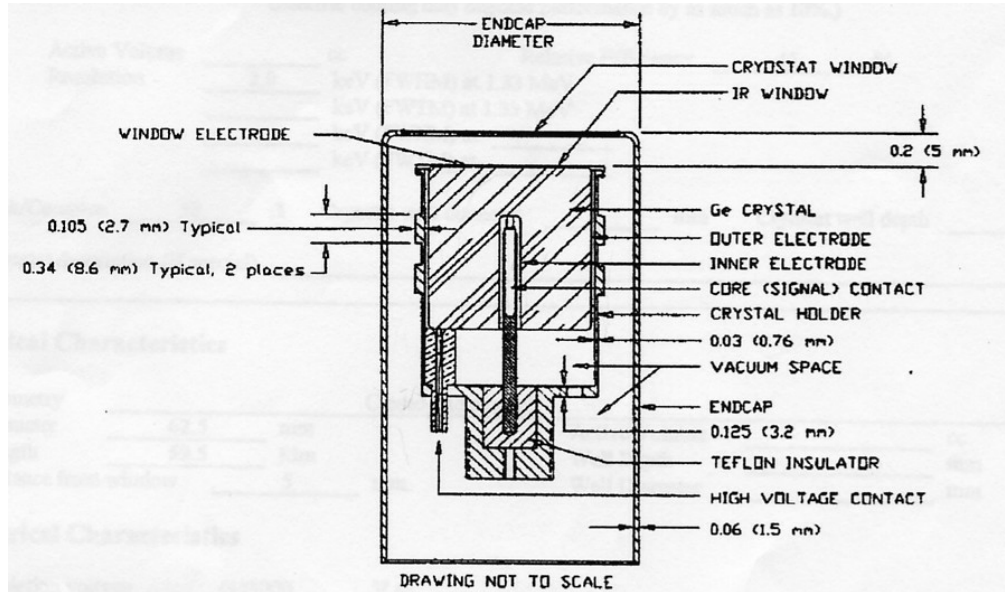


Figure 2.6: Cross-section view of germanium detector chamber [Can99].

Component	Density	Dimension
	g.cm <sup>-3</sup>	
Core diameter	0.000	0.85 cm
Core depth	0.000	4.40 cm
Ge crystal diameter	5.323	6.25 cm
Ge crystal length	5.323	5.95 cm
Ge dead layer	5.323	0.5 mm
Al cap	2.700	0.76 mm
Vacuum	0.000	3.5 mm
Cryostat	2.700	1.5 mm

*Table 2.1: Dimensions of the ERL HPGe detector [Can99].*



### 2.1.2 Energy Calibration

During the energy calibration procedure the HPGe detector system is used to acquire a  $\gamma$ -ray spectrum for a one litre liquid cocktail standard (Figure 2.13) containing the radionuclides,  $^{60}\text{Co}$  (1.907 kBq  $\pm$  2.0 %),  $^{137}\text{Cs}$  (0.661 kBq  $\pm$  2.0 %) and  $^{152}\text{Eu}$  (6.550 kBq  $\pm$  3.0 %) in 0.1 M HCl in a 1 litre Marinelli beaker, that was prepared in July 2002 [Mor02]. The spectrum was then energy calibrated by setting regions of interest (ROI) around a number of peaks of interest (Figure 4.10). The selected peaks are then manually calibrated by entering in the known energies corresponding to the ROI centroids. A linear fit is then used to obtain the energy calibration parameters. The amplifier gain is set such that 1 spectrum channel corresponds to 0.5 keV.

### 2.1.3 Detector efficiency determination

The detector efficiency is dependent on the geometry, density and chemical composition of the sample [Kno79] and can be calculated using the formula [Gil95]:

$$\varepsilon = \frac{C}{L_T \times B_r \times A \times V} \quad (2.1)$$

where

$\varepsilon$  = absolute photopeak efficiency,

$C$  = net counts in photopeak, after appropriate background subtraction,

$L_T$  = live time, the time during which the system is available for processing a pulse,

$A$  = activity concentration ( $\text{Bq.kg}^{-1}$  or  $\text{Bq.l}^{-1}$ ) of the sample,

$V$  = volume (1 litre) of sample (or sample mass in the case of solid samples),

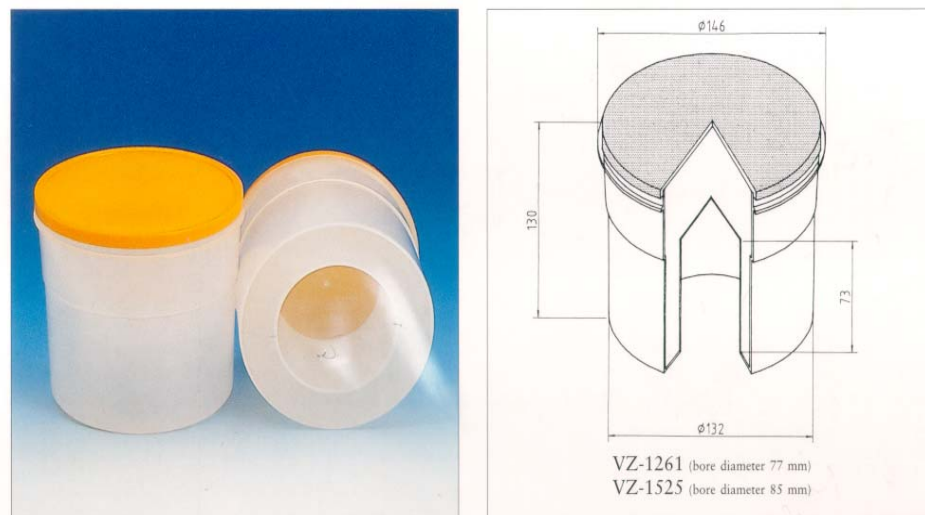
$B_r$  = branching ratio, the statistical chance that a particular  $\gamma$ -ray is emitted per decaying nucleus [Fir96].

The net counts,  $C$ , for a particular photopeak from the spectrum is determined by manually setting a region of interest (ROI) around the peak of interest and the Oxford–Win software then uses an algorithm to automatically calculate the gross and net counts (i.e. those above the background in the sample spectrum) associated with the ROI. There was no background correction applied to the net counts in determining the absolute efficiency of the liquid source because it did not contain any naturally occurring radionuclides. However when analysis was done on the soil, sand and KCl samples, a tap water measurement was used for the background correction. The energies of the photopeaks that were investigated, were chosen such that their branching ratios were above 3 %.

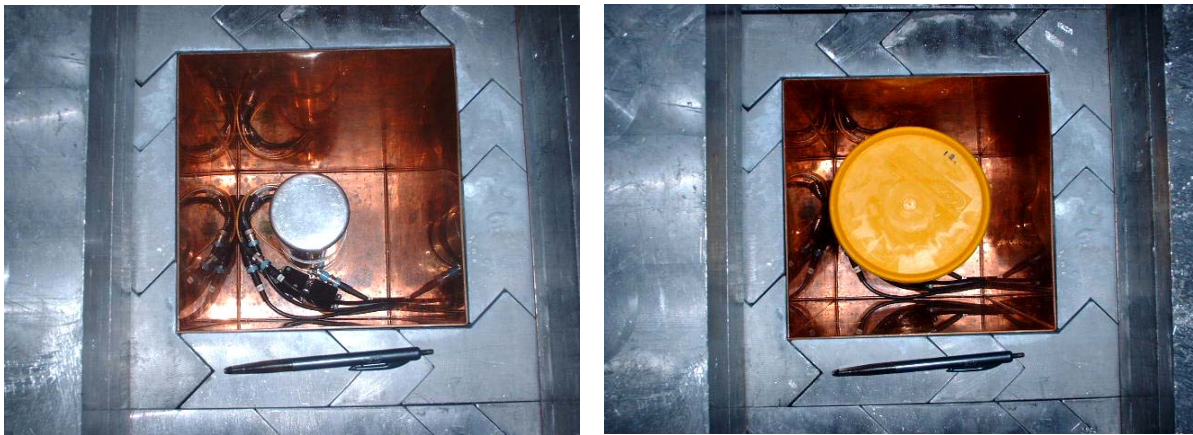
## 2.2 Sample preparation

To optimise the detection efficiency in measuring environmental samples, a large quantity of the sample must be as close to the detector crystal as possible [Deb89]. In order to achieve this we make use of Marinelli beakers. Measurements using the Marinelli beaker are referred to as close geometry radioactivity measurements.

The Marinelli beaker used in this study is a litre polypropylene beaker with an 85 mm annular bottom (Figure 2.7), manufactured by Amersham [Ame00]. The beaker slides over the HpGe detector as shown in Figure 2.8. The first beaker was designed by L.D. Marinelli in the early 1940s and used mainly for biological applications. By using the Marinelli beaker the sample effectively surrounds the detector so that the counting efficiency is greater than would be the case if the sample were in any other type of container [Mar50].



*Figure 2.7: A picture of the Marinelli beaker used in this work showing its dimensions [Ame00].*



*Figure 2.8: Top view of HPGe detector with and without Marinelli beaker.*

### **2.2.1 Soil and sand samples**

The sand sample that was used in this study was obtained from a beach in Somerset West, Cape Town, in September 2004. The sample was collected, transferred into different Marinelli beakers and sealed with a copper disk and silicon (Figure 2.9). The same procedure was followed for the vineyard soil sample, which was obtained in April 2004, from a farm in the Western Cape called Simonsig. When  $\gamma$ -ray spectrometry is used for the measurement of natural radioactivity in environmental soil and sand samples, the samples must be properly sealed for 21 – 30 days to obtain radioactive secular equilibrium between  $^{222}\text{Rn}$  (radioactive noble gas), its decay products ( $^{214}\text{Pb}$  and  $^{214}\text{Bi}$ ) and radium ( $^{226}\text{Ra}$ ), from the  $^{238}\text{U}$  decay series. In the  $^{232}\text{Th}$  decay series the radon isotope ( $^{220}\text{Rn}$ ) poses no serious problem because of its short half-life of 55 seconds and in the  $^{40}\text{K}$  decay series no equilibrium is needed [Cle94]. For a high moisture content sample (> 15 %), the sample is oven dried at 100 °C. All samples are weighed and the date of sealing is recorded (Table 2.2).





*Figure 2.9: Sand sample sealed with copper disk and silicon in Marinelli beaker.*

Sample description	Sample type	mass kg	density g.cm <sup>-3</sup>
Simonsig Sample: Pomphuis Hole 18	soil	1.15764	1.15764
Beach Sand from Strand: 1.0 Litre volume filled	soil	1.62588	1.61607
Beach Sand from Strand: 0.9 Litre volume filled	soil	1.38459	1.61607
Beach Sand from Strand: 0.8 Litre volume filled	soil	1.32297	1.61607
Beach Sand from Strand: 0.7 Litre volume filled	soil	1.13265	1.61607
Beach Sand from Strand: 0.6 Litre volume filled	soil	1.00562	1.61607
Beach Sand from Strand: 0.5 Litre volume filled	soil	0.83009	1.61607
Beach Sand from Strand: 0.4 Litre volume filled	soil	0.67137	1.61607

*Table 2.2: Data recorded of soil and sand samples used in this study.*

## 2.2.2 KCl samples

The relative efficiency curves of the soil and sand samples measured by the ERL are set on an absolute scale by measuring the absolute efficiency at 1461 keV for a potassium chloride (KCl) sample having the same volume as that of the sample under investigation.

To investigate the influence of sample density on the photopeak efficiency, four (4)  $^{40}\text{K}$  calibration standards with matrices of densities ranging from 0.6 – 1.6  $\text{g.cm}^{-3}$  were prepared by spiking inactive organic (stearic powder and starch) and natural (gypsum and quartz sand) materials with  $^{40}\text{K}$ . These materials are all resistant to oxidation and gamma sterilization. The matrices were spiked by adding a known mass of KCl (Table 2.3) and then mixing each mixture in a rotational bath for approximately 10 minutes at  $2 \text{ rev.s}^{-1}$  in order to achieve homogeneity. The samples were then transferred to standard Marinelli beakers and counted on the ERL's HPGe [Jos05].

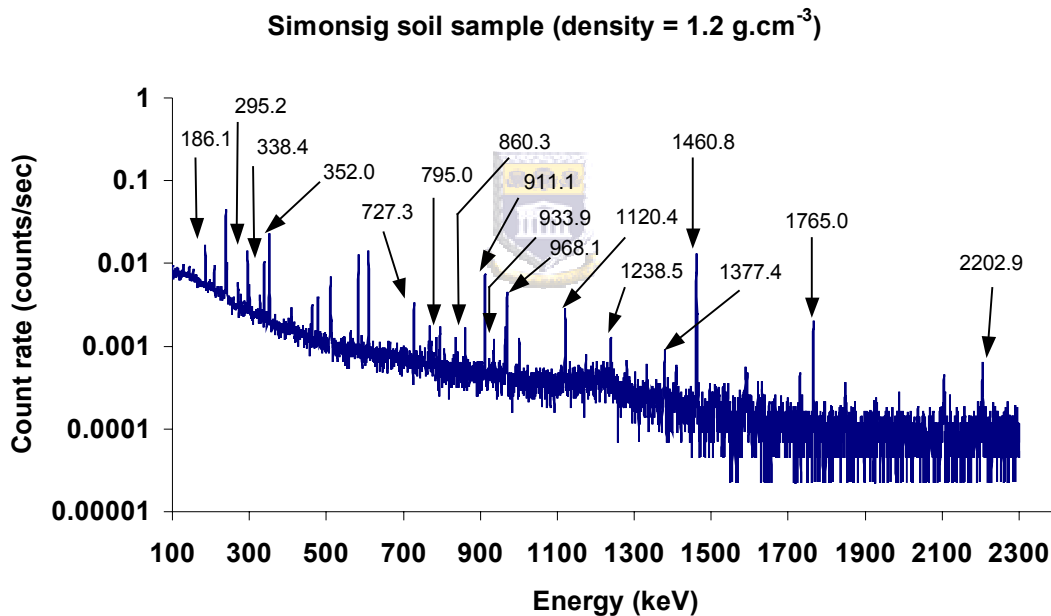
Material	Formula	Standards			
		Stearic+K	Starch+K	Gypsum+K	Quartz+K
		(g)	(g)	(g)	(g)
Stearic acid	$\text{CH}_3(\text{CH}_2)_{16}\text{COOH}$	577.42			
Starch	$(\text{C}_6\text{H}_{10}\text{O}_5)_{20}$		802.85		
Gypsum	$\text{CaSO}_4 \cdot 0.5\text{H}_2\text{O}$			863.67	
Quartz sand	$\text{SiO}_2$				1403.94
Potassium Chloride	KCl	81.00	61.01	75.13	197.01
<b>Total Mass in 1 litre Marinelli beaker</b>		<b>658.42</b>	<b>863.86</b>	<b>938.80</b>	<b>1600.95</b>

Table 2.3: Masses of materials and KCl used in study [Jos05].

### 2.3 Measurements

All samples used in this study were counted on the ERL's HPGe detector system. The ERL has established a sample database for all samples that are counted on their HPGe. The samples that appear in this study can be found on this database according to the information provided in Table 2.4.

Some of the spectra that were obtained with the HPGe are shown in Figures 2.10 – 2.15. All samples presented in this study were prepared as indicated in section 2.2. The spectrum obtained from the soil sample used to investigate if there was evidence for coincidence summing is shown in Figure 2.10.



*Figure 2.10: Spectrum of vineyard soil sample, showing the gamma lines of the naturally occurring radionuclides <sup>238</sup>U, <sup>232</sup>Th and <sup>40</sup>K used to investigate the effect of coincidence summing on photopeak efficiency [Mod05].*

Two examples of the spectra analysed in the study of the effect of volume on the photopeak efficiency are presented in Figures 2.11 and 2.12. These are the spectra for Marinelli beakers that were filled to 400 ml and 1000 ml, respectively.

0.4 litre beach sand sample in Marinelli beaker

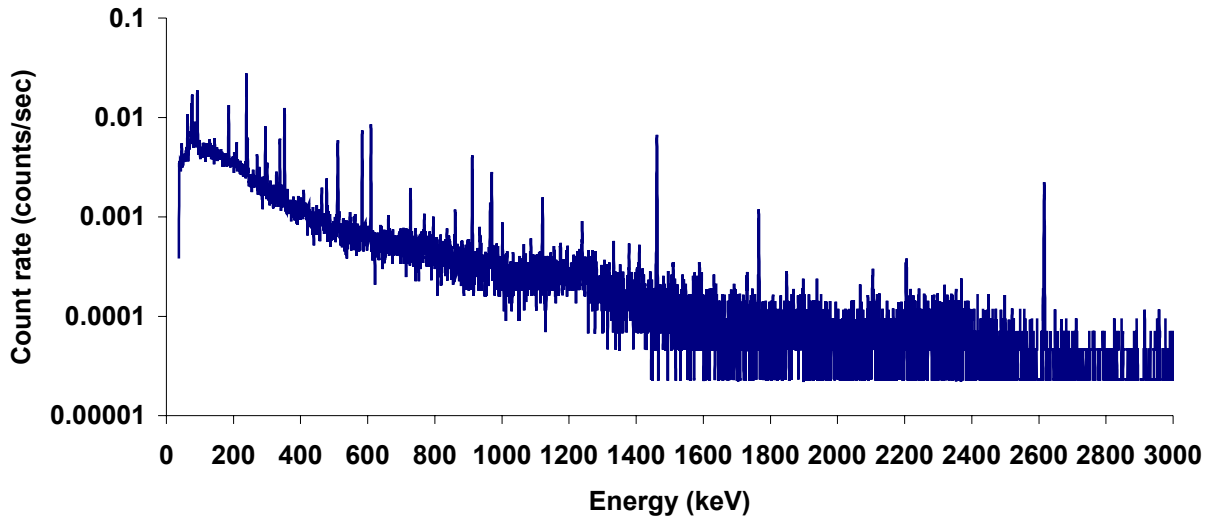


Figure 2.11: Spectrum of 400 ml beach sand sample in Marinelli beaker used to investigate the effect of volume on photopeak efficiency.



1 litre beach sand sample in Marinelli beaker

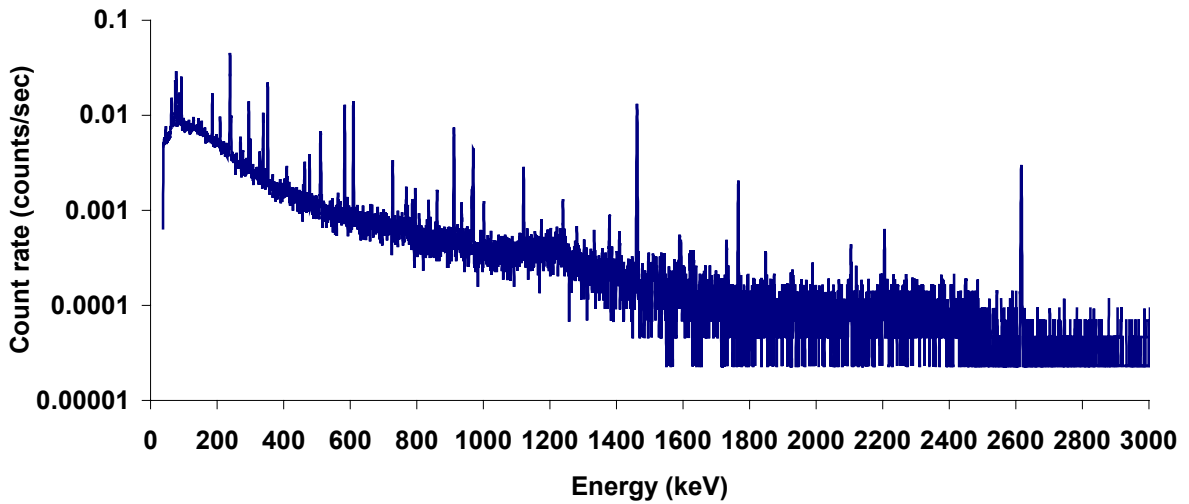


Figure 2.12: Spectrum of 1000 ml beach sand sample in Marinelli beaker used to investigate the effect of volume on photopeak efficiency.

The spectrum of the standard liquid source that was used to investigate coincidence summing is shown in Figure 2.13. This liquid standard contains the radionuclides  $^{152}\text{Eu}$ ,  $^{60}\text{Co}$  and  $^{137}\text{Cs}$ . This standard is used for energy calibrations in the ERL.

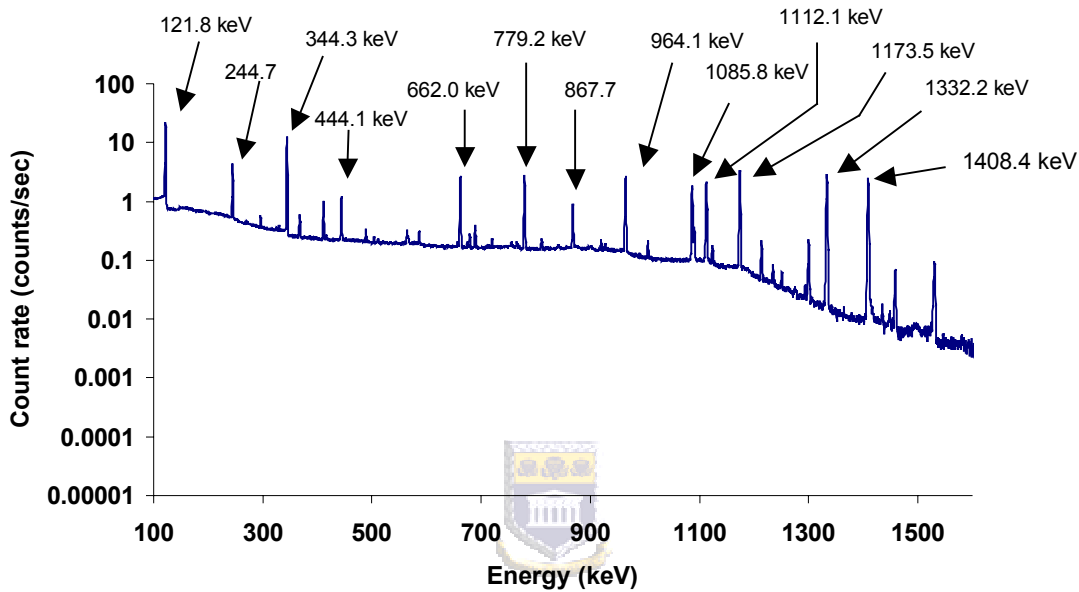


Figure 2.13: Spectrum of Liquid standard source containing the radionuclides  $^{60}\text{Co}$ ,  $^{137}\text{Cs}$  and  $^{152}\text{Eu}$ .

The background spectrum (Figure 2.14) that was used to determine the absolute efficiencies is that of 1 litre tap water sample in a Marinelli beaker. The ERL now uses 1 litre distilled water sample in a Marinelli beaker for background corrections.

1 Litre Tap Water sample

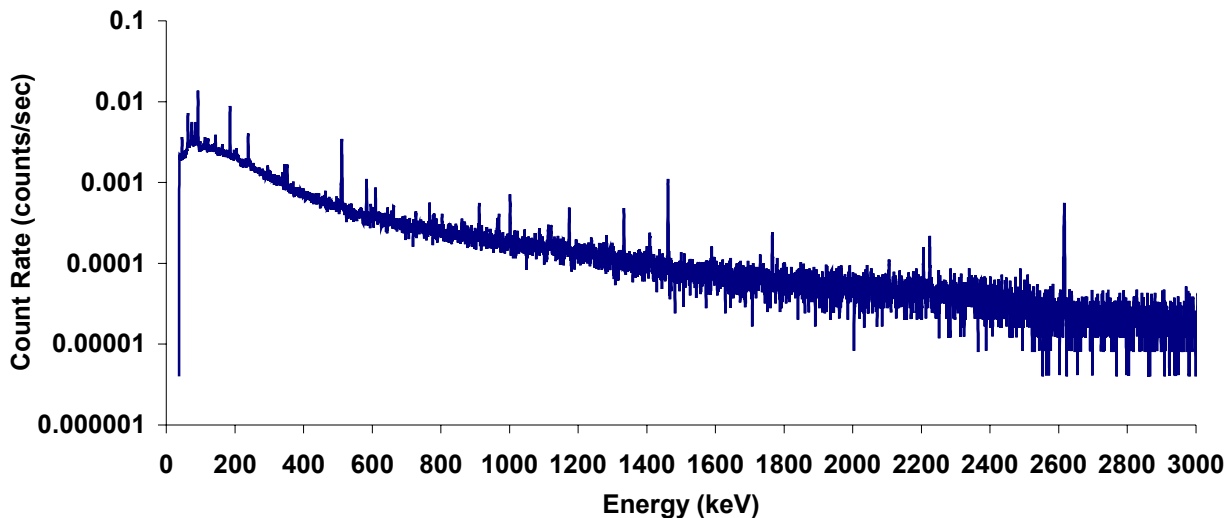
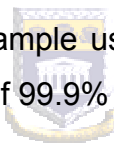


Figure 2.14: Spectrum of 1000 ml tap water sample used for background correction.

Saarchem manufactured the KCl sample used in this study. The spectrum of 1 litre Marinelli beaker filled with KCl of 99.9% purity, is presented in Figure 2.15.



1 liter KCl sample in Marinelli beaker

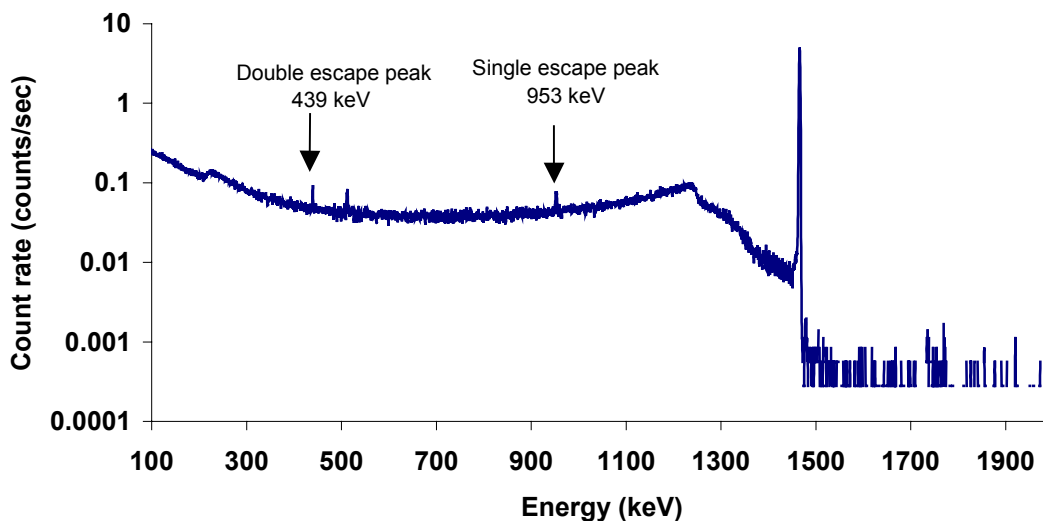


Figure 2.15: Spectrum of 1 litre KCl sample in Marinelli beaker [Jos05].

ERL sample code	ERL spectrum	Sample description	Sample type	Date		Time		Marinelli code
	name			sealed	counted	Live	Real	
Erl-itl-inh-ts-0005	tmts0005	Simonsig Sample: Pomphuis Hole 18	soil	21-Apr-04	28-May-04	35969.64	36000.00	A92
Erl-itl-inh-ts-0012	wdts0001	Beach Sand from Strand: 1.0 Liter volume filled	soil	10-Sep-04	6-Oct-04	43191.68	43200.00	A50
Erl-itl-inh-ts-0013	wdts0002	Beach Sand from Strand: 0.9 Liter volume filled	soil	10-Sep-04	11-Oct-04	43912.07	43200.00	A51
Erl-itl-inh-ts-0014	wdts0003	Beach Sand from Strand: 0.8 Liter volume filled	soil	10-Sep-04	12-Oct-04	43192.20	43200.00	A53
Erl-itl-inh-ts-0015	wdts0004	Beach Sand from Strand: 0.7 Liter volume filled	soil	10-Sep-04	13-Oct-04	43192.54	43200.00	A54
Erl-itl-inh-ts-0016	wdts0005	Beach Sand from Strand: 0.6 Liter volume filled	soil	10-Sep-04	14-Oct-04	43192.84	43200.00	A64
Erl-itl-inh-ts-0017	wdts0006	Beach Sand from Strand: 0.5 Liter volume filled	soil	10-Sep-04	15-Oct-04	43193.40	43200.00	A65
Erl-itl-inh-ts-0018	wdts0007	Beach Sand from Strand: 0.4 Liter volume filled	soil	10-Sep-04	7-Oct-04	43193.91	43200.00	A16
n/a	k400ml	Potassium Chloride Standard: 0.4 Liter volume filled	KCl	-	12-Jun-02	1795.68	1800.00	-
n/a	k500ml	Potassium Chloride Standard: 0.5 Liter volume filled	KCl	-	12-Jun-02	1794.89	1800.00	-
n/a	k600ml	Potassium Chloride Standard: 0.6 Liter volume filled	KCl	-	12-Jun-02	1794.30	1800.00	-
n/a	k700ml	Potassium Chloride Standard: 0.7 Liter volume filled	KCl	-	12-Jun-02	1792.90	1800.00	-
n/a	k800ml	Potassium Chloride Standard: 0.8 Liter volume filled	KCl	-	12-Jun-02	1792.17	1800.00	-
n/a	k900ml	Potassium Chloride Standard: 0.9 Liter volume filled	KCl	-	12-Jun-02	896.91	900.67	-
n/a	k1000ml	Potassium Chloride Standard: 1.0 Liter volume filled	KCl	-	12-Jun-02	895.50	900.00	-
n/a	KCl	Potassium Chloride Standard: 1.0 Liter volume filled	KCl	-	5-Jun-02	3582.73	3600.00	A55
n/a	KQuartz	Potassium Chloride and Quartz matrices	K+Quartz	-	29-May-02	3596.80	3600.00	A11
n/a	Kgyp	Potassium Chloride and Gypsum matrices	K+Gypsum	-	11-Jul-02	3598.38	3600.00	A14
n/a	Ksta	Potassium Chloride and Starch matrices	K+Starch	-	11-Jul-02	3598.78	3600.00	A20
n/a	Kste	Potassium Chloride and Stearic matrices	K+Stearic	-	11-Jul-02	3598.43	3600.00	A15
n/a	bg230704	Background: 1.0 Liter tap water	liquid	-	23-Jul-04	241177.08	241200.00	A09
n/a	Liquid	Standard Liquid Source: <sup>152</sup> Eu, <sup>60</sup> Co and <sup>137</sup> Cs	liquid	-	10-Aug-04	11089.96	11385.09	A32

Table 2.4: Sample reference data from ERL sample database for samples used in this study.

## Chapter 3

### Simulations

Laboratory experiments cannot always test the influence of individual parameters on the detector's response. It is therefore becoming essential to investigate such influences by means of computational techniques. Currently the most widely used method is random sampling (i.e. "Monte Carlo" simulations). However, it is important to understand that MC methods do not solve an equation, but only approximates an average behaviour [Hen03, Man01].

In radiation-transport (R-T) problems this approximation is achieved by simulating "particle" trajectories (photons) from creation to termination (absorption or escape). In MCNPX simulations, the physical quantities for each particle, such as particle flux over a surface or volume, or the energy deposition in a certain part of the geometry ("cell"), are calculated [Man01]. The statistical sampling in R-T problems involves time consuming calculations and therefore advances in computer technology greatly influence the use of MC methods.

### 3.1 MCNPX

#### 3.1.1 History of MCNPX

The Monte Carlo N – Particle (MCNP) transport code is a general-purpose, three-dimensional general geometry; time-dependent, continuous energy MC code that was first released in 1977 and since then 12 upgraded versions have been released. The MCNP code is used to calculate neutron, photon, electron, or coupled neutron/photon/electron transport. MCNP provides a nearly predictive capability of how radiation interacts with matter. Furthermore neutrons are



modelled from 0 to 20 MeV; photons and electrons are modelled from 1 keV to 100 GeV. Since 1965, over 1000 person years have been invested in MCNP and related development of Monte Carlo methods [Man01]. The Applied Theoretical and Computational Physics Division at Los Alamos National Laboratory (USA), where further development of the code continues, developed MCNP and MCNPX.

MCNPX is a major extension of the MCNP code. The MCNPX development program began in 1994, when several groups in the Los Alamos X, T and LANSCE divisions proposed a program of simulation and data tool development in support of the Accelerator Production of Tritium Project. The work involved a formal extension of MCNP with support for 31 additional particle types, extension of proton, neutron and photonuclear libraries to 150 MeV, the ability to use physics models to calculate interactions for energies beyond tabular data and where data tables are unavailable and with new source, tallying and variance reduction options [Man01, Hen00].



Since the initial release of MCNPX version 2.1 on October 23, 1997, an extensive beta-test team has been formed to test the code versions before official release. In November 1999, the final corrected version was released to the **R**adiation **S**afety **I**nformation **C**omputational **C**entre (RSICC). Approximately 800 users in 175 institutions worldwide tested the improvements to the original code and relayed feedback to the developers, which led to version 2.3.0 in April 2002 [Man01]. Since then four (4) beta-test versions have been released. At present the latest version of the code available from RSICC is MCNPX version 2.5.e (March 2004). The beta-test team is constantly working on improving the code with the feedback they obtain from users of the code around the world. The platforms supported by MCNPX are Unix, Linux, Windows and Apple.

### 3.1.2 MCNPX's method of solving R-T problems

The Boltzmann transport equations of R-T through matter can only be solved analytically for some specific configurations. However since the interaction processes for photons are well known and accurate cross-section data are available, radiation transport is ideal for simulation using Monte Carlo methods. In MCNPX simulations, each particle (photon) is tracked from creation until termination with all interactions based on physics models and cross-sections, and all decisions (location of interaction, scattering angle, etc.) are based on pseudo-random numbers [Hen03].

The following discussion is illustrated in Figure 3.1. A photon is created randomly with some initial energy  $E_\gamma$ , starting location and direction. Based on the cross-section data available or physics model where data is not available, for the material through which the photon is transported, an interaction site and type are determined by using a pseudo-random number to sample a pdf. The results of the interaction i.e. remaining energy  $E'_\gamma$  and new direction of the photon is determined by the pdf. This process is repeated until the source photon and its secondary particles have deposited all their energy or escaped the "cell" of interest. Secondary photons that are created in an interaction are temporarily stored in computer memory and their transport is only calculated after the primary photon is completely tracked. A source photon and its descendants are referred to as a "history". When a history is fully tracked and its contribution to the detector's response is determined, a count is recorded in a bin according to its energy. Usually, the results of a simulation are normalised per starting source photon. New source photons are randomly created until a preset number of histories are tracked and the simulation is ended.

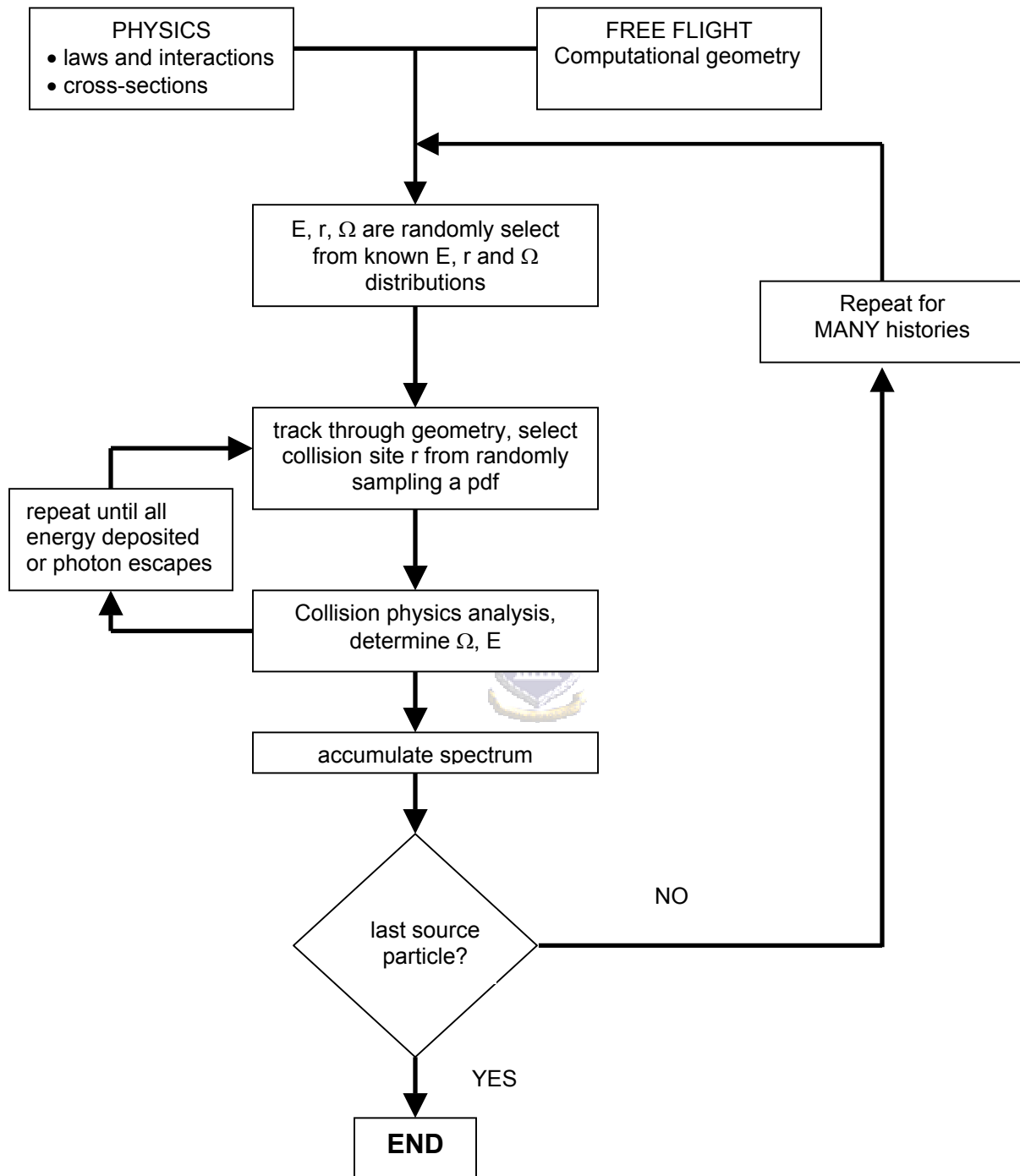


Figure 3.1: Schematic representation of radiation transport in Monte Carlo simulations. All processes are based on physical laws and all decisions are based on random numbers and cross-section tables [Hen03].

### 3.1.3 Physics models used in MCNPX for this study

MCNPX has two photon interaction models: (a) simple and (b) detailed which use the cross-section data of J.H. Hubbell for elements from  $Z = 1$  through  $Z = 94$  in the energy range 1 keV to 100 MeV [Man01, Hen03]:

- (a) The simple physics model ignores coherent (Thomson) scattering (i.e. no energy is lost to the free electron and momentum is conserved) and fluorescent photons created from photoelectric absorption. This model is used for high-energy photon problems or in problems that deal with free electrons and point detectors where scattering can be nearly parallel with coherent scattering.
- (b) The detailed physics model includes coherent scattering and accounts for fluorescent photons. Form factors are used to account for electron binding effects. The electron transport in this study was turned off and therefore any electrons generated in the simulations are dealt with by means of a thick-target bremsstrahlung approximation (TTB). The approximation assumes that any electrons or positrons produced travel in the direction of the incident photon and are immediately annihilated.

The detailed physics model is the best model for most applications, particularly low photon energy problems. The processes considered in this model are discussed in more detail below [Man01]:

- (i) Compton Scattering: is modelled such that the scattering angle and energy  $E'_\gamma$  of the photon is determined from the differential cross-section for a modified Klein-Nishina cross-section where the appropriate scattering factor decreases the cross-section (per electron)

more extremely in the forward direction, for low  $E$  and high  $Z$  independently. The recoil kinetic energy is treated with the TTB approximation.

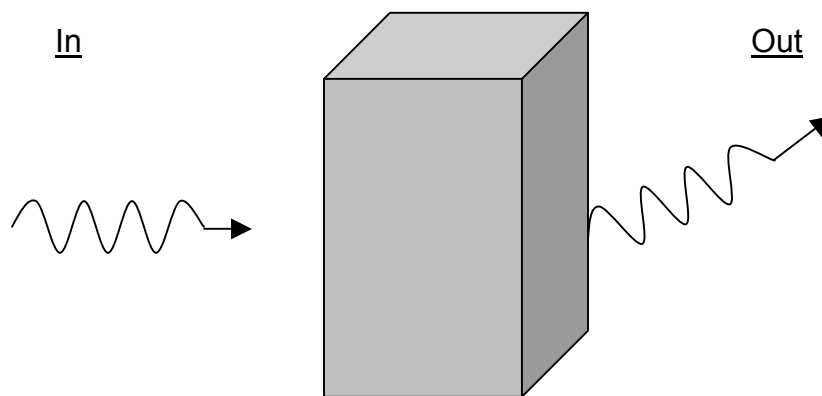
- (ii) Thomson Scattering: does not involve any energy loss and therefore no electrons are produced. The differential cross-section for a modified energy-dependent Thomson cross-section is determined such that the form factor decreases the Thomson cross-section more extremely for back scattering.
- (iii) Photoelectric Effect: the incident photon is absorbed, several fluorescent photons are emitted and an orbital electron of binding energy  $e < E_\gamma$  is ejected (or excited), giving the electron kinetic energy  $E_\gamma - e$ . The fluorescent photons are captured and eject electrons. All electrons produced are treated with the TTB approximation.
- (iv) Pair Production: is considered in the field of the nucleus with a threshold of 1.022 MeV. The electron and positron are created and treated with the TTB approximation. If the positron is below the electron energy cut-off, then a photon pair (0.511 keV each) is created instead and its energy deposited locally.

### 3.1.4 Pulse Height Estimator

The desired result in the simulation component of this study is a pulse height spectrum since it produces the distribution of the energy deposited in a “cell”, i.e. the  $\gamma$ -ray energy spectrum in a physical model of a detector. Pulse height spectra simulations are implemented in MCNPX in the so-called “f8 tally”. This estimator is based on the following fundamental approaches [Hen03]:

- The energy bins in  $\gamma$ -spectra simulations correspond to the energy deposited in the detector cell summed over all the tracks of a history.
- No integral is evaluated, but the deposited energy in a cell is calculated based on the detailed microscopic radiation tracking.
- If the photon does not undergo interactions in a specified cell, no energy is deposited and the photon does not contribute to the pulse height spectrum.

The energy deposition ( $E_{\text{dep}}$ ) calculated by tally “f8” in a “cell” is presented in Figure 3.2. When a photon (or its descendant) enters the cell, the cell is credited with energy ( $E_{\text{in}}$ ) times weight ( $\omega$ ) of the incoming photon. If the photon (or its descendant) leaves the cell, the product of weight ( $\omega$ ) and energy ( $E_{\text{out}}$ ) of the outgoing photon is subtracted from the cell’s energy. Therefore, for each history the total energy is the weighted difference between the incoming and outgoing energies summed over all tracks belonging to that particular history. The count recorded corresponds to the initial weight  $\omega_s$  of the source photon. Hence for each history, only one count is added to the spectrum [Man01, Hen03].



$$\frac{E_{\text{dep}}}{\omega_s} = \sum \omega_{\text{in}} E_{\text{in}} - \sum \omega_{\text{out}} E_{\text{out}}$$

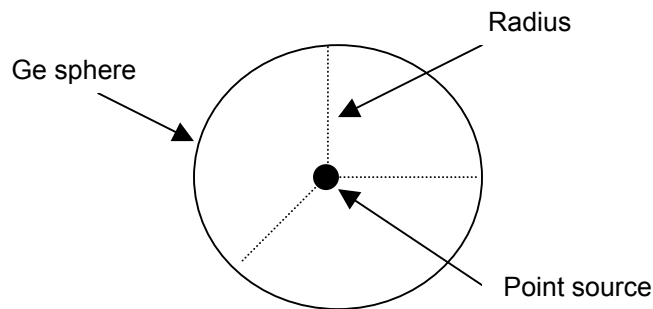
Figure 3.2: The energy deposition ( $E_{\text{dep}}$ ) in a cell calculated by tally f8 [Hen03].

## 3.2 Intercomparison exercise

An intercomparison was made of the results from the MCNPX code and a Dev – C++ program, developed for this study, to obtain a better understanding of the use of MC methods in R-T problems and the physical concepts involved in such calculations.

### 3.2.1 Geometry and physical properties

For this exercise, a spherical geometry was chosen because of its symmetry, thereby making it easier to simulate (Figure 3.3). The user determines the energy of the point source of gamma-rays (located at the centre of the sphere) and the radius of the germanium ( $\rho = 5.323 \text{ g.cm}^{-3}$ ) sphere for each simulation. The  $\gamma$ -ray energies simulated were those associated with the radionuclides of  $^{137}\text{Cs}$  (in a sphere with radii 1 cm and 5 cm sphere, respectively) and  $^{152}\text{Eu}$  (in a sphere with radius 5 cm) to obtain an absolute efficiency curve (Figure 3.12), for comparison with MCNPX.



*Figure 3.3: Schematic of geometry used in intercomparison exercise.*

### 3.2.2 MCNPX approach

All simulations in this study were done with MCNPX version 2.5.c, which was released in April 2003 by RSICC. MCNPX was used for this study because the code is being used by other departments at iThemba LABS and therefore the necessary expertise was available with regards to the use of the code. The code is run on a Windows operating system (Table 3.1) and each simulation takes approximately 20 minutes for volume sources and 10 minutes for point sources. Each simulation is run with 10 million source particles, assumed to be distributed homogeneously throughout the source volume or at the centre of the sphere geometry. In the case of the spherical geometry the MCNPX simulations are normalised to 100000 source particles (Figures 3.5 and 3.14). The input files for both geometries are listed in Appendix A and B, respectively.

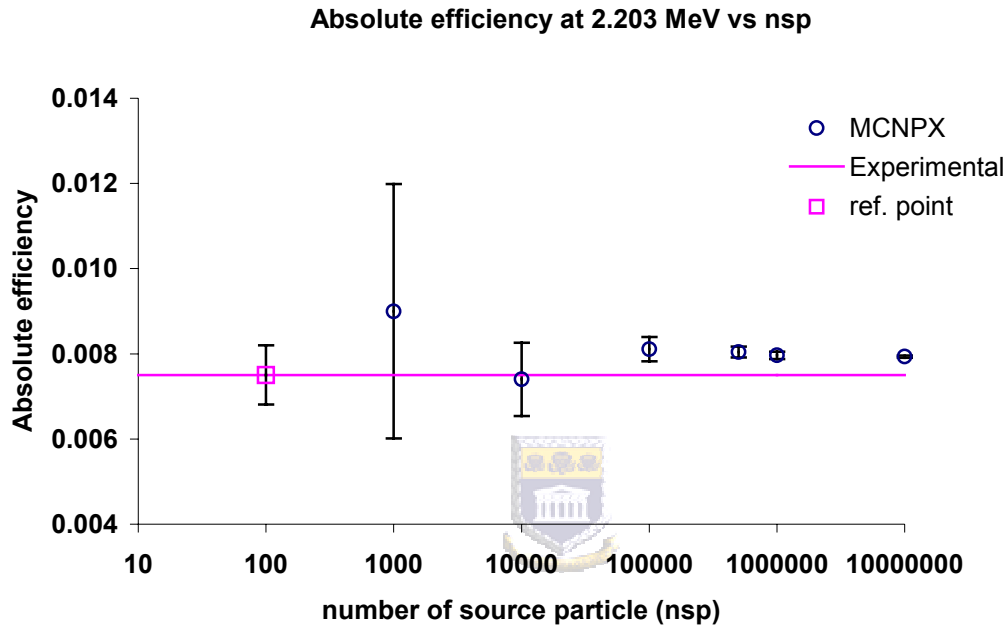
System	Microsoft Windows 2000
Processor	Intel Celeron I CPU – 1000 MHz
RAM	128KB
Hard drive	10 GB

*Table 3.1: Specifications of Computer and Operating System used for this study.*

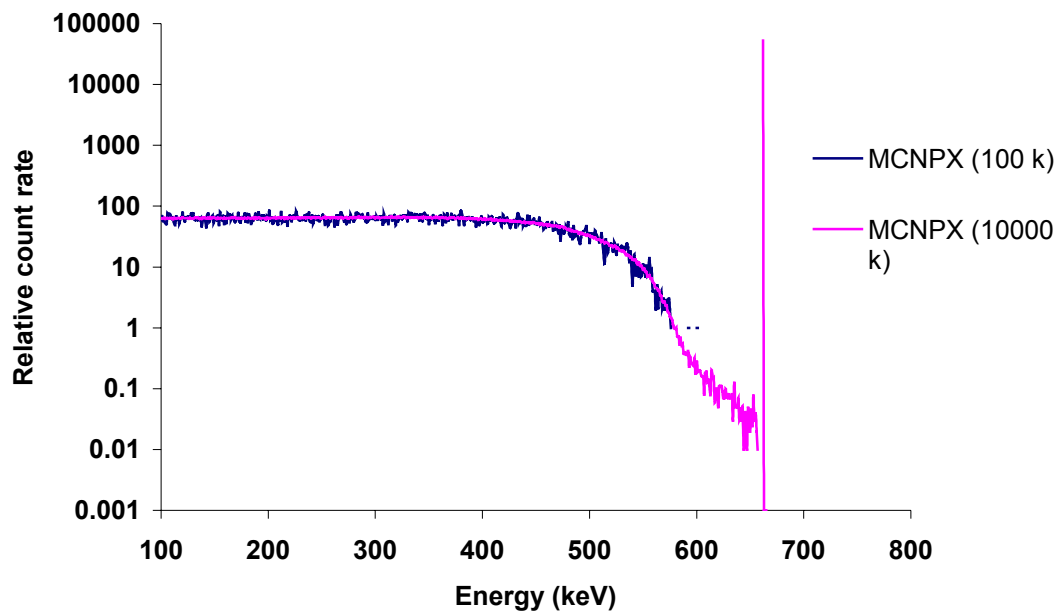
This number of source particles (nsp) was chosen because it was found, as shown in Figure 3.4, that the absolute efficiency value approaches a steady value and the relative variance decreases as the nsp increases. It is also evident from Figure 3.5 that there are less statistical fluctuations in the spectrum simulated with 10 million histories compared to the spectrum simulated with 100000 histories. The uncertainty in the efficiency values in MCNPX is given as a percentage of the efficiency for a specific energy in the output of the simulation. The energy simulated here is that of the radionuclide  $^{214}\text{Bi}$ , from the decay series of  $^{238}\text{U}$ , in a generic soil sample of density  $1.2 \text{ g.cm}^{-3}$  (section 3.3.2) in a litre Marinelli beaker (Table 3.7). The source particles are assumed to be distributed



homogenously throughout the source volume. The experimental value used as a reference, was obtained from a beach sand sample counted with the ERL HPGe detector in a standard Marinelli beaker in September 2004 (section 2.2.1).



*Figure 3.4: Improvement of absolute efficiency with nsp. The experimental reference point and line used is that of a 1 litre beach sand sample in a Marinelli beaker counted with the ERL HPGe detector.*



*Figure 3.5: Spectra of 662 keV point source in the centre of 5 cm germanium sphere, showing the statistical fluctuation for MCNPX when 10 million and 100000 histories are simulated .*



Figure 3.6 shows the Compton edges in the MCNPX simulations for a 662 keV point source in a 1 cm and 5 cm sphere. The spectra were normalised to 100000 source particles.

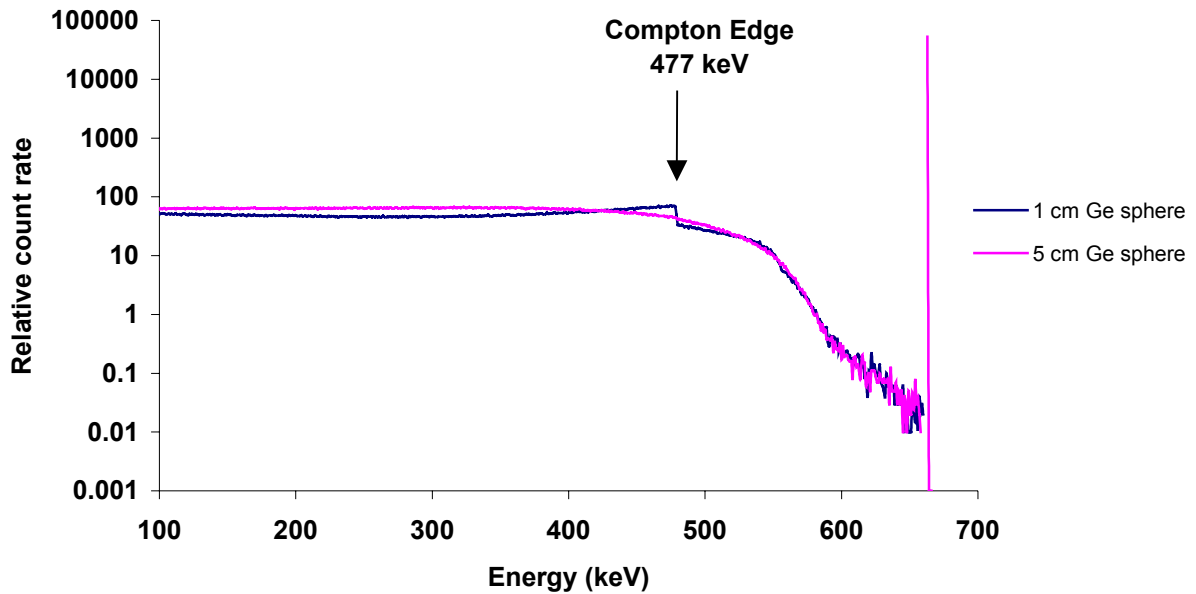


Figure 3.6: MCNPX simulated spectra for a 662 keV point source in germanium spheres of different radii. The photopeak for the 1 cm sphere, at 4564 counts is below the photopeak for the 5 cm sphere.



### 3.2.3 C++ approach

The C++ program was written to determine the distribution of energy that would be deposited in a germanium sphere ( $\rho = 5.323 \text{ g.cm}^{-3}$ ), if a point source of gamma-rays (10 keV – 1.0 MeV) were placed at the centre of the sphere. The source code for this program is listed in Appendix C.

#### 3.2.3.1 Assumptions and Simplifications

The assumptions made for simplicity are as follows:

- Either Compton Scattering (CS) or photoelectric absorption (PE) occurs (energy range of gamma-rays: 10 keV – 1.0 MeV).
- All scattering is isotropic i.e. no anisotropic angular distribution of scattering is considered ( i.e. the Klein-Nishina formula was not used).

### 3.2.3.2 The Conceptual Model

The flowchart showing how the program is structured to obtain a spectrum of the energy deposited in the sphere is shown in Figure 3.7. The user first enters the energy of the source gamma-ray (10 keV – 1.0 MeV), the radius of the sphere and the number of gamma-rays to be simulated. The path length (i.e. the length ( $d$ ) that a photon will travel before depositing 99.99 % of its energy) of the photon is determined dependent on its energy and thereafter an interaction point is chosen along this length (section 3.2.3.4). If this interaction point (Figure 3.8) is within the sphere an interaction will occur depositing energy in the sphere, depending on the type of interaction that occurs. If the photon is fully absorbed (PE), then all of its energy is deposited, the photon is terminated and the program continues onto the next photon until all source photons are simulated. On the other hand if CS occurs the photon deposits some of its energy (equation 1.3) and is then scattered in some random direction, depositing energy until it is fully absorbed in the sphere or escapes.



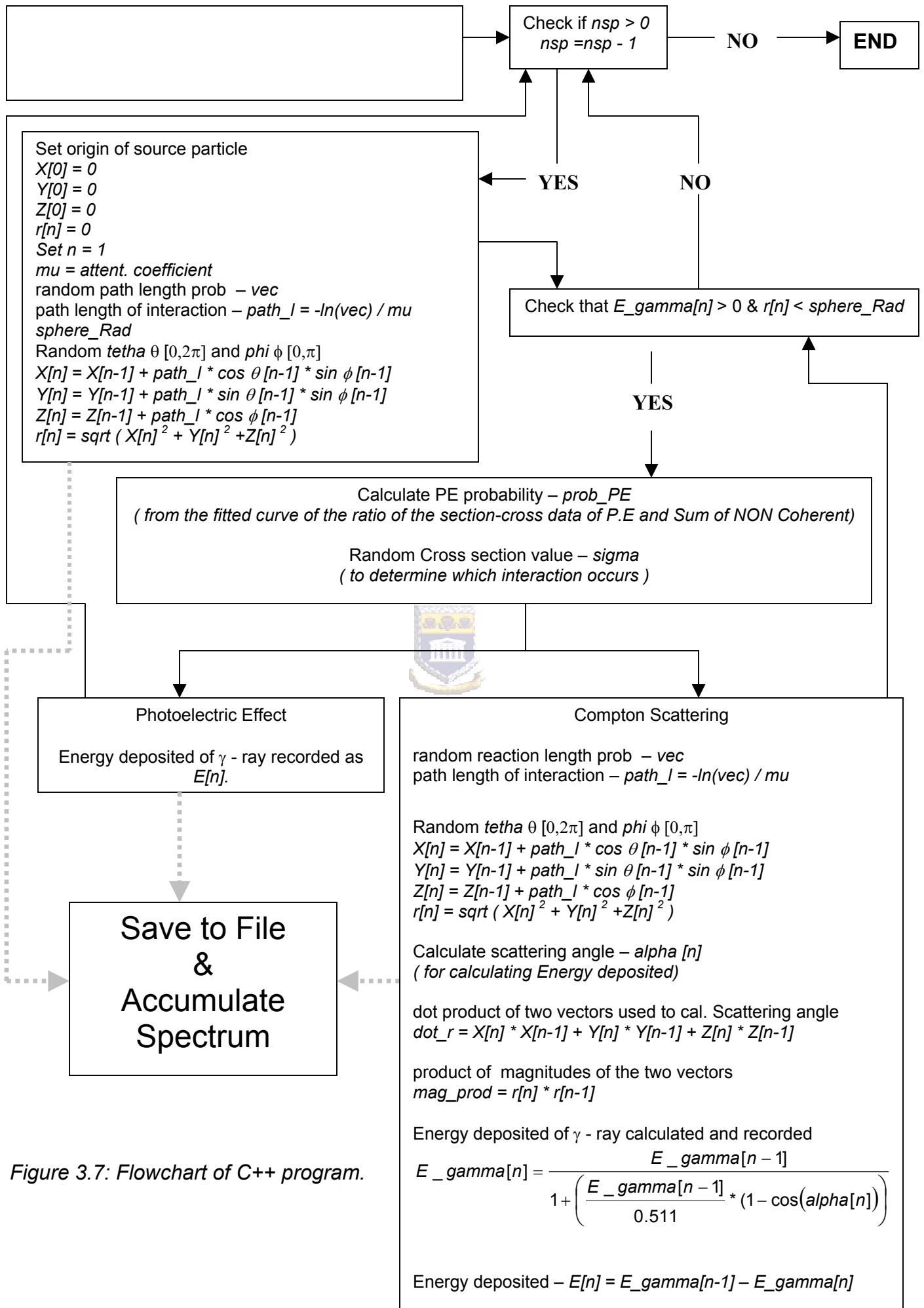
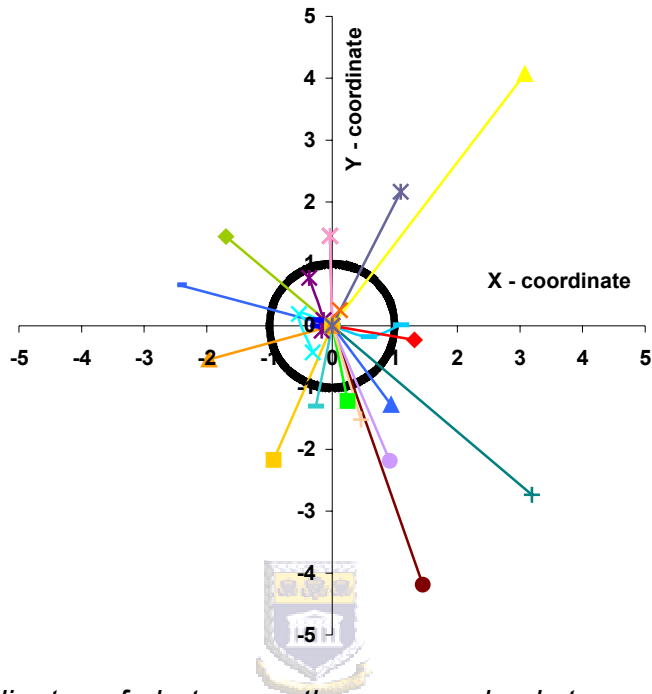


Figure 3.7: Flowchart of C++ program.

Figure 3.8 shows the random coordinates of 20 particles as they are transported through the germanium sphere. The black circle indicates the 1 cm radius of the germanium sphere.



*Figure 3.8: Coordinates of photons as they are randomly transported through a germanium sphere with a radius of 1 cm. The black circle illustrates the radius of the sphere.*

The energy that is deposited in the sphere is recorded and binned in order to obtain an energy deposition spectrum (Figure 3.9).

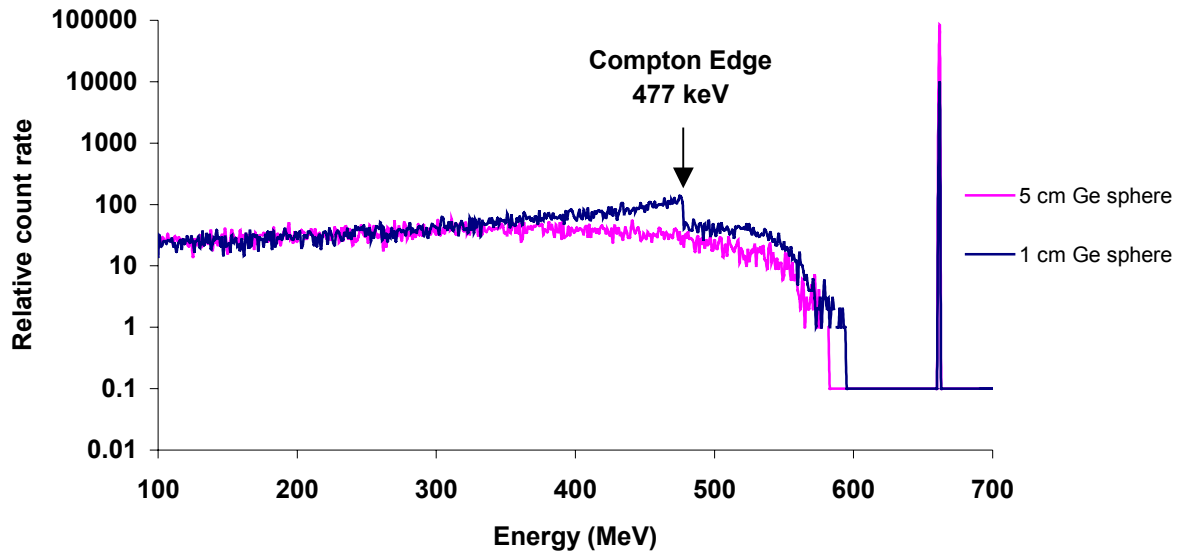


Figure 3.9: Simulated C++ spectra for a 662 keV point source in germanium spheres of different radii.



### 3.2.3.3 Important Physics Processes considered in simulation

During each simulation, the program outputs the coordinates of each interaction point, the scattering angles and the energy that each source photon deposits, which are binned to create a spectrum.

### 3.2.3.4 Path length

The path length (i.e. the length ( $d$ ) that a photon will travel before an interaction occurs) of the photon in germanium ( $\rho = 5.323 \text{ g/cm}^3$ ), is determined from the probability  $p(d)$  of a photon interacting in the germanium [Bea78]. The probability that a photon will interact is chosen randomly i.e.  $p(d) = \xi \in (0,1)$ , which must correspond to the usual absorption equation,

$$p(d) = 1 - e^{-\mu_1 d}$$

$$d = -\frac{\ln(1 - p(d))}{\mu_1}$$

$$d = -\frac{\ln(1 - \xi)}{\mu_1}$$

Since  $1 - \xi$  is distributed in the same way as  $\xi$  and hence may be replaced by  $\xi$ , we obtain

$$d = -\frac{\ln(\xi)}{\mu_1} \quad (3.1)$$

The mass attenuation coefficients were obtained from the NIST XCOM: photon cross-section database [Hub82]. These values were then used to obtain the linear attenuation coefficients ( $\mu_1$ ). These were then plotted as a function of energy and a polynomial curve was fitted (Figure 3.10) to the data, using the software program TableCurve 2D v5.01. This was done in order to extrapolate the linear attenuation coefficient (equation 3.2) required by equation 3.1, to calculate the path length ( $d$ ) of the photon as a function of energy.



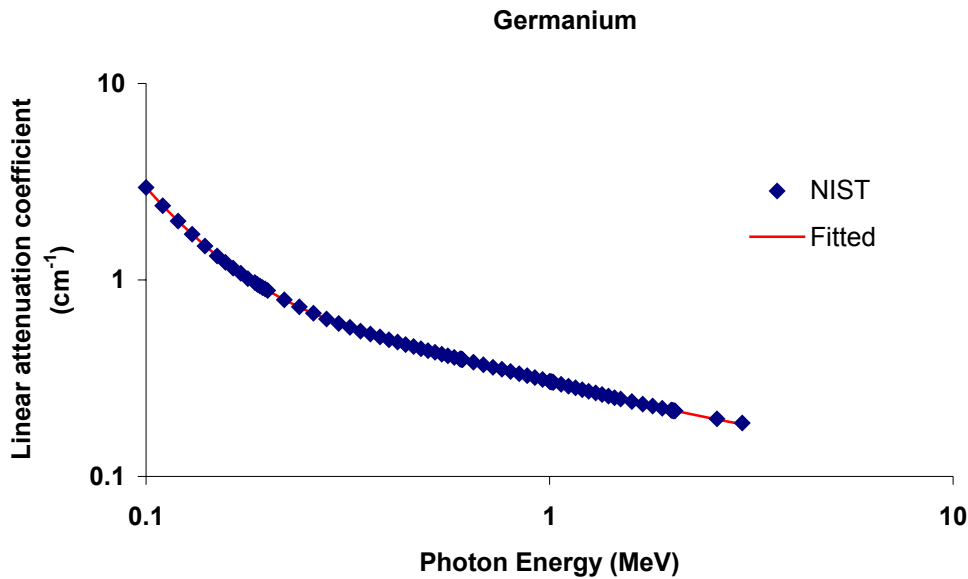


Figure 3.10: Curve fitted to the linear attenuation coefficients obtained from the NIST mass attenuation coefficients for germanium, as function of photon energy

The polynomial equation,

$$\mu_l = \frac{(a + cx + ex^2 + gx^3)}{(1 + bx + dx^2 + fx^3)} \quad (3.2)$$

where  $x$  is the  $\gamma$ -ray energy, was used for the curve fitting. The best fit parameter values  $a$ ,  $b$ ,  $c$ ,  $d$ ,  $e$ ,  $f$  and  $g$  are given in Table 3.2.

Param	Value
a	-12.8023
b	-11.1733
c	54.76261
d	-227.001
e	-430.608
f	-1603.66
g	-171.599

Table 3.2: Optimal parameters used in equation 3.2 to fit the linear attenuation coefficients.

TableCurve2D uses four common goodness of fit statistics, namely Coefficient of Determination ( $r^2$ ), Degree of Freedom Adjusted Coefficient of Determination, Fit Standard Error and F-statistic. Equations 3.2 and 3.3 were chosen because the  $r^2$  value for each of the fits was 0.9999. As the fit improves, the  $r^2$  values approach 1.0 (0 represents a complete lack of fit). The Coefficient of Determination ( $r^2$ ) is calculated as follows,

$$r^2 = 1 - \frac{SSE}{SSM}$$

where SSM is the sum of the squares about the mean and SSE is the sum of the squared errors (residuals).

### 3.2.3.5 Probability of Scattering

The probability of scattering (Figure 3.12) is extrapolated from the ratio of the total cross-section with non-coherent scattering (SNC), and the cross-section for photoelectric absorption. The photoelectric absorption cross-section (Figure 3.11) data for germanium are taken from the data of Nuclear Data Tables A7 [Sto70]. A random number in the interval [0,1] is generated, if the number is less than or equal to the value obtained from equation 3.3 then PE occurs otherwise the photon undergoes CS. This is a simple weighting of the two processes according to their relative cross-sections.

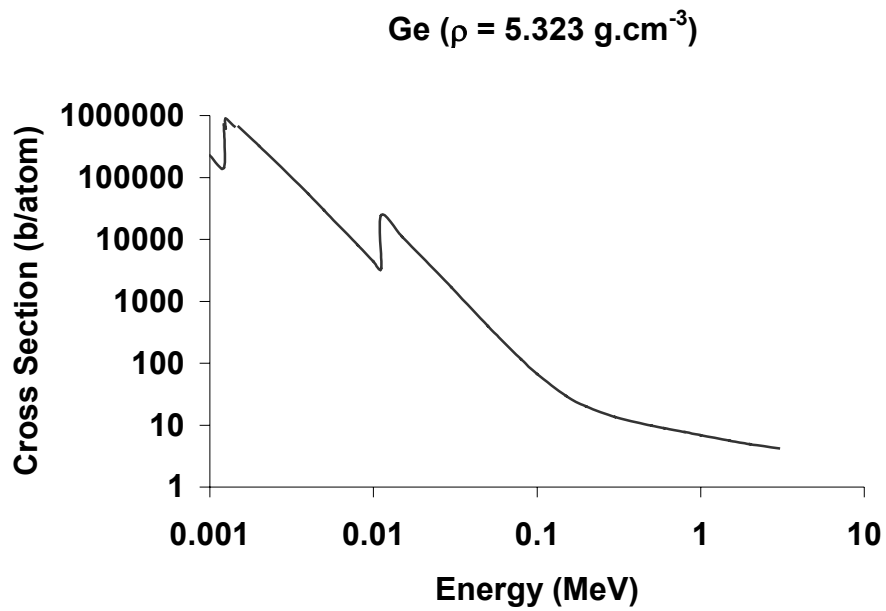


Figure 3.11: Plot of the PE cross-section for Ge in the energy range of interest.

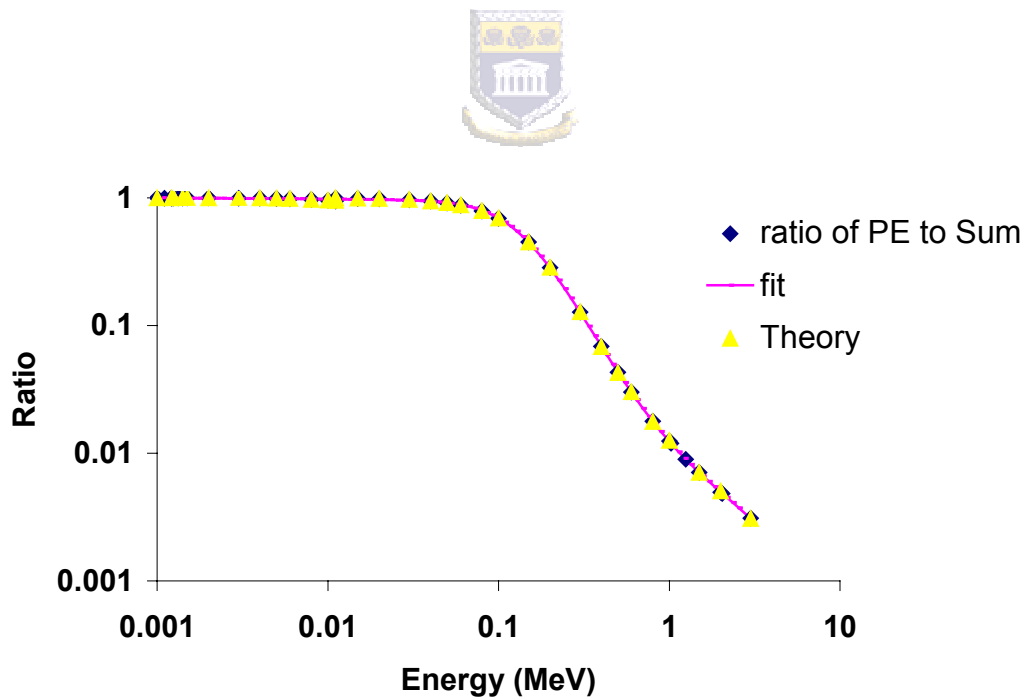


Figure 3.12: Ratio of the cross-section values of PE to the total (sum) to determine the scattering probability.

The polynomial equation that determines the ratio of the cross-sections is

$$\text{ratio} = \frac{(h + jx^{0.5}) + lx + nx^{1.5}}{(1 + ix^{0.5}) + kx + mx^{1.5} + ox^2} \quad (3.3)$$

where best fit parameters h, i, j, k, l, m, n and o are given in Table 3.3 and x is the energy of the photon.

Param	Value
h	1.018913
i	-1.20045
j	-1.91432
k	-2.20945
l	1.656692
m	1.839459
n	-0.31875
o	36.39973

*Table 3.3 Parameters used to determine scattering probability.*



### 3.2.4 Intercomparison results and discussion

The aim of writing a MC program was to establish a better understanding of the physical concepts involved in such calculations.

The spectra of the energy deposition of a 662 keV ( $^{137}\text{Cs}$ ) point source in germanium spheres of radii 1 cm and 5 cm, were simulated by both codes as shown in Figures 3.6, 3.9 and 3.15. With the use of equation 1.3 it can be shown that the maximum energy that can be deposited due to Compton Scattering for a 662 keV  $\gamma$ -ray (i.e. Compton edge) is 477 keV. The Compton edge in both figures shows good agreement with this value.

A  $^{152}\text{Eu}$  point source was simulated in a 5 cm germanium sphere to obtain the absolute detection efficiency curve of Figure 3.13. The comparison between C++ and MCNPX for the same geometry shows a deviation of up to 30 % (Figure 3.14 and Table 3.4).

Energy keV	Efficiency		Difference	Peak to Total	
	C++	MCNPX		MCNPX	C++
121.9	0.9998	0.9997	0.02%	1.000	1.000
244.9	0.9373	0.8948	4.5%	0.895	0.937
344.6	0.8497	0.7653	9.9%	0.765	0.910
444.1	0.7772	0.6658	14.3%	0.666	0.858
661.8	0.6766	0.5256	22.3%	0.475	0.799
779.2	0.6371	0.4752	25.4%	0.415	0.774
964.1	0.5908	0.4155	29.7%	0.415	0.748

Table 3.4: Comparison between absolute detection efficiency values from C++ and MCNPX simulations of  $\gamma$ -rays from a  $^{152}\text{Eu}$  and  $^{137}\text{Cs}$  point source located at the centre of a germanium sphere with radius 5 cm.



Absolute efficiency curve

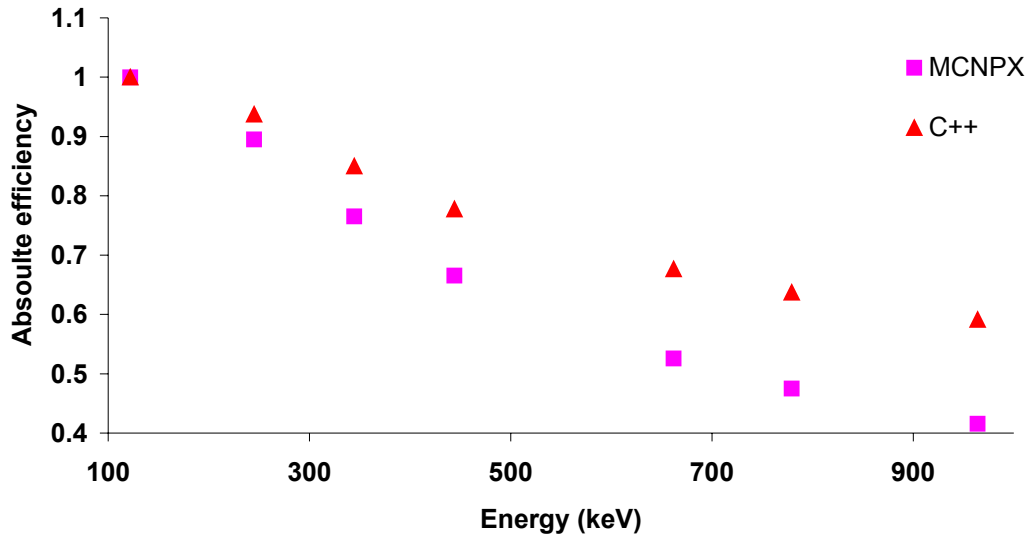
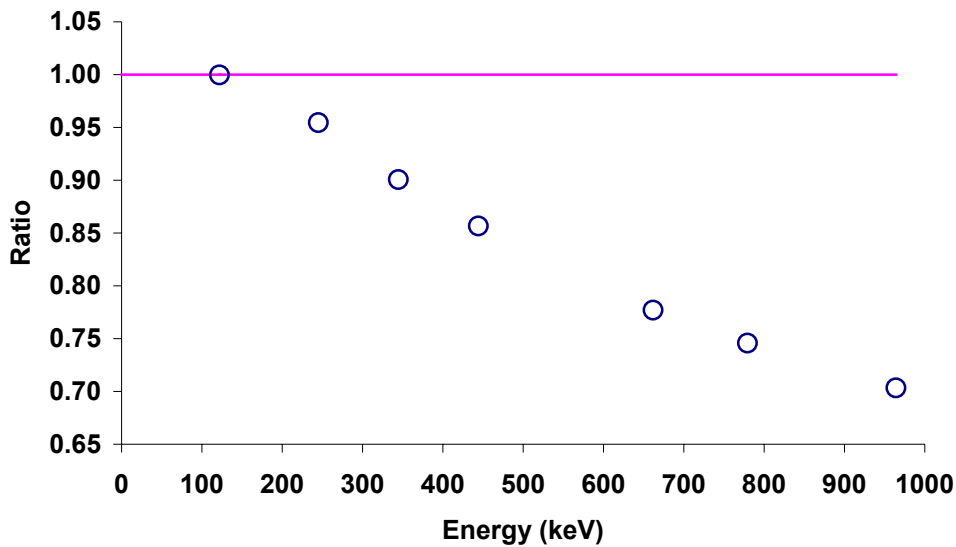


Figure 3.13: Absolute detection efficiency curves for  $\gamma$ -rays from a  $^{152}\text{Eu}$  and  $^{137}\text{Cs}$  point source in a germanium sphere with radius 5 cm.

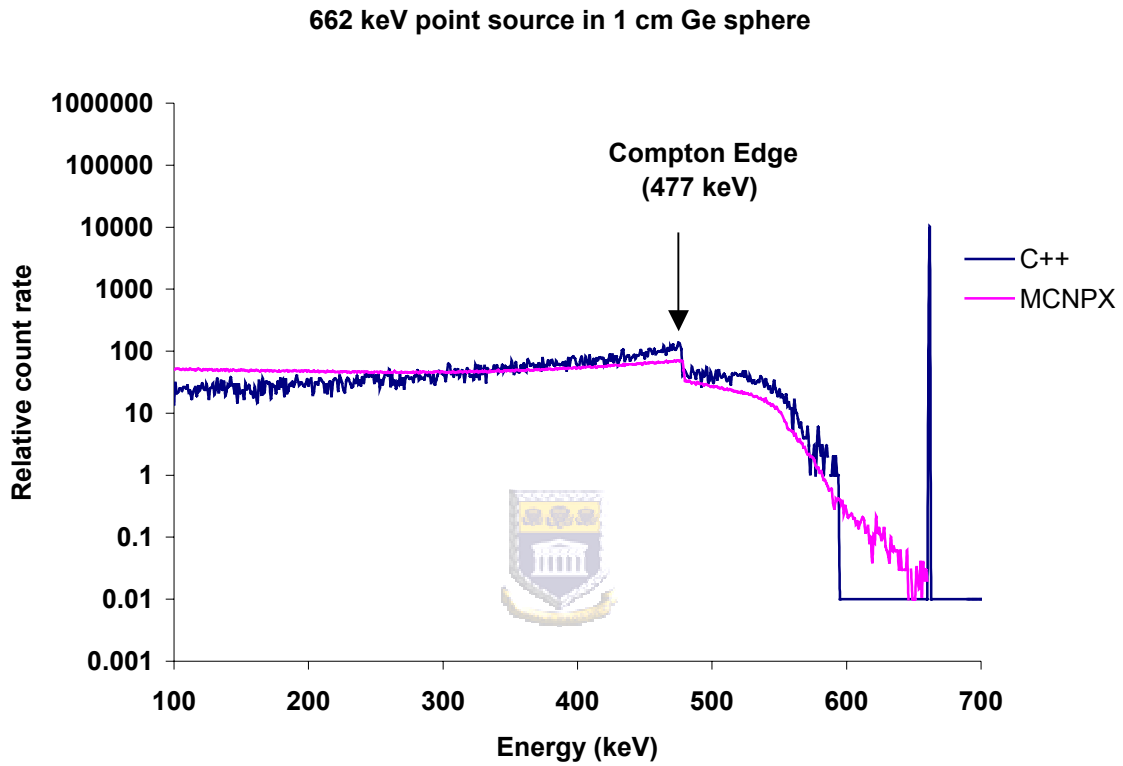


*Figure 3.14: Ratio of absolute detection efficiency values of MCNPX to C++ simulations.*



Figure 3.14 is a plot of the ratio of the absolute detection efficiency values of MCNPX to C++ simulations. The deviations between the results can probably be attributed to the assumptions made in the C++ program (section 3.2.3.1). For energies below 400 keV photoelectric absorption predominates (Figure 1.8) and the strong Z dependence of this interaction would explain the difference of less than 10 % between C++ and MCNPX. However for energies above 400 keV, Compton scattering begins to dominate (Figure 1.8) and therefore the large differences shown in Figure 3.14 are due to the fact that the photons in the C++ program are assumed to all scatter randomly, whereas in MCNPX the Klein-Nishina formula is used which predominately causes forward scattering (section 3.1.3). This forward scattering would cause more photons to likely escape the sphere after undergoing Compton scattering, whereas the random scattering in the C++ simulations is more likely to cause the photon to scatter back into the sphere. This results in a greater probability that the photon will undergo a further interaction and deposit all of its energy in the sphere and therefore contributing to

a higher photopeak efficiency. This difference in the photopeak intensity could therefore account for the three times higher Compton continuum found in the MCNPX simulations, in the low energy region of Figure 3.15.



*Figure 3.15: Spectra showing the larger number of Compton events in MCNPX.*

### 3.3 ERL Marinelli geometry

#### 3.3.1 MCNPX input specifications

The dimensions of the Canberra HPGe detector simulated with MCNPX are given in Table 3.5 [Can99]. The Marinelli beaker is constructed from polypropylene of thickness 0.18 cm, with a density of  $1.65 \text{ g.cm}^{-3}$  and is resistant to acids and most organic solvents [Iso98]. The Marinelli beaker slides over the detector creating a close geometry system, as shown in Figure 2.8. Figure 3.16 is a schematic of the close geometry system used in the simulations, where the Marinelli beaker is assumed not to be tapered in this geometry, as in Figure 2.7, and the lead castle with its copper lining was not included. The components of the detector used in the simulations are made up of “cells”, which are a piece of space/volume that is bound by surfaces (Appendix B). These components and their cell and surface numbers are given in Tables 3.5 and 3.6.

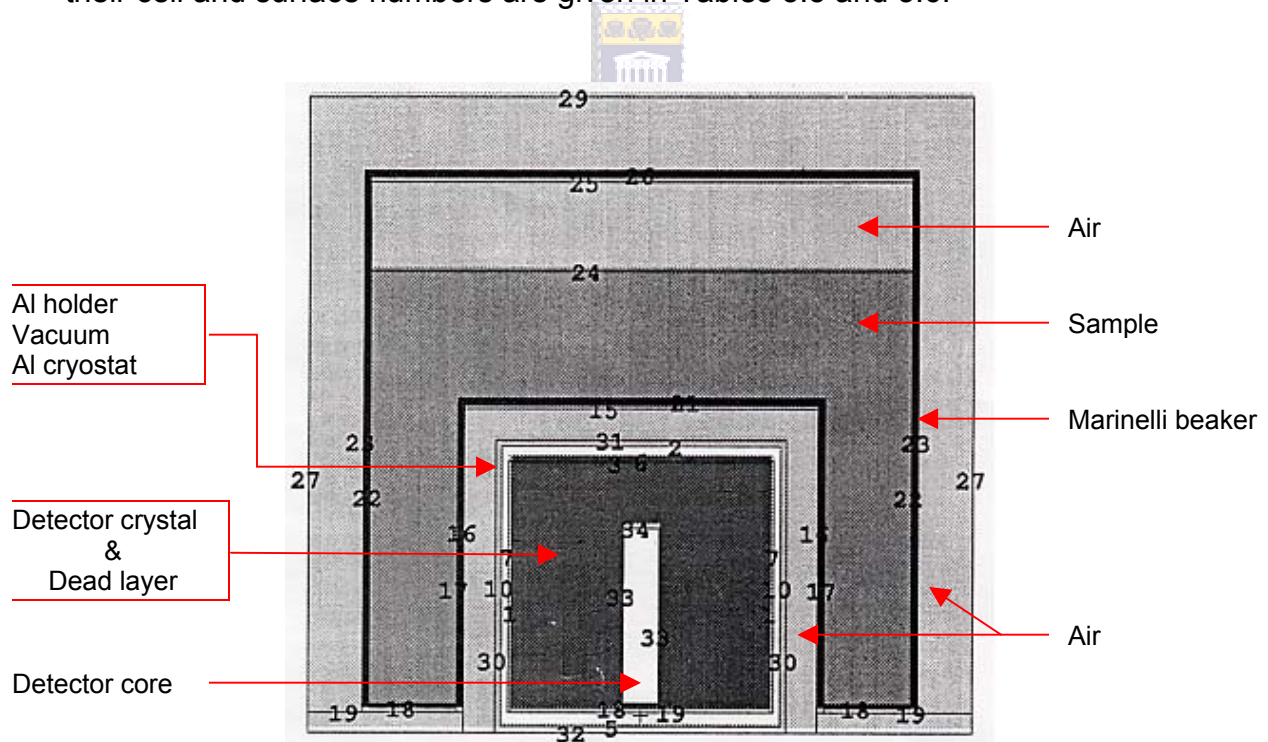
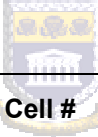


Figure 3.16 : Schematic of close geometry used in simulations (numbers indicate surfaces defined in MCNPX).



Component	Dimension	Cell #	surface #
Core diameter	0.85 cm	14	18, 33, 34
Core depth	4.40 cm	14	18, 33, 34
Ge crystal diameter	6.25 cm	1	1, 3, 18, 33, 34
Ge crystal length	5.95 cm	1	1, 3, 18, 33, 34
Ge dead layer	0.5 mm	3	1, 3, 4, 6, 18, 19
Al cap	0.76 mm	4	4, 6, 7, 19
Vacuum	3.5 mm	5	2, 5, 6, 7, 10, 19
Al cryostat	1.5 mm	13	2, 5, 10, 30, 31, 32

*Table 3.5: Dimensions of the HPGe detector used in simulations [Can99].*



Component	Dimension	Cell #	surface #
Bore diameter	8.5 cm	2	16
Bore depth	7.6 cm	2	15, 32
Beaker diameter	13.2 cm	9	23
Beaker length	13.0 cm	9	18, 19
Beaker walls	0.18 cm	6, 7, 8	16, 17, 18, 20, 21, 22, 23, 25, 26

*Table 3.6: Dimensions of the Marinelli beaker used in the simulations [Iso98].*

### 3.3.2 Soil and sand

Two samples were used in this study, which we refer to as soil (from a vineyard) and sand (from a beach) for convenience. These samples were not analysed chemically to determine their elemental composition and therefore, generic soil compositions were used in the simulations. The generic compositions of the soils used are given in Tables 3.7 and 3.8.

Element	Z number	Weight %	Element	Z number	Weight %
<b>H</b>	1	0.37	<b>Al</b>	13	7.73
<b>C</b>	6	1.28	<b>Si</b>	14	27.91
<b>O</b>	8	49.91	<b>K</b>	19	2.66
<b>Na</b>	11	0.67	<b>Ca</b>	20	3.43
<b>Mg</b>	12	1.57	<b>Fe</b>	26	4.47

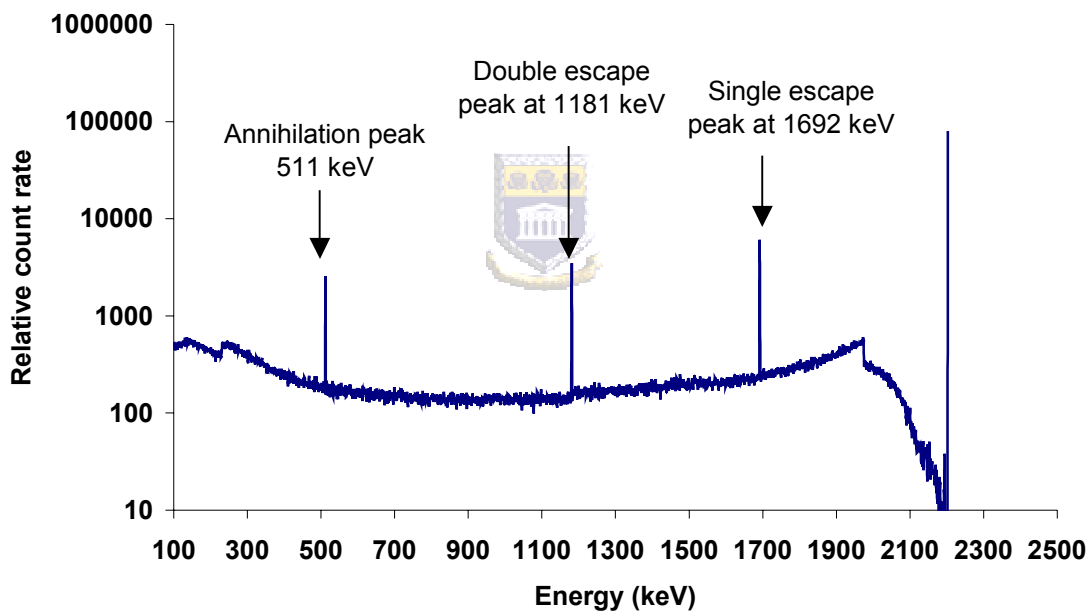
Table 3.7: Composition of generic soil 1 used in simulations [Gar71].



Element	Z number	Weight %	Element	Z number	Weight %
<b>C</b>	6	2.10	<b>Si</b>	14	32.70
<b>N</b>	7	0.10	<b>K</b>	19	0.90
<b>O</b>	8	50.10	<b>Ca</b>	20	1.40
<b>Na</b>	11	0.60	<b>Ti</b>	22	0.40
<b>Mg</b>	12	0.50	<b>Fe</b>	26	3.90
<b>Al</b>	13	7.30			

Table 3.8: Composition of generic soil 2 used in simulations [Lin79].

The gamma-ray energies that were simulated (Table 4.1) are those associated with the decay of naturally occurring radionuclides  $^{238}\text{U}$ ,  $^{232}\text{Th}$  and  $^{40}\text{K}$ , which are found in all sand and soil samples. Each gamma-ray energy is simulated individually for a specified volume (filling height) and the absolute efficiency for that specific  $\gamma$ -ray energy is determined with the use of the pulse height estimator (section 3.1.4) in MCNPX. The pulse height estimator gives the energy deposited per source particle entering the cell. Figure 3.17 shows the normalised pulse height distribution for the energy (2202.9 keV) of the radionuclide  $^{214}\text{Bi}$ , from the decay series of  $^{238}\text{U}$ , in a generic soil sample of density  $1.2\text{ g.cm}^{-3}$  in a 1 litre Marinelli beaker.



*Figure 3.17: Normalised pulse height distribution as calculated in MCNPX (section 3.1.4) for the energy (2202.9 keV) of the radionuclide  $^{214}\text{Bi}$ , from the decay series of  $^{238}\text{U}$ , in a generic soil sample of density  $1.2\text{ g.cm}^{-3}$  in a 1 litre Marinelli beaker.*

### 3.3.3 KCl

The  $^{40}\text{K}$  spiked matrices (Table 2.3) were simulated in the density range of 0.6 – 1.6  $\text{g}\cdot\text{cm}^{-3}$  to investigate the effect of density on the photopeak efficiency in a close geometry. For each density that was considered, the respective matrices according to their element composition (Table 2.2) were simulated. In the case where the effect of volume on photopeak efficiency was investigated, a KCl sample of density 1.25  $\text{g}\cdot\text{cm}^{-3}$  was simulated at different filling heights (Figure 3.18).

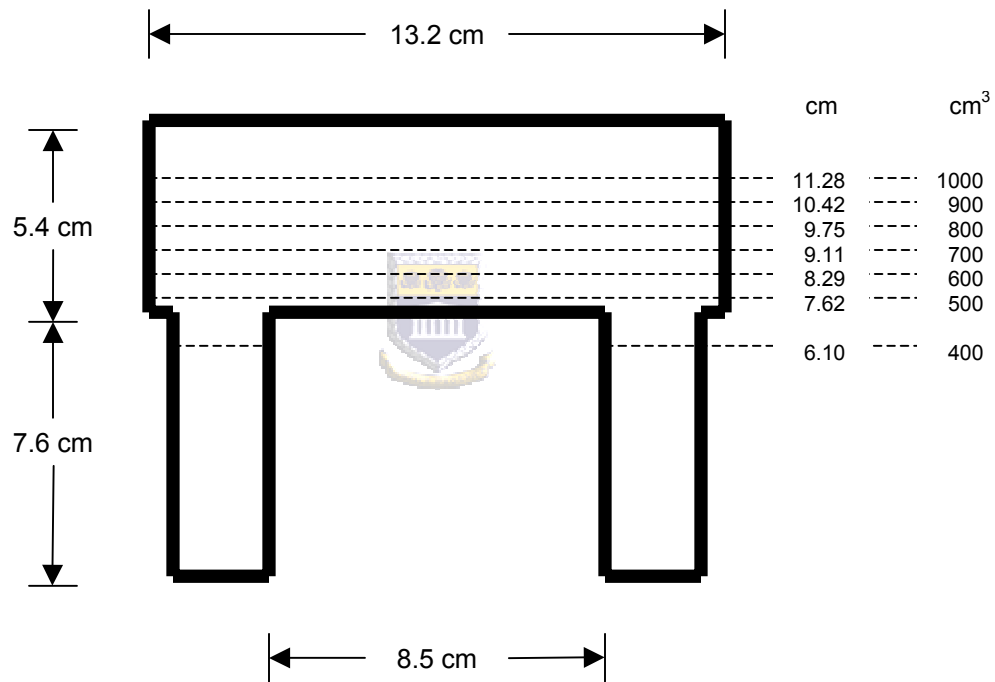


Figure 3.18: Schematic of Marinelli beaker illustrating different filling height.

The simulated spectra for the filling heights of 400 ml and 1000 ml are shown in Figures 3.19 and 3.20, respectively. These spectra also show the double and single escape peaks that have been discussed in section 1.2.3.

400ml KCl in Marinelli beaker (MCNPX)

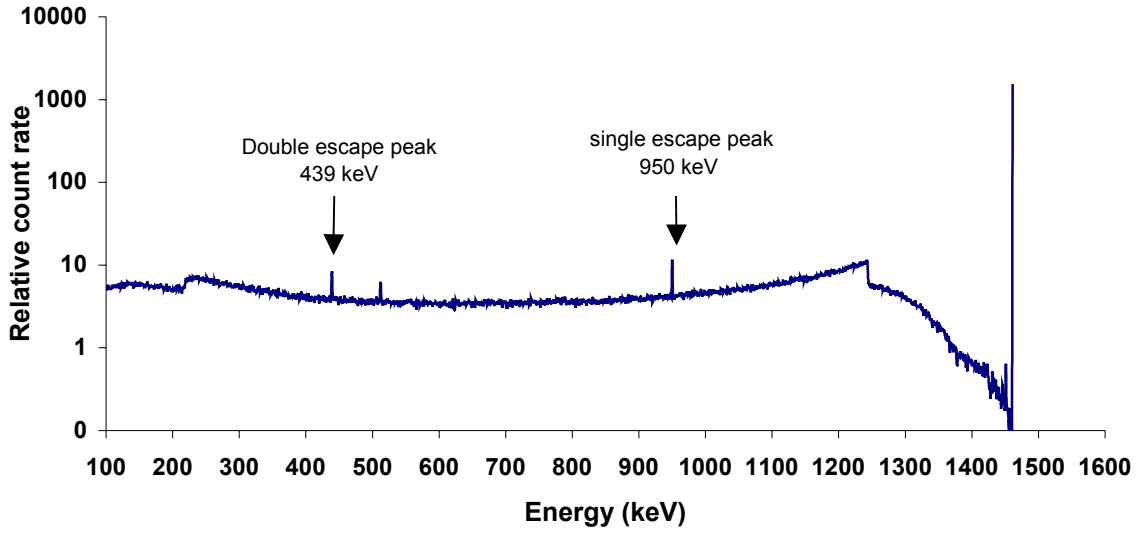


Figure 3.19: Simulated spectrum at 1460.8 keV for 400 ml KCl sample in Marinelli beaker illustrating the double and single escape peaks.

1 litre KCl in Marinelli beaker (MCNPX)

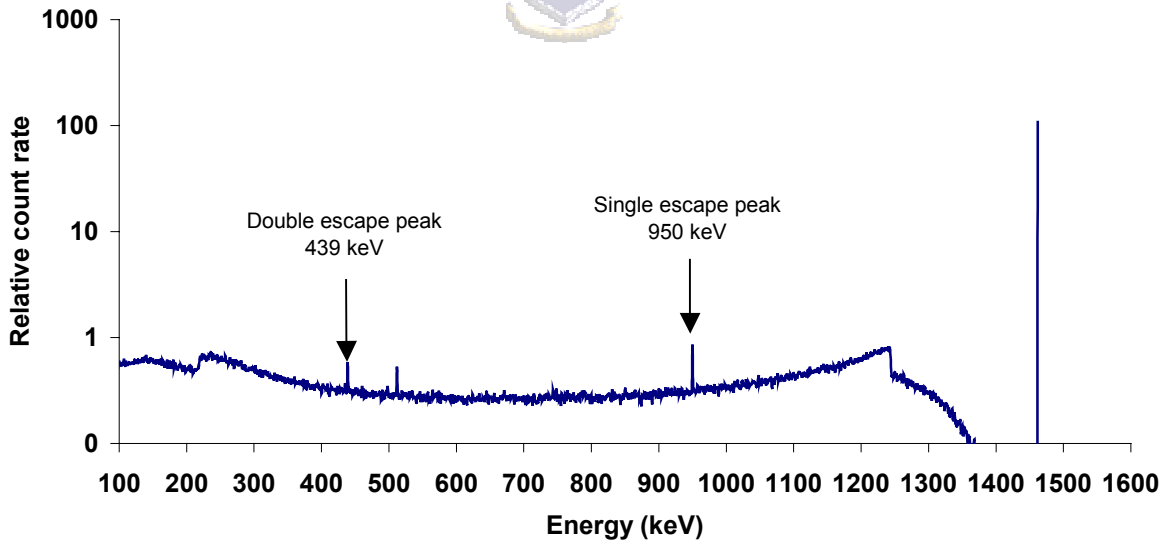


Figure 3.20: Simulated spectrum at 1460.8 keV for 1000 ml KCl sample in Marinelli beaker illustrating the double and single escape peaks.

## Chapter 4

### Experimental results

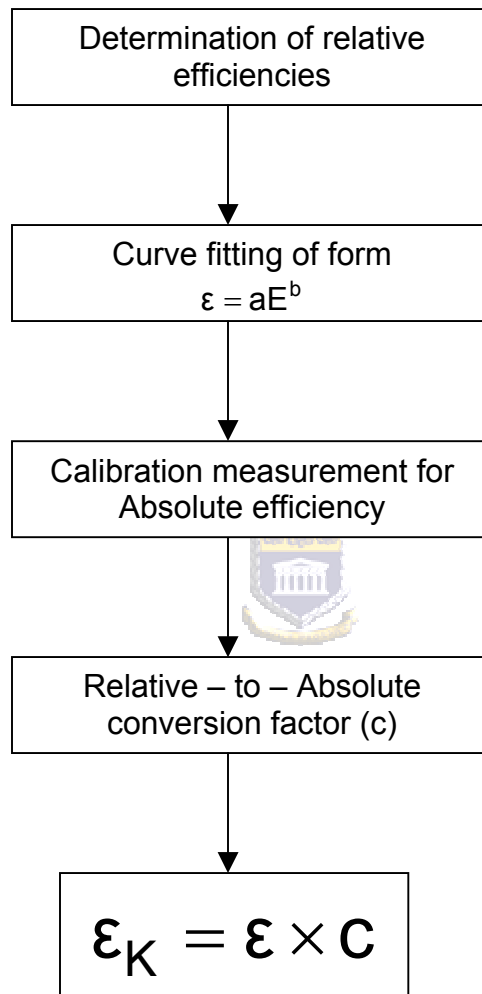
#### 4.1 Soil and sand measurements

##### 4.1.1 Absolute photopeak efficiency

When determining the photopeak efficiency for environmental samples, a correction is made for the background due to cosmic-rays, radioactivity in the surroundings and the contribution from the empty sample beaker (Marinelli beaker), because essentially all materials contain some quantity of natural radioactivity. The activity concentration of  $^{238}\text{U}$ ,  $^{232}\text{Th}$  and  $^{40}\text{K}$  in the soil and sand samples are determined by using the so-called Windows Analysis method [Map05]. The activities are calculated using the following equation:

$$A = \frac{C_n}{mL_T B_r \epsilon_K} \quad (4.1)$$

where  $C_n$  is the photopeak counts associated with the decay of  $^{238}\text{U}$ ,  $^{232}\text{Th}$  or  $^{40}\text{K}$ ,  $m$  is the mass of the sample in kilograms,  $L_T$  is the live time,  $B_r$  is the branching ratio and  $\epsilon_K$  is the photopeak detection efficiency of a particular  $\gamma$ -ray energy. The flow chart in Figure 4.1 illustrates how the photopeak detection efficiency needed in equation 4.1 is determined.



*Figure 4.1: Flowchart illustrating the absolute photopeak efficiency determination procedure.*

First we generate two relative efficiency curves, one based on the  $\gamma$ -ray energies in the decay series of  $^{238}\text{U}$  and the other on the  $\gamma$ -ray energies in the decay series of  $^{238}\text{U} + ^{232}\text{Th}$ . The relative efficiencies of  $^{238}\text{U}$  and  $^{232}\text{Th}$  were determined by normalising the ratio of the photopeak counts for each  $\gamma$ -ray energy to its associated branching ratios with the 352 keV line in the uranium series and 338 keV line in the thorium series respectively. The relative efficiency data is then

fitted with a curve of the form  $\varepsilon = a \left( \frac{E}{E_0} \right)^b$ , where  $E_0 = 1$  keV and the fit parameters are a and b. When taking the logarithm of this equation we obtain:

$$\ln \varepsilon = \ln a + b \ln \left( \frac{E}{E_0} \right) \quad (4.2)$$

The fit parameters generated for the soil sample used in this study are shown in Figure 4.2.

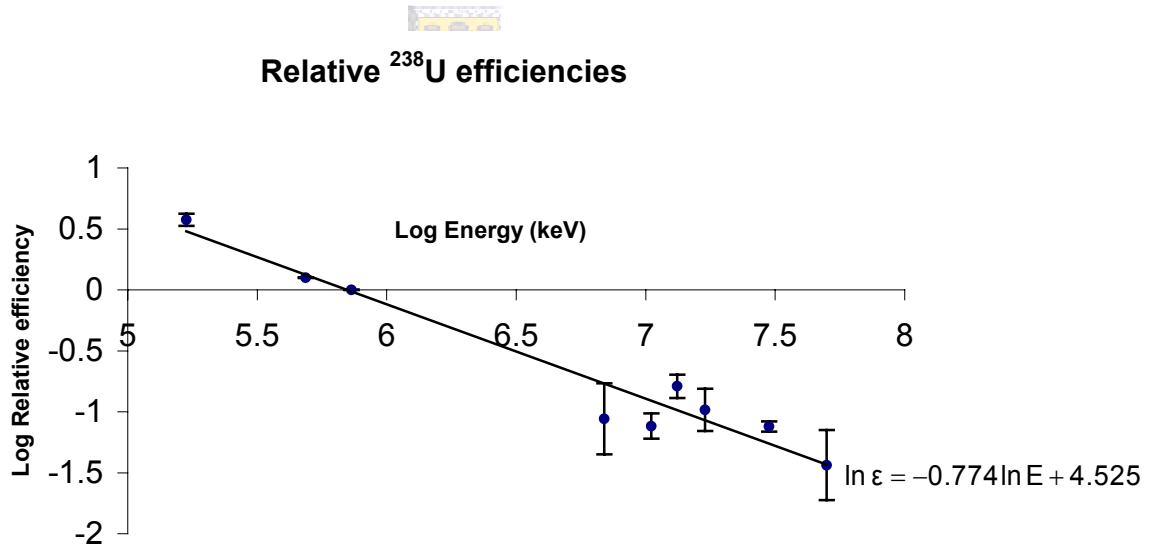


Figure 4.2: Fit to the relative efficiency data as determined from the lines associated with the decay series of  $^{238}\text{U}$  [Mod05]. (showing parameters  $\ln a = 4.525$  and  $b = -0.774$ )



These parameters together with the relative efficiency of  $^{232}\text{Th}$  were used to determine the factor needed to join the thorium to the uranium relative efficiencies [Cro99]. Figure 4.3 shows the relative efficiencies of  $^{238}\text{U} + ^{232}\text{Th}$  and their parameters.

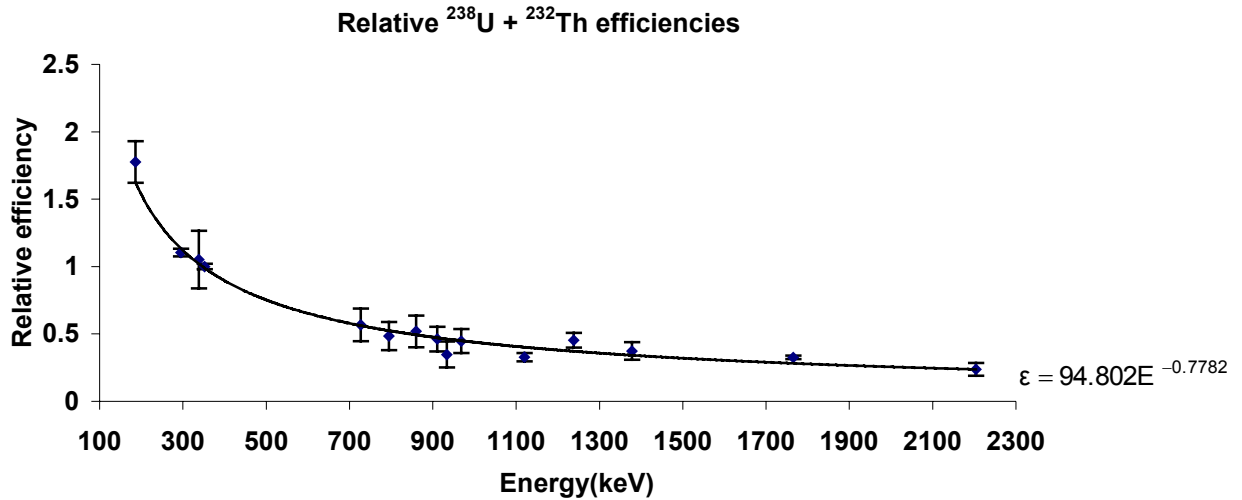


Figure 4.3: Relative efficiency curve of  $^{238}\text{U} + ^{232}\text{Th}$  showing its parameters  $a=94.802$  and  $b=-0.778$  [Mod05].

The next step involves the calibration measurement of the absolute photopeak efficiency and a KCl standard source (Table 4.2) in 1 litre Marinelli beaker. The masses and densities of the soil and sand samples used in this study differ from that of the KCl standard source and therefore an empirically determined density correction was used [Jos05]. This correction was parameterised using the expression given in section 4.2. For each sample, the density corrected absolute photopeak efficiency at 1461 keV was then divided by the relative efficiency and a factor to convert all the relative efficiencies to absolute efficiencies was obtained. The relative efficiency values were then multiplied by this factor to obtain the absolute photopeak efficiencies (Table 4.1). These absolute photopeak efficiencies are plotted in Figure 4.5.

Element	$\gamma$ -ray Energy	Counts	Live Time	Activity	B <sub>r</sub>	efficiency $\epsilon$
<b>Uranium</b>	keV			Bq.kg <sup>-1</sup>		
<sup>228</sup> Ra	*186.1	5543 ± 476	35968.26	42.9 ± 11.4	# 0.062	0.0501 ± 0.0030
<sup>214</sup> Pb	295.2	10337 ± 234	35968.26	42.9 ± 11.4	0.185	0.0313 ± 0.0028
	352.0	18121 ± 258	35968.26	42.9 ± 11.4	0.358	0.0283 ± 0.0026
<sup>214</sup> Bi	933.9	533 ± 147	35968.26	42.9 ± 11.4	0.030	0.0099 ± 0.0017
	1120.4	2452 ± 224	35968.26	42.9 ± 11.4	0.150	0.0092 ± 0.0015
	1238.5	1345 ± 160	35968.26	42.9 ± 11.4	0.059	0.0128 ± 0.0014
	1377.4	741 ± 129	35968.26	42.9 ± 11.4	0.039	0.0106 ± 0.0014
	1765.0	2536 ± 88	35968.26	42.9 ± 11.4	0.154	0.0092 ± 0.0012
	2202.9	584 ± 116	35968.26	42.9 ± 11.4	0.049	0.0067 ± 0.0010
<b>Thorium</b>						
<sup>228</sup> Ac	338.4	9077 ± 420	35968.26	64.1 ± 15.7	0.113	0.0301 ± 0.0026
<sup>212</sup> Bi	727.3	2866 ± 225	35968.26	64.1 ± 15.7	0.066	0.0163 ± 0.0019
<sup>228</sup> Ac	795.0	1610 ± 136	35968.26	64.1 ± 15.7	0.043	0.0140 ± 0.0018
<sup>208</sup> Tl	860.3	1794 ± 199	35968.26	64.1 ± 15.7	0.045	0.0150 ± 0.0017
<sup>228</sup> Ac	911.1	9426 ± 267	35968.26	64.1 ± 15.7	0.266	0.0133 ± 0.0017
	968.1	7302 ± 223	35968.26	64.1 ± 15.7	0.213	0.0129 ± 0.0016
<b>Potassium</b>						
	1460.8	9976 ± 172	35968.26	238.8 ± 6.6	0.107	0.0094 ± 0.0017

# This value is corrected for the contribution from <sup>235</sup>U.

Table 4.1: Some gamma-ray energies of naturally occurring radionuclides in soil. The entry marked \* is an energy peak consisting of a doublet.

The natural gamma-ray energies that were looked at in this study, are for the radionuclides <sup>238</sup>U, <sup>232</sup>Th and <sup>40</sup>K and their daughters. These gamma-ray are presented in Figure 4.4 and Table 4.1.

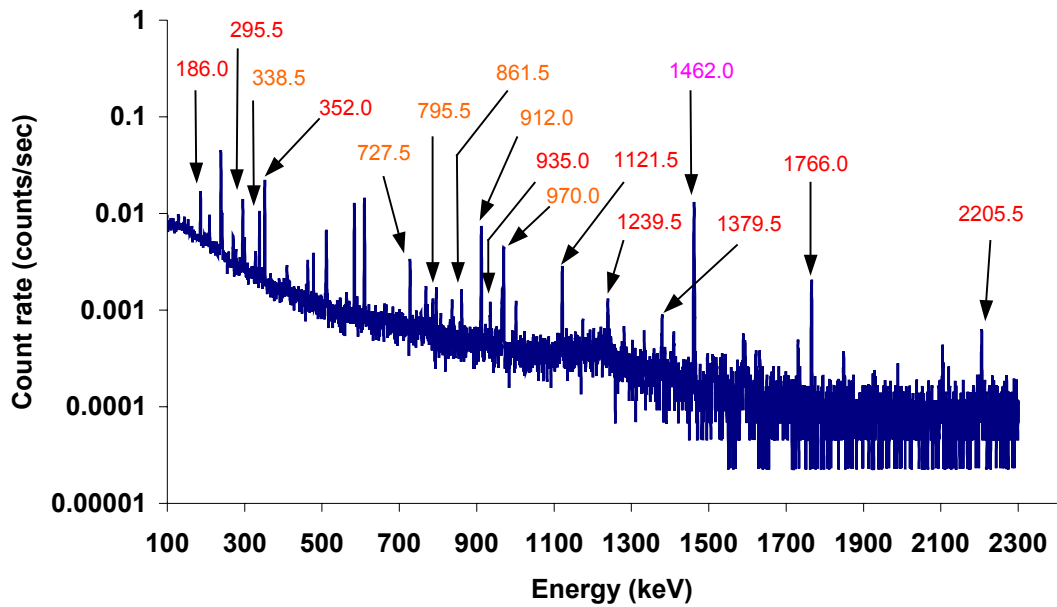


Figure 4.4: Location of peaks in soil sample for the radionuclides  $^{238}\text{U}$ ,  $^{232}\text{Th}$  and  $^{40}\text{K}$ .



Absolute efficiency curve for soil sample

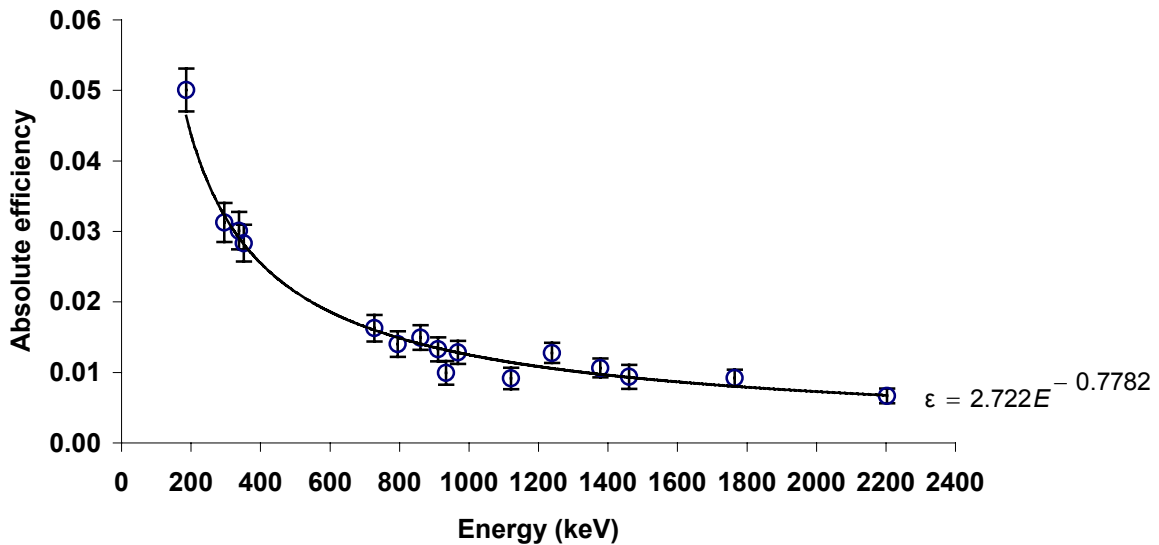


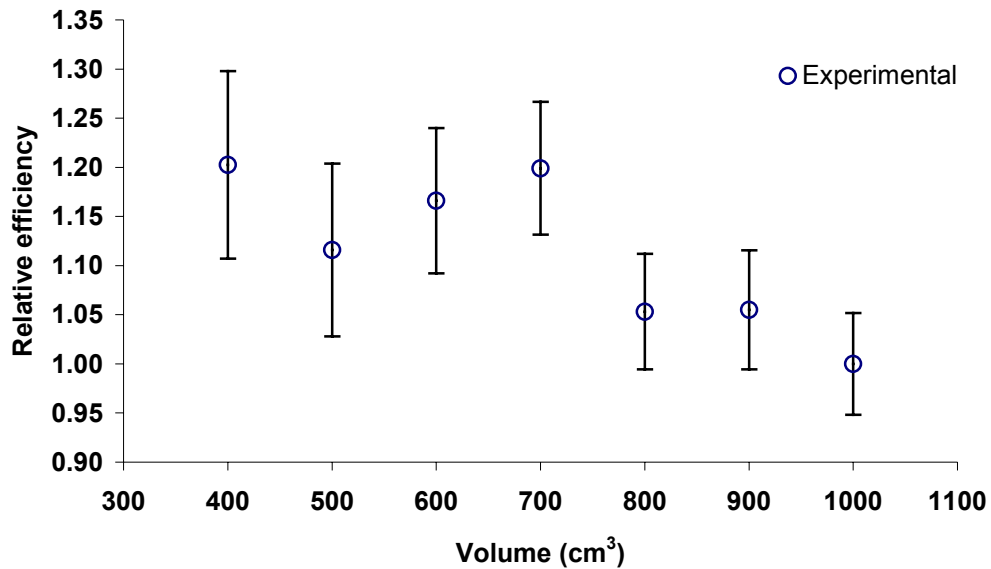
Figure 4.5: Absolute efficiency curve of soil sample showing its parameters  $a=2.722$  and  $b=-0.778$  [Mod05].

#### 4.1.2 Volume effect

In order to investigate the effect of volume on photopeak efficiency, a beach sand sample was measured at 100 ml increments, starting from 400 ml up to and including 1000 ml. Table 4.2 shows the 1460.8 keV photopeak counts (after appropriate background subtraction) for the beach sand sample and the data used to determine the relative photopeak efficiency at different filling heights. These relative photopeak efficiencies were determined by taking the ratio of the photopeak counts to the mass of the sample at each filling height. These values were then normalised to the value at 1000 ml and then plotted in Figure 4.6. The live time, branching ratio and activity of the sand sample are considered to be constant.

Volume	Mass	Counts	Lt	Relative efficiency
ml	kg			$\epsilon$
400	0.67137	1236 $\pm$ 87	43193.91	1.202 $\pm$ 0.095
500	0.83009	1418 $\pm$ 99	43191.40	1.116 $\pm$ 0.088
600	1.00562	1795 $\pm$ 93	43192.84	1.166 $\pm$ 0.074
700	1.32650	2079 $\pm$ 89	43191.52	1.200 $\pm$ 0.068
800	1.32297	2133 $\pm$ 90	43191.20	1.053 $\pm$ 0.059
900	1.38459	2236 $\pm$ 99	43192.07	1.055 $\pm$ 0.061
1000	1.62588	2489 $\pm$ 91	43191.68	1.000 $\pm$ 0.052

*Table 4.2: Summary of data on beach sand samples at different volumes. The relative efficiency values are normalised to 1000 ml.*



*Figure 4.6: Relative efficiency curve as a function of volume for beach sand sample.*



To further investigate the effect of volume on the absolute photopeak efficiency, other gamma lines of the decay series of  $^{238}\text{U}$  ( $5.1 \pm 1.5 \text{ Bq.kg}^{-1}$ ) and  $^{232}\text{Th}$  ( $5.2 \pm 1.5 \text{ Bq.kg}^{-1}$ ), together with the  $^{40}\text{K}$  ( $35.3 \pm 1.5 \text{ Bq.kg}^{-1}$ ) gamma line was also looked at in the different volumes. The efficiencies for these gamma lines were also obtained using equation 4.1. The gamma energies that were looked at, together with their efficiencies at the different volumes are presented in Table 4.3 and plotted in Figure 4.7.

Energy keV	Volume (ml)					
	500	600	700	800	900	1000
	$\epsilon$	$\epsilon$	$\epsilon$	$\epsilon$	$\epsilon$	$\epsilon$
186	$0.069 \pm 0.003$	$0.072 \pm 0.008$	$0.062 \pm 0.005$	$0.049 \pm 0.002$	$0.042 \pm 0.002$	$0.029 \pm 0.002$
352	$0.040 \pm 0.002$	$0.041 \pm 0.006$	$0.035 \pm 0.003$	$0.031 \pm 0.001$	$0.027 \pm 0.001$	$0.021 \pm 0.001$
795	$0.020 \pm 0.001$	$0.020 \pm 0.003$	$0.017 \pm 0.002$	$0.017 \pm 0.001$	$0.015 \pm 0.001$	$0.013 \pm 0.001$
934	$0.017 \pm 0.001$	$0.017 \pm 0.003$	$0.014 \pm 0.002$	$0.0149 \pm 0.0004$	$0.014 \pm 0.001$	$0.012 \pm 0.001$
1460	$0.0118 \pm 0.0002$	$0.0116 \pm 0.0002$	$0.0111 \pm 0.0002$	$0.0107 \pm 0.0002$	$0.0099 \pm 0.0002$	$0.0094 \pm 0.0002$

Table 4.3: The natural gamma energies and absolute photopeak efficiencies for different volumes of the sand sample.

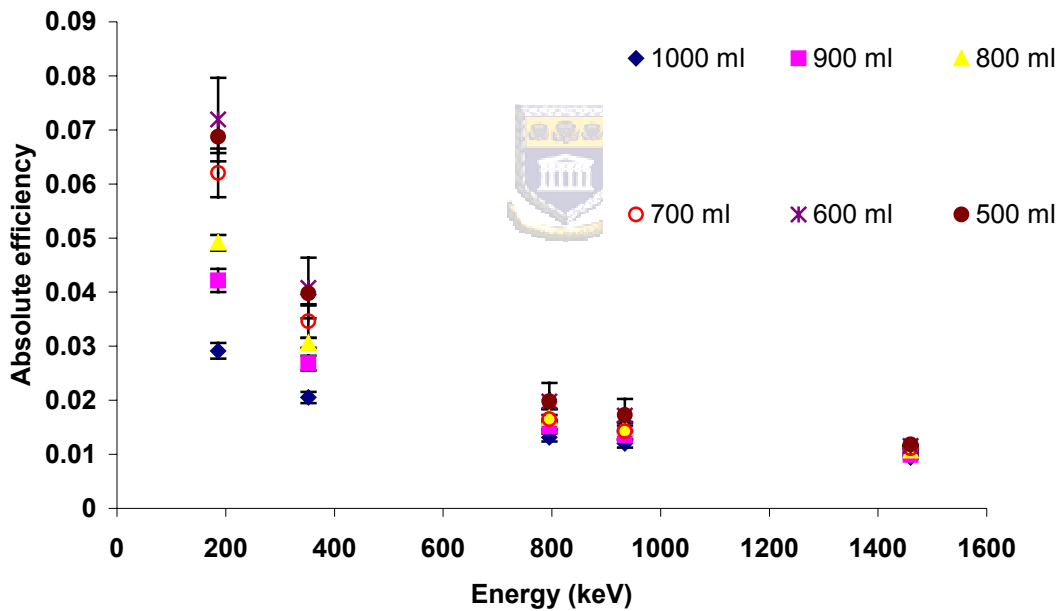



Figure 4.7: Absolute efficiency curves for the natural gamma energies at different volumes.

## 4.2 KCl measurements

### 4.2.1 Volume effect

To investigate the volume effect, the 1460.8 keV gamma – ray of  $^{40}\text{K}$  was looked at in a standard KCl source of density  $1.25 \text{ g.cm}^{-3}$ . This radionuclide was chosen because the  $^{40}\text{K}$  line is used in our analysis to set the photopeak efficiency on an absolute scale (section 4.1.1). The samples are assumed to be homogeneously distributed throughout the beaker. Each 100 ml increment volume of sample was measured in a measuring cylinder and transferred to the Marinelli beaker to obtain the different filling volumes; thereafter the heights were measured with a vernier callipers (Table 4.4). Table 4.4 shows the activity concentration determined for the KCl standard and the data used to determine the photopeak efficiency at different filling heights. The activity concentration of KCl was calculated with the use of the following equation:


$$\text{Activity} = \frac{M_{\text{KCl}}}{MM_{\text{KCl}}} \times \lambda \times N_{\text{A}} \times A \quad (4.3)$$

where

$M_{\text{KCl}}$  = mass of KCl sample,

$MM_{\text{KCl}}$  = molar mass of KCl = 74.551 g,

$\lambda$  = decay constant =  $1.72 \times 10^{-17} \text{ s}^{-1}$ ,

$A$  = Abundance of  $^{40}\text{K}$  =  $1.17 \times 10^{-4}$ ,

$N_{\text{A}}$  = Avogadro's number.

The photopeak efficiencies as a function of volume are plotted in Figure 4.8.

Height	Volume	KCl mass	Counts	Live Time	Activity	Experimental efficiency
cm	ml	g			Bq	$\epsilon$
6.10	400	492.23	18216 $\pm$ 138	1795.68	8002 $\pm$ 85	0.0119 $\pm$ 0.0002
7.62	500	589.83	21662 $\pm$ 152	1794.89	9588 $\pm$ 102	0.0118 $\pm$ 0.0002
8.29	600	766.51	27533 $\pm$ 169	1794.30	12460 $\pm$ 132	0.0115 $\pm$ 0.0002
9.11	700	870.39	30087 $\pm$ 179	1792.90	14149 $\pm$ 150	0.0111 $\pm$ 0.0002
9.75	800	995.18	33122 $\pm$ 192	1792.17	16177 $\pm$ 171	0.0107 $\pm$ 0.0002
10.42	900	1122.41	17260 $\pm$ 137	896.91	18246 $\pm$ 193	0.0099 $\pm$ 0.0002
11.28	1000	1274.14	18606 $\pm$ 141	895.50	20712 $\pm$ 219	0.0094 $\pm$ 0.0002

Table 4.4: Absolute efficiency and filling heights for KCl standard source at different volumes [Jos05].

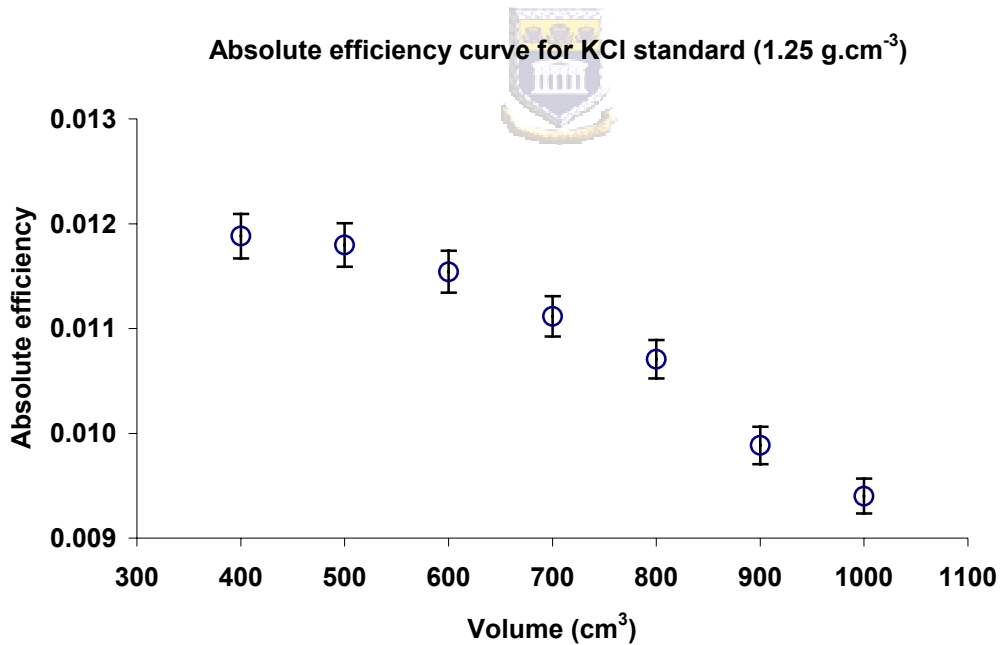


Figure 4.8: Absolute efficiency curve for KCl standard as a function of volume [Jos05].



## 4.2.2 Density effect

The absolute efficiency curve for the  $^{40}\text{K}$  standards (section 2.2.2) as a function of density is presented in Figure 4.9, where a simple power law relationship was fitted to the experimental data presented in Table 4.5. The power law is given by

$$\varepsilon_k = a \times \rho^b$$

where  $\varepsilon_k$  is the  $^{40}\text{K}$  absolute efficiency (Table 4.5),  $\rho$  is the sample density,  $a = 0.009 \pm 0.0002$  and  $b = -0.048 \pm 0.003$  [Jos05].

Code	Density ( $\text{g}\cdot\text{cm}^{-3}$ )	Efficiency $\varepsilon_k$
Stearic	0.66	$0.0092 \pm 0.0002$
Starch	0.86	$0.0090 \pm 0.0002$
Gypsum	0.94	$0.0090 \pm 0.0002$
Quartz	1.60	$0.0088 \pm 0.0002$

Table 4.5: Absolute efficiency values for  $^{40}\text{K}$  standards at different densities.

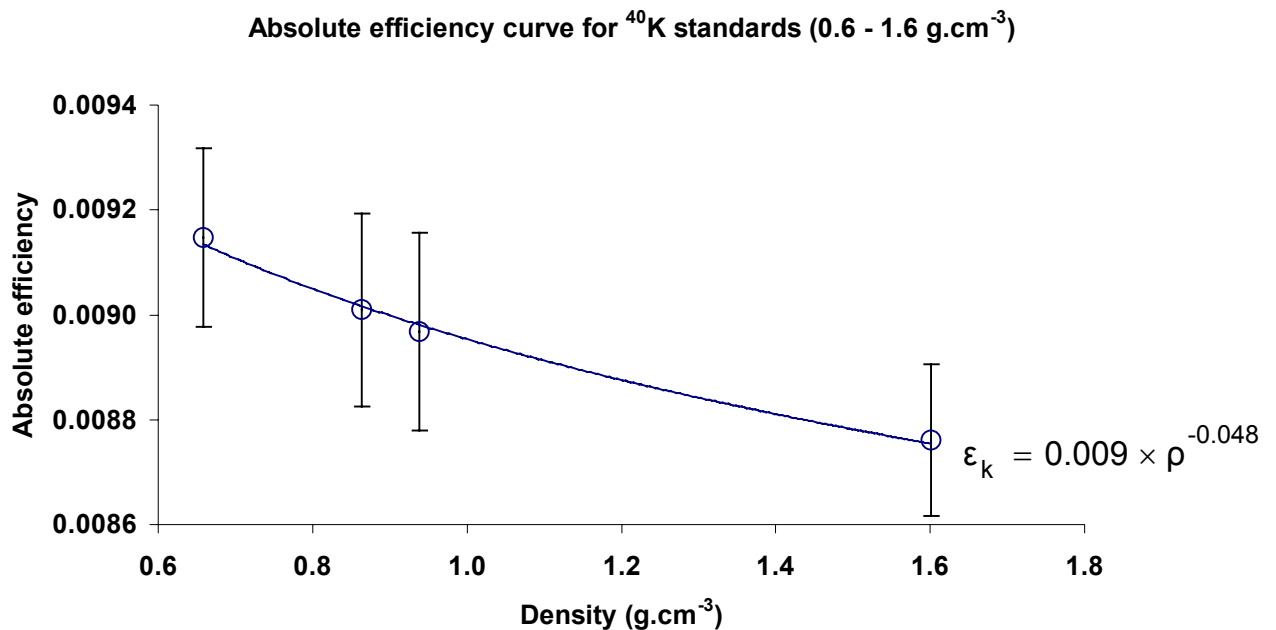


Figure 4.9: The measured absolute efficiency curve for  $^{40}\text{K}$  standards at different densities [Jos05].

### 4.3 Liquid source

#### 4.3.1 Absolute photopeak efficiency – CSIR standard liquid source

The peaks used from the liquid standard spectrum obtained in August 2004, are shown in Figure 4.10. These  $\gamma$ -ray energies are associated with the radionuclides  $^{152}\text{Eu}$ ,  $^{60}\text{Co}$  and  $^{137}\text{Cs}$  (Table 4.6). The lowest  $\gamma$ -ray energy considered in this study was 121.8 keV because the absolute efficiency for this energy lies just below the turnover region on the absolute photopeak efficiency curve of Figure 5.3.

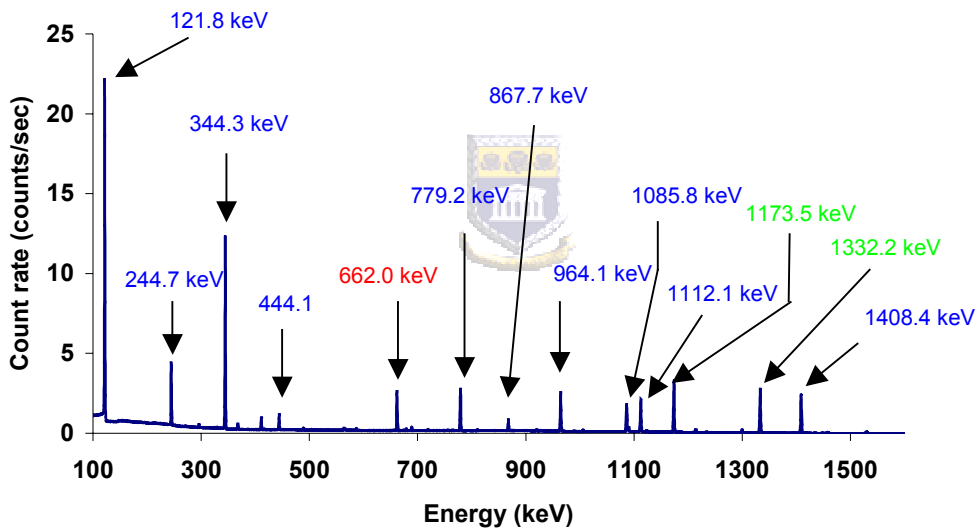


Figure 4.10: Location of peaks in the liquid standard that were used in efficiency determination.

The activity for each nuclide was corrected for decay since preparation of the source and is given in Table 4.6.

$\gamma$ – ray Energy (keV)	Nuclides	Ref.	Activity (Bq)	Current Activity (10-Aug-04) (Bq)
121.8	<sup>152</sup> Eu	NDS89	6550 ± 197	5739.86 ± 172
244.9	<sup>152</sup> Eu	NDS89	6550 ± 197	5739.86 ± 172
344.6	<sup>152</sup> Eu	NDS89	6550 ± 197	5739.86 ± 172
444.1	<sup>152</sup> Eu	NDS90	6550 ± 197	5739.86 ± 172
662.0	<sup>137</sup> Cs	Fir96	661 ± 13	622.88 ± 13
779.2	<sup>152</sup> Eu	NDS89	6550 ± 197	5739.86 ± 172
867.7	<sup>152</sup> Eu	NDS89	6550 ± 197	5739.86 ± 172
964.1	<sup>152</sup> Eu	NDS89	6550 ± 197	5739.86 ± 172
1085.8	<sup>152</sup> Eu	NDS89	6550 ± 197	5739.86 ± 172
1112.1	<sup>152</sup> Eu	NDS89	6550 ± 197	5739.86 ± 172
1173.5	<sup>60</sup> Co	Fir96	1907 ± 38	1359.65 ± 27
1332.8	<sup>60</sup> Co	Fir96	1907 ± 38	1359.65 ± 27
1408.4	<sup>152</sup> Eu	NDS89	6550 ± 197	5739.86 ± 172

*Table 4.6:  $\gamma$ -ray energies and corrected activity concentration values (10-Aug-04) for the decay of radionuclides in the standard liquid source.*

The absolute photopeak efficiencies were then calculated with these corrected activities (Table 4.7) by means of equation 2.1 and a functional curve of the form  $\varepsilon = 0.92987 E^{-0.6325}$  was then fitted to the efficiency data and plotted in Figure 4.11.

<b><math>\gamma</math> – ray Energy (keV)</b>	<b>Counts</b>	<b>Live Time</b>	<b>Br</b>	<b><math>\varepsilon</math></b>
121.8	717190 $\pm$ 1575	11089.96	0.2843	0.040 $\pm$ 0.001
244.9	142190 $\pm$ 939	11089.96	0.0749	0.030 $\pm$ 0.001
344.6	441008 $\pm$ 1039	11089.96	0.2658	0.026 $\pm$ 0.001
444.1	38916 $\pm$ 498	11089.96	0.0309	0.020 $\pm$ 0.001
662.0	98466 $\pm$ 568	11089.96	0.8510	0.0168 $\pm$ 0.0004
779.2	115617 $\pm$ 651	11089.96	0.1296	0.0140 $\pm$ 0.0004
867.7	32529 $\pm$ 485	11089.96	0.0415	0.0123 $\pm$ 0.0004
964.1	113496 $\pm$ 581	11089.96	0.1447	0.0123 $\pm$ 0.0004
1085.8	62289 $\pm$ 620	11089.96	0.1016	0.0096 $\pm$ 0.0003
1112.1	99166 $\pm$ 501	11089.96	0.1355	0.0115 $\pm$ 0.0004
1173.5	157289 $\pm$ 529	11089.96	0.9990	0.0104 $\pm$ 0.0002
1332.8	143498 $\pm$ 427	11089.96	0.9998	0.00952 $\pm$ 0.0002
1408.4	126778 $\pm$ 392	11089.96	0.2087	0.00954 $\pm$ 0.0003

*Table 4.7: Associated branching ratios of radionuclides [Fir96] and photopeak efficiencies obtained using equation 2.1.*

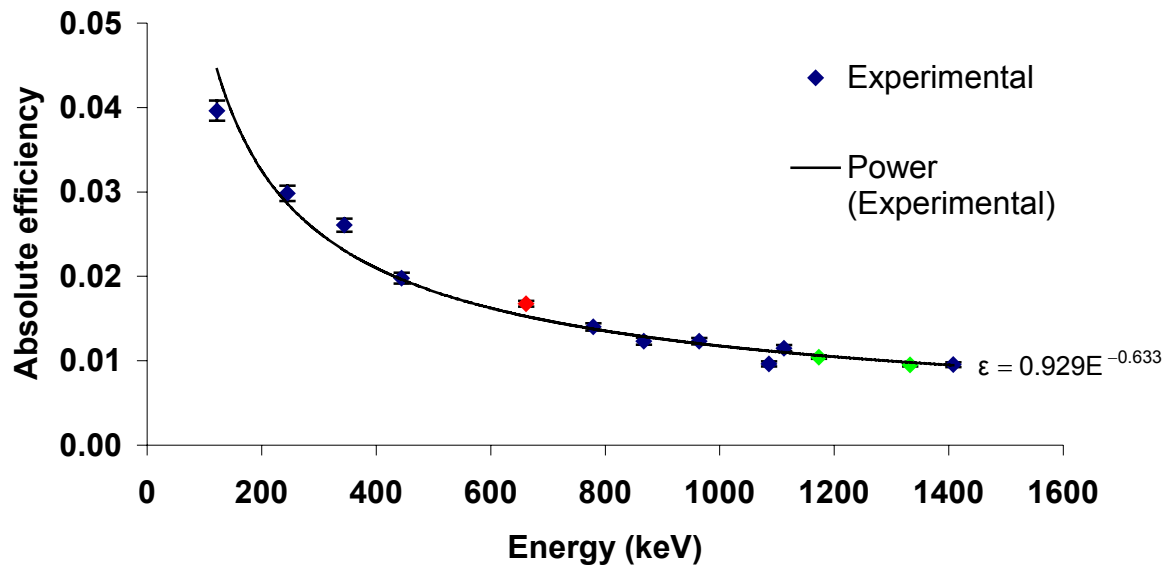


Figure 4.11: Absolute efficiency curve fitted through experimental values measured using the liquid standard source, showing parameters  $a = 0.929$  and  $b = -0.633$ . The data points are associated with the decay of  $^{60}\text{Co}$ ,  $^{137}\text{Cs}$  and  $^{152}\text{Eu}$ .



## Chapter 5

### Results and Discussion

The results of the MCNPX simulations will be presented in this chapter and compared to the experimental results. In general the simulations predict efficiencies larger than experimental results. Reasons for this will be studied.

#### 5.1.1 Liquid Source

The experimental and simulated absolute efficiency curves for the standard liquid source containing the radionuclides  $^{60}\text{Co}$ ,  $^{137}\text{Cs}$  and  $^{152}\text{Eu}$  are presented in Figure 5.1.

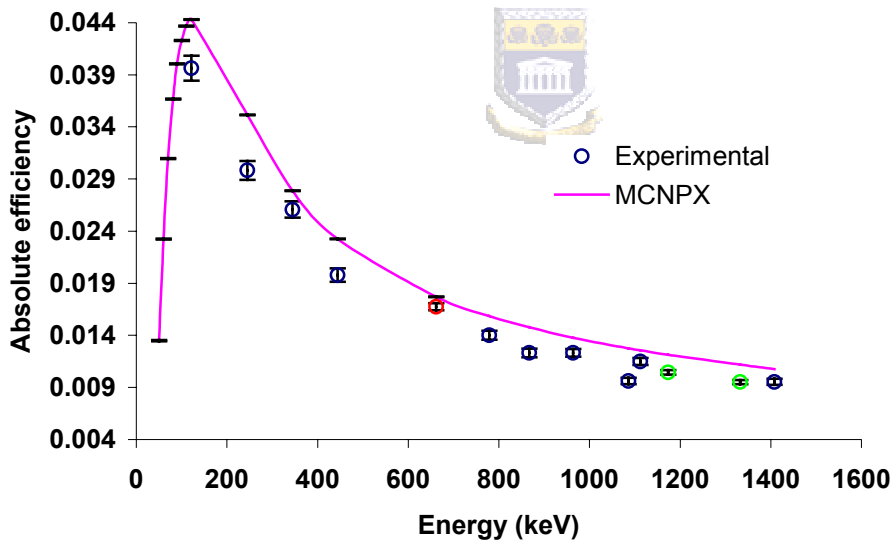
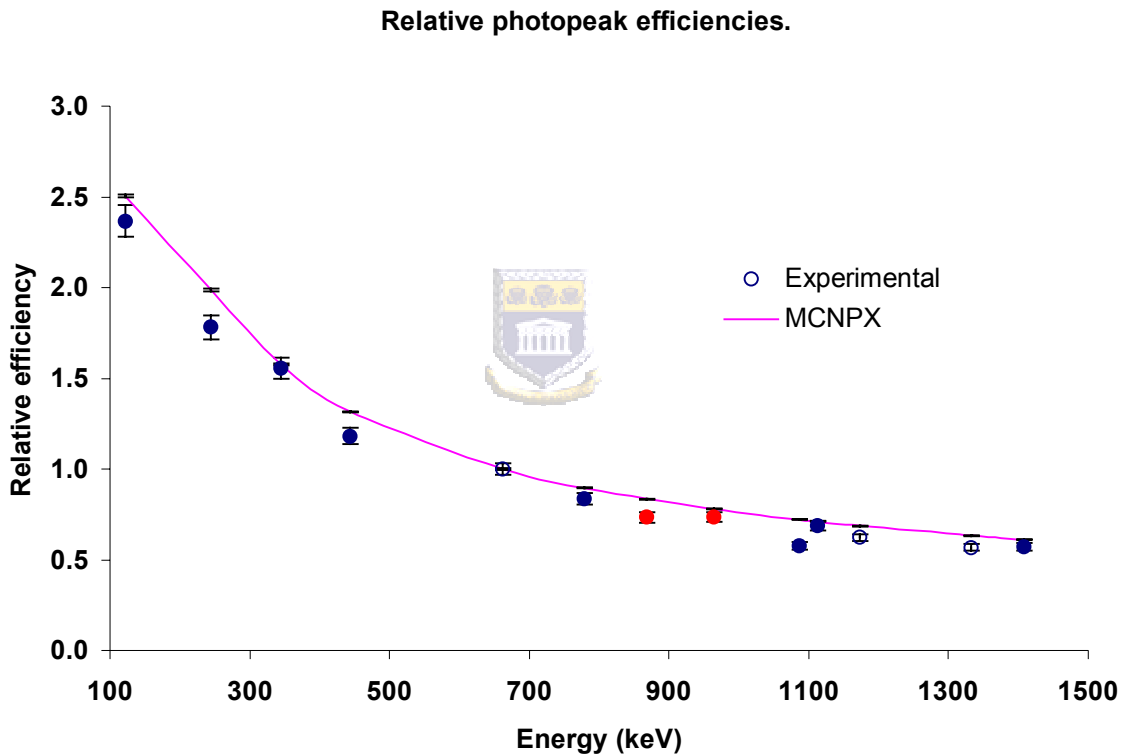


Figure 5.1: Absolute photopeak efficiency curve showing the turnover region. The data points are associated with the decay of  $^{60}\text{Co}$ ,  $^{137}\text{Cs}$  and  $^{152}\text{Eu}$ .

The ratio of the absolute photopeak efficiencies for each curve with respect to the respective 662 keV absolute photopeak efficiency value (from the  $^{137}\text{Cs}$  decay scheme) was plotted to obtain the relative photopeak efficiency curve of Figure 5.2. The 662 keV efficiency value was chosen because it is the only gamma-ray line from the  $^{137}\text{Cs}$  decay scheme and there is good agreement between the simulated and experimental absolute photopeak efficiency values at this gamma energy. This was done in order to determine the extent of the effect that coincidence summing has on determining accurate absolute efficiency values.



*Figure 5.2: Relative photopeak efficiency curve with respect to the 662 keV efficiency value. The filled circles show those lines, which are prone to coincidence summing.*

The filled circles represent those lines, which are prone to coincidence summing [Gil95]. The blue circles show the lines that sum to give sharp peaks (Figure 5.4), whereas the red circles show lines that are prone to summing in (i.e. summing that contributes to a photopeak). The discrepancy in the two remaining lines at 1173.2 keV and 1332.5 keV shows evidence of summing out. The discrepancy due to summing out for these two gamma lines is in good agreement with the findings of Garcia-Torano [Tor05], who found that the correction factor for these gamma energies are in the order of 10 % for liquid samples (see discussion in Appendix D).

The complex decay scheme of  $^{152}\text{Eu}$  was considered in the standard liquid source because it involves a number of gamma emissions and is known to undergo coincidence summing [Gil95]. Nuclei of  $^{152}\text{Eu}$  decay either by  $\beta^-$  decay and become  $^{152}\text{Gd}$  or, more likely (72.08 % of the time) undergo electron capture and become  $^{152}\text{Sm}$  (Figure 5.3). In either mode of decay the daughter nucleus then de-excites by emitting a number of gamma-rays until a stable nucleus is formed. The lifetime of the discrete nuclear levels is much shorter than the resolving time of the spectrometer system. Therefore, each decay of a  $^{152}\text{Eu}$  atom in the source will release a number of gamma-rays and possibly X-rays and there is a high probability that the detector will detect more than one of these within the resolving time of the detector. When this occurs a pulse is recorded which represents the sum of the energies deposited in the detector. This is called coincidence summing out, which like for random summing, the event results in the loss of counts from the photopeak and therefore a loss of photopeak efficiency [Gil95].

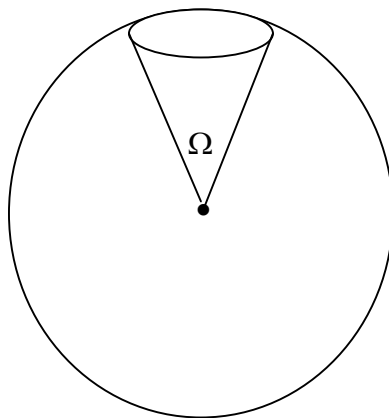
The degree of coincidence summing depends upon the probability that two or more  $\gamma$ -rays emitted “simultaneously” will be detected as one count by the detector. However, unlike random summing, which is count rate dependent, coincidence summing is geometry dependent and errors are particularly severe when the sources are positioned very close to the detector [Jos05]. The number



of coincidence summing events per second will be proportional to the sample activity for a given solid angle i.e. angle subtended at the detector by the source. For any source to detector distance there will be some degree of summing. This is shown in the following illustration.

The probability of detecting a gamma – ray after passing through a thickness (d) of the detector material is  $P_n(\text{det}) = 1 - P_n(d) = 1 - e^{-\mu_n d}$ , where  $n = 1, 2, \dots$  denotes the gamma-ray. For an isotropically emitting point source and uncorrelated  $\gamma$ -rays:

$$P(\Omega) = \frac{\Omega}{4\pi}$$



where  $\Omega$  is the solid angle of the detector (section 1.2.5). Therefore the probability of detecting coincidence summing (cs) is;

$$\begin{aligned} P(\text{cs}) &= P_1(\text{det}) P_1(\Omega) \cdot P_2(\text{det}) P_2(\Omega) \\ &= P_1(\text{det}) P_2(\text{det}) \cdot \frac{\Omega^2}{(4\pi)^2} \\ &= \left(1 - e^{-\mu_1 d}\right) \cdot \left(1 - e^{-\mu_2 d}\right) \cdot \left(\frac{\Omega^2}{(4\pi)^2}\right) \end{aligned}$$

where  $\mu$  is the energy dependent linear attenuation of the detector material. It can be seen from the above equation that, depending on the detector size, beyond a certain distance, coincidence summing losses will be negligible.

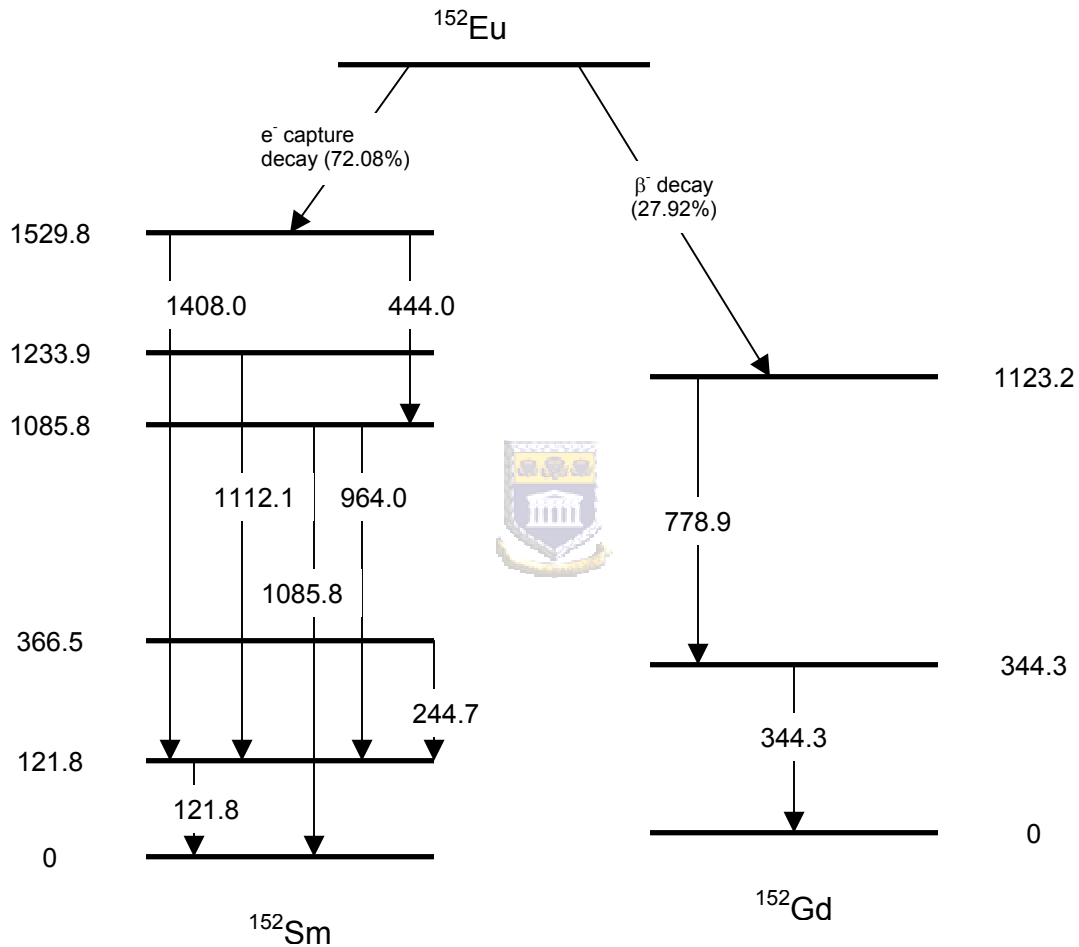
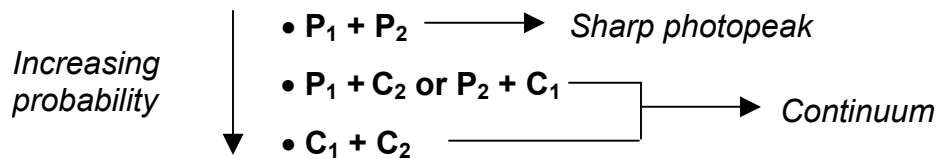


Figure 5.3: Simplified decay scheme for  $^{152}\text{Eu}$  [Fir96].

Since the two branches of the  $^{152}\text{Eu}$  decay scheme (Figure 5.3) are independent of each other, there is no photopeak at 466.06 keV (Figure 5.4), which would indicate summing between the 121.78 keV and 344.28 keV gamma-ray (these originate in different cascades). Each  $\gamma$ -transition produces a photopeak (P) and a Compton continuum (C) with the probability  $P_C \gg P_P$ . However, each summing peak represents only some of the counts lost from the main peaks; this is because there is the possibility of summing in the detector with each and every gamma-ray in the cascade whether or not fully absorbed. There are three types of coincidence summing;



The evidence for coincidence summing is found in the spectrum of the liquid source (Figure 5.4). The photopeaks that are indicated in Figure 5.4 correspond to the combination of gamma-ray lines given in Table 5.1.

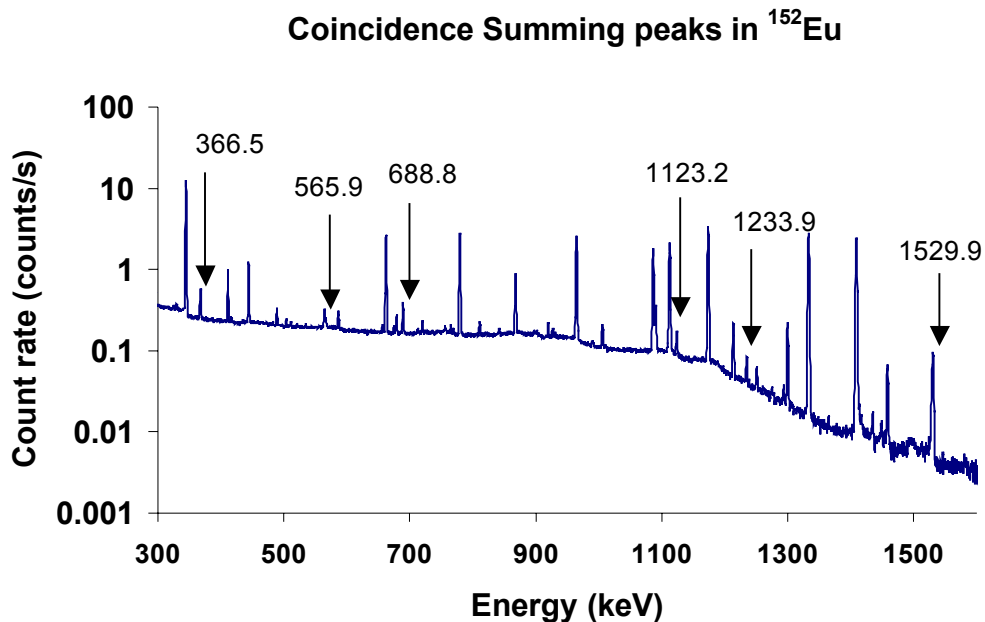



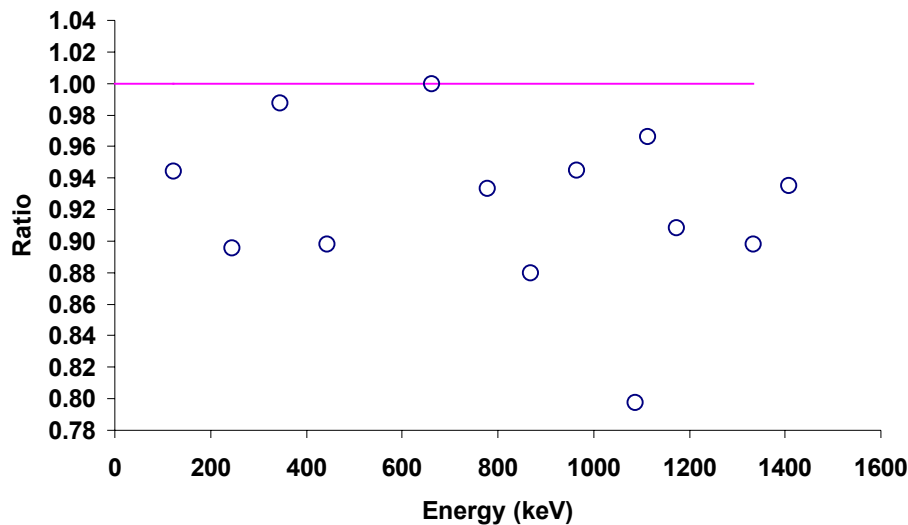
Figure 5.4: Sum peaks in the liquid standard source spectrum due to coincidence summing.

<b>keV</b>	121.8	244.7	344.3	444.1
244.7	366.5			
444.1	565.9	688.8		
778.9			1123.2	
867.4		1112.1		
964.0	1085.8			1408.1
1085.8		1330.5		1529.9
1112.1	1233.9			
1408.0	1529.8			

*Table 5.1: Combinations of gamma-rays (keV) that undergo coincidence summing. The shaded grey boxes indicate those peaks that undergo summing in.*

The essential points of coincidence summing can be summarized as:

- It can be expected whenever nuclides with a complex decay scheme is measured. 
- The degree of summing is not dependent upon count rate.
- It results only for certain peaks, usually in lower photopeak areas.
- It gets worse the closer the source is to the detector.
- It gets worse the larger the detector.
- It is worst of all when using well detectors.
- It may be worse if a detector with a thin window is used because the X-rays, which might contribute to the summing, will penetrate into the detector's active volume.



*Figure 5.5: Ratio of experimental to simulated relative photopeak efficiency values.*

It is evident from Figure 5.5 that there is a deviation of up to 12 % between simulated and experimental values (except for the efficiency at 1085.8 keV). This may largely be due to the fact that there is a systematic problem in the simulations, since it may miss some important information on the precise details of the detector (section 5.1.2) and also due to coincidence summing. Apart from those gamma lines shown in Table 5.1, the 121.8 keV and 244.7 keV gamma lines, are also prone to summing with the 39.9 keV and 45.4 keV gamma lines in the  $^{152}\text{Eu}$  series [Gil95]. It is evident from Figure 5.5 that the difference between simulated and experimental value for the 344.3 keV and 778.9 keV are less than 8 % and therefore these gamma lines do not need much correction. The difference between simulated and experimental values for the 867.4 keV, 964.0 keV and 1408.0 keV gamma lines can be attributed to summing out (i.e. loss of efficiency/counts from photopeak due to coincidence summing). Although the 1085.5 keV gamma line undergoes summing in, it is evident from Figure 5.5 and Table 5.1 that this gamma line predominately undergoes summing out. For the 1173.2 keV and 1332.5 keV gamma lines of the  $^{60}\text{Co}$  series, Figure 5.5 shows a difference of 9 % and 11 %, respectively, between simulated and experimental

results. This is in good agreement with the findings of Garcia-Torano [Tor05], who found that the correction factor for these gamma energies is of the order of 10 % (see discussion in Appendix D).

### **5.1.2 Sensitivity analysis**

When using MC methods to calculate the photopeak efficiency for volume sources, knowledge of the dimensions of the internal and external parts of the detector and the volume source is required. For manufacturing reasons there is uncertainty in the dimensions for the detector supplied by the manufacturer [Tho05]. In order to assess the sensitivity of simulated results to assumptions regarding the HPGe dimensions, these dimensions were systematically varied after which simulations were again performed. The dimensions that were considered at were the dead layer and the core of the detector crystal. Since the element composition of the sand and soil samples used in this study was unknown, the effect of moisture was also looked at. The results from this sensitivity analysis are discussed below.

#### **5.1.2.1 Dead layer of detector crystal**

The dead layer of the detector crystal (Figure 3.16) was looked at because the ERL's HPGe detector was sent to its manufacturers for repairs in December 2003. During this time the detector was not cooled by liquid nitrogen and therefore it is believed that the dead layer may have increased due to warming. It is also important to note that on other occasions the detector was also warmed up. This increase in the dead layer is caused by a lithium contact that is used by the manufacturer. The lithium may have eaten into the active volume of the detector crystal, resulting in a larger dead layer and smaller active detector crystal [Can99]. The dead layer may have grown to twice its original size of 0.05 cm during this warming up process.

If the dead layer of the detector has increased in this manner it is expected to affect the photopeak efficiency due to an increase in the attenuation of the low-energy gamma-rays. It is also assumed that the high-energy gamma region is affected because the size of the active detector crystal would have decreased. For the purposes of this study the crystal dead layer was increased by 25 %, 50 % and 100 %, respectively, to investigate the effect that it would have on the photopeak efficiency for the standard liquid source in a 1 litre Marinelli beaker. The dimensions of the detector for the different dead layers are presented in Table 5.2.

Dimensions	Geometry			
	1	2	3	4
	(cm)	(cm)	(cm)	(cm)
		+ 25 %	+ 50 %	+ 100 %
core diameter =	0.85	0.85	0.85	0.85
core depth =	4.40	4.40	4.40	4.40
Ge crystal diameter =	6.25	6.225	6.200	6.050
Ge crystal length =	5.95	5.938	5.925	5.900
<i>dead layer =</i>	<i>0.050</i>	<i>0.063</i>	<i>0.075</i>	<i>0.100</i>
Al holder =	0.076	0.076	0.076	0.076
vacuum =	0.35	0.35	0.35	0.35
cryostat =	0.15	0.15	0.15	0.15

*Table 5.2: Detector dimensions for the different dead layers.*

Figure 5.6 shows the decrease in the absolute photopeak efficiency as the dead layer increases. It is also evident from the curves that the assumption made about the effect on the photopeak efficiency in the high-energy region of the efficiency curve is correct. The change in the dead layer causes a decrease in the active detector crystal dimensions and therefore a decrease in the photopeak efficiency.

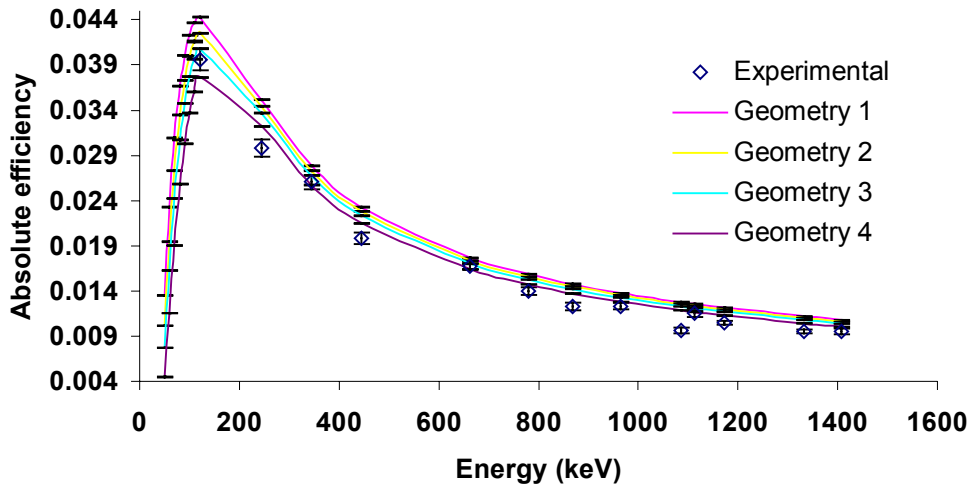


Figure 5.6: Absolute efficiency curves for 1 litre standard liquid source in Marinelli beaker showing the decrease in efficiency as the dead layer of the detector crystal increases.

Figure 5.7 is a plot of the ratio of the experimental and simulated efficiency data for the different dead layers. The decrease in the photopeak efficiency is of the order of 8 %, if the dead layer of the detector is doubled.

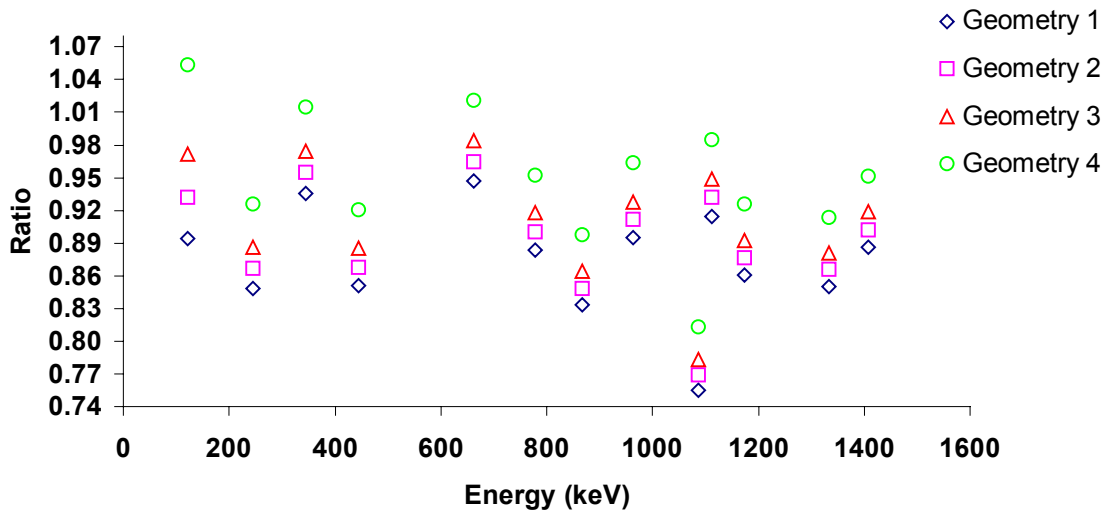


Figure 5.7: Ratio of experimental to simulated efficiency values for the different thickness of the detector crystal dead layers.



### 5.1.2.2 Core of detector crystal

The core of the detector was looked at because after a series of simulations with the MC code, GEANT, it was suggested by Gonzalez that the reason for his simulated detector being more efficient than the actual detector, was possibly because the core of the detector could have been larger than specified [Gon01]. This was investigated for this study by increasing the core of the detector crystal by 10 %. The dimensions of the detector with its increased core are given in Table 5.3.

Dimensions	Geometry	
	1	2
	(cm)	(cm)
		+ 10 %
core diameter =	0.85	0.935
core depth =	4.40	4.84
Ge crystal diameter =	6.25	6.25
Ge crystal length =	5.95	5.95
dead layer =	0.05	0.05
Al holder =	0.0760	0.0760
vacuum =	0.35	0.35
cryostat =	0.15	0.15

*Table 5.3: Dimension of detector with core increased by 10 % of its original size.*

The ERL believes that the core dimensions supplied by the manufacturer would not have an uncertainty of more than 10 % and therefore from Figure 5.8 it is evident that the core of the detector crystal does not contribute to the differences between experimental and simulated efficiency values in this study.

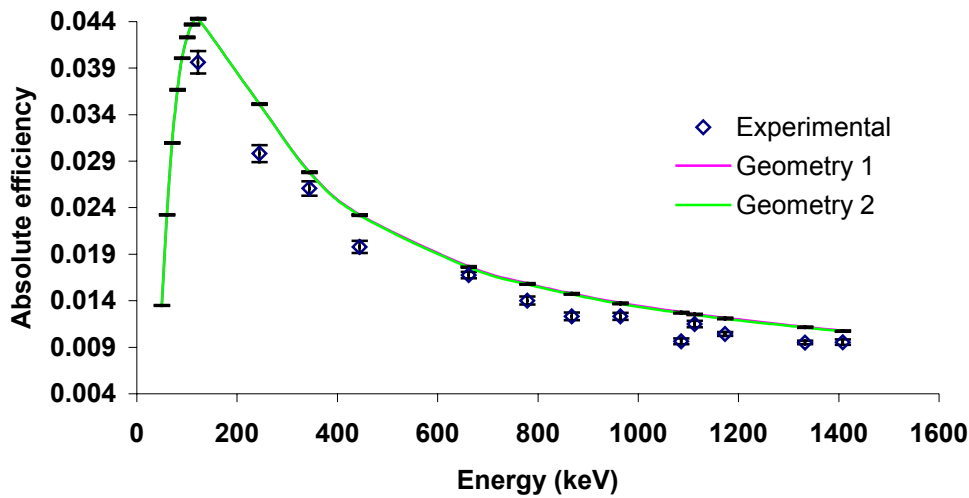


Figure 5.8: Absolute efficiency curves for 1 litre standard liquid source in Marinelli beaker for different detector core dimensions.

The calculations in the rest of this thesis uses the shape of the detector as given by the manufacturer since there is not certainty on the thickness of the actual dead layer.



## 5.2 KCl samples

### 5.2.1 Volume effect

Although much care is taken in the ERL to make sure that filling heights of samples in Marinelli beakers are reproducible, it may happen that due to human error this is not achieved and therefore the effect of volume on absolute photopeak efficiencies was investigated. A KCl sample was used because of its high purity and its emission of a single distinct gamma-ray at 1460.8 keV. Figure 5.9 shows the absolute efficiency curve for the KCl sample at different filling heights as measured (section 4.1.2) and simulated.

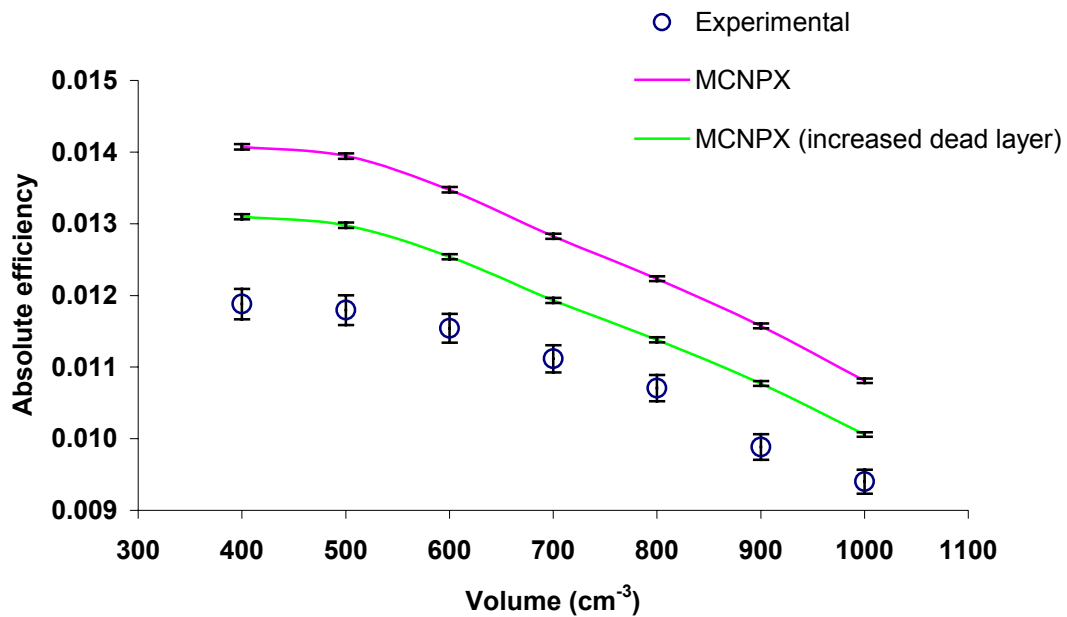


Figure 5.9: Absolute photopeak efficiency curve as a function of volume for standard KCl sample.

It is evident from Figure 5.9 that both the simulated and experimental curves follow similar trends. However it is also evident that in the region below 500 ml there is a greater deviation between the experimental and simulated curves. This serves as evidence that sufficient reproducibility of filling heights is needed in this region (below 600 ml) because of the shape of the Marinelli beaker. This region of filling heights lie around the borehole of the Marinelli beaker and if care is not taken the geometrical setup may be compromised i.e. at 500 ml the sample may not completely cover the detector.

Height	Difference	Volume	Efficiencies			
			Exp	Difference	MCNPX	Difference
cm	mm	ml		%		%
6.10		400	0.0119		0.0141	
7.62	15.2	500	0.0118	0.72	0.0139	6.65
8.29	6.7	600	0.0115	2.21	0.0135	3.50
9.11	8.2	700	0.0111	3.83	0.0128	5.08
9.75	6.4	800	0.0107	3.82	0.0122	4.84
10.42	6.7	900	0.0099	8.32	0.0116	5.67
11.28	8.6	1000	0.0094	5.14	0.0108	7.08
average	8.6			4.01		5.47
			%.mm <sup>-1</sup>		%.mm <sup>-1</sup>	
			<b>0.46</b>		<b>0.63</b>	

*Table 5.4: Absolute photopeak efficiencies for different filling heights for KCl sample.*



The percentage change in the absolute photopeak efficiency per mm was calculated by taking the ratio of the average percent difference in absolute efficiency to the average difference in filling height (Table 5.4). It was found that the change in the efficiency is approximately 0.5 % per mm experimentally and 0.6 % per mm with the use of MCNPX. These values are tabulated in Tables 5.4, and are in good agreement with those obtained by Debertin and Ren [Deb89]. It should be noted though that the value (0.5 %) obtained by Debertin and Ren was for filling heights in the range of 3 mm above and below the 1000 ml mark of the Marinelli beaker, whereas in this study an average is taken over the range 400 ml – 1000 ml (at 100 ml increments).

## 5.2.2 Density Effect

The absolute photopeak efficiency curves for the  $^{40}\text{K}$  standards (section 2.2.2) are presented in Figure 5.10, where a simple power law relationship was fitted to the experimental and simulated data. The power law is given by

$$\varepsilon_k = a \times \rho^b \quad (5.1)$$

where  $\varepsilon_k$  is the  $^{40}\text{K}$  absolute photopeak efficiency,  $\rho$  is the sample density, and the parameters  $a$  and  $b$  are given in Figure 5.10.

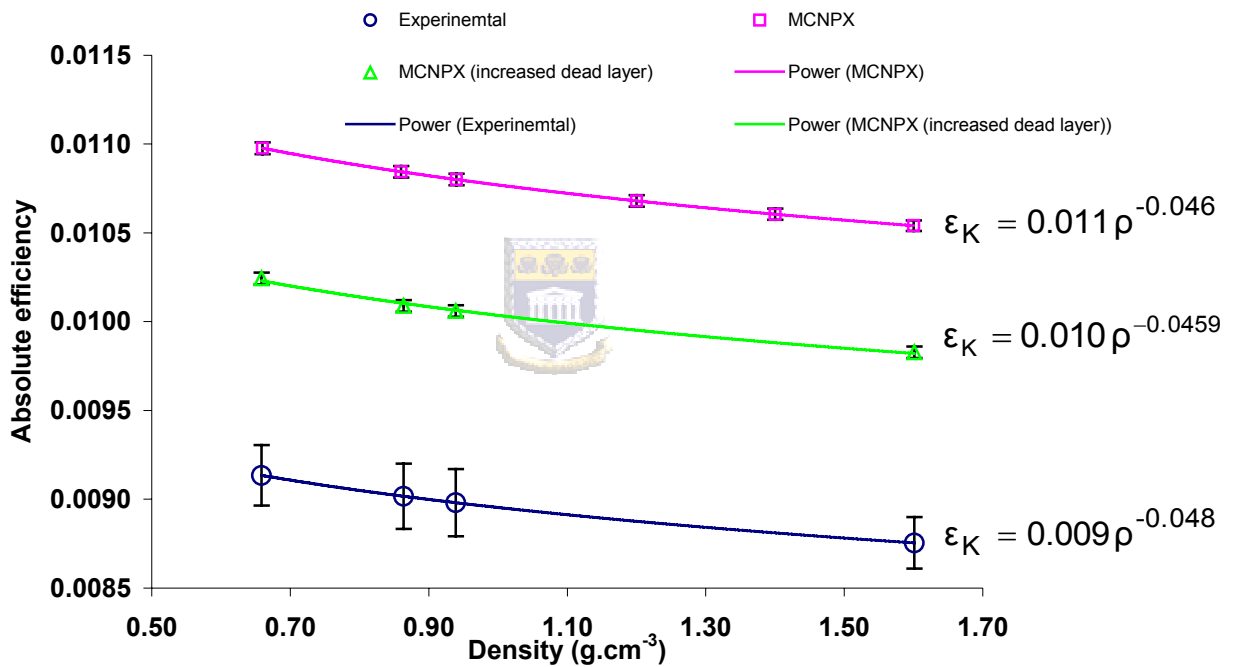


Figure 5.10: Absolute photopeak efficiency curves for  $^{40}\text{K}$  standards as a function of density.

It is clear from Figure 5.10 that the MCNPX results have the same density dependence as the experimental values, but there is an overall normalisation difference. The relative photopeak efficiency curves in Figure 5.11 were obtained by taking the ratio of the absolute photopeak efficiencies (Table 5.5) with respect to the absolute photopeak efficiency of the stearic + KCl standard (0.66 g.cm<sup>-3</sup>). The absolute photopeak efficiencies shown in Table 5.5 were calculated with the

use of equation 5.1 and the parameters  $a = 0.011$  and  $b = -0.046$  for the MCNPX simulation and  $a = 0.009$  and  $b = -0.048$  for the experimental data, from Figure 5.10.

Density	Absolute efficiency	
	Experimental	MCNPX
$\text{g.cm}^{-3}$		
0.66	$0.009133 \pm 0.0002$	$0.01098 \pm 0.00003$
0.86	$0.009018 \pm 0.0002$	$0.01085 \pm 0.00003$
0.94	$0.008980 \pm 0.0002$	$0.01080 \pm 0.00003$
1.2	$0.008875 \pm 0.0002$	$0.01068 \pm 0.00003$
1.4	$0.008810 \pm 0.0002$	$0.01061 \pm 0.00003$
1.6	$0.008754 \pm 0.0002$	$0.01054 \pm 0.00003$

Table 5.5: Absolute photopeak efficiencies calculated with equation 5.1 and the parameters  $a$  and  $b$  from Figure 5.10.

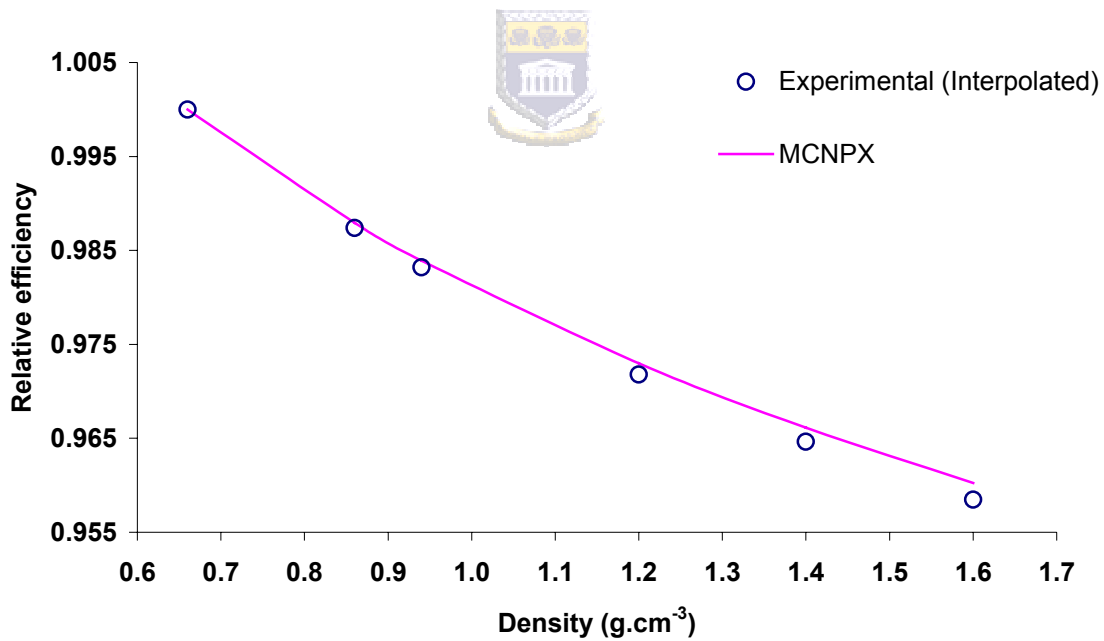


Figure 5.11: Relative efficiency curves at 1460.8 keV with respect to the efficiency value at  $0.66 \text{ g.cm}^{-3}$ .

From Figure 5.11 it is evident that the relative efficiency decreases approximately directly proportional to the KCl standard density and this is in agreement with the theory that postulates that self-attenuation of gammas increases with increasing sample density [Sim92, Deb89].

The percentage drop in efficiency was calculated with respect to the stearic + KCl standard ( $0.66 \text{ g.cm}^{-3}$ ) and plotted in Figure 5.12. For comparison, the published values of Croft [Cro99] are also included in Figure 5.12. The study of Croft and Joseph shows that the density effect in the range  $0.6 - 1.6 \text{ g.cm}^{-3}$  is less than 5 % [Cro99, Jos05] and this is in close agreement with the value achieved with MCNPX (4.2 %).

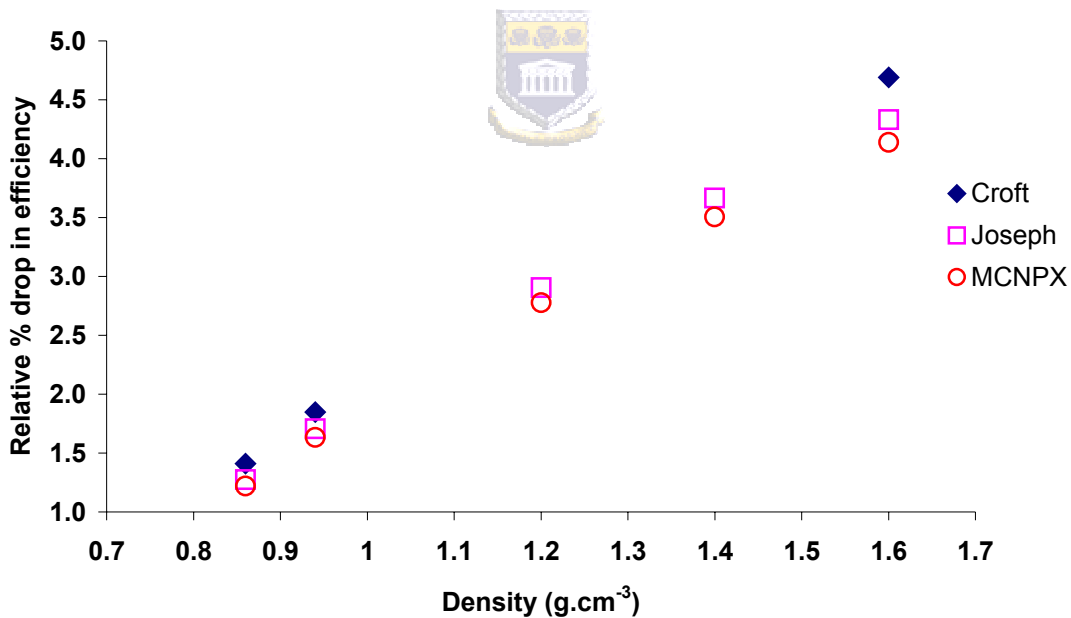


Figure 5.12: Relative percentage drops in efficiency as a function of density for the  $^{40}\text{K}$  standards.

## 5.3 Soil and Sand samples

### 5.3.1 Coincidence Summing effect

The simulated and experimental absolute efficiency curves for the vineyard soil sample of density  $1.2 \text{ g.cm}^{-3}$  in a 1 litre Marinelli beaker is shown in Figure 5.13, for the naturally occurring radionuclides uranium, thorium and potassium.

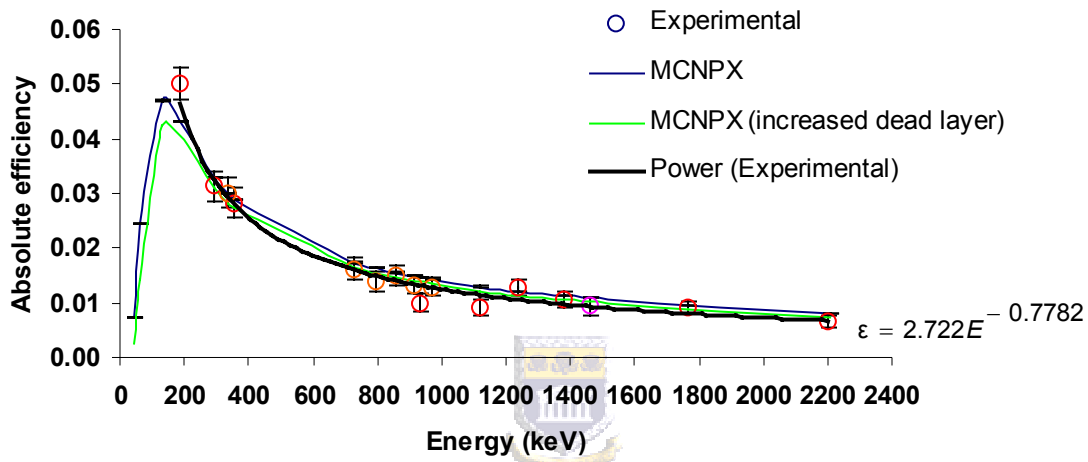


Figure 5.13: Absolute photopeak efficiency curves showing the turnover region. The data points are associated with the decay of  $^{238}\text{U}$ ,  $^{232}\text{Th}$  and  $^{40}\text{K}$ . The green curve shows the absolute efficiency when the detector crystal dead layer is increased to twice its original size. An interpolated absolute efficiency curve showing its parameters  $a = 2.722$  and  $b = -0.7782$  is also shown.

A similar study to that done with the standard liquid source (section 5.1) was undertaken for a soil sample, to determine the effect that coincidence summing may have on the absolute photopeak efficiency for the gamma lines (186.1 keV, 351.9 keV, 727.3 keV, 911.2 keV, 968.0 keV and 1120.3 keV) used by the ERL to determine the activity concentration of soil and sand samples.



In this investigation the ratio of the absolute photopeak efficiency with respect to the 1460.8 keV absolute photopeak efficiency value (from the decay series of  $^{40}\text{K}$ ) was plotted to obtain the relative photopeak efficiency curve (Figure 5.14). The 1460.8 keV gamma line was chosen because it is the only gamma emission from the  $^{40}\text{K}$  decay series and therefore not prone to coincidence summing.

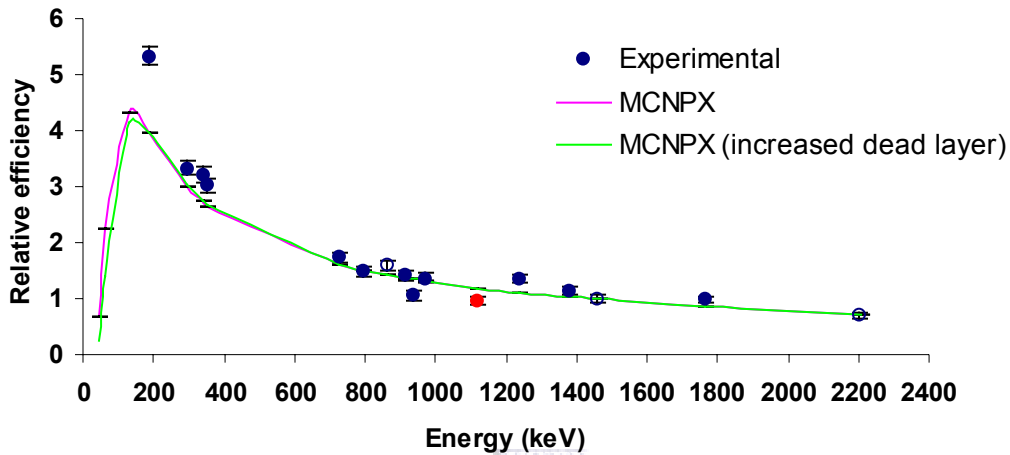


Figure 5.14: Relative photopeak efficiency curve with respect to the 1460.8 keV efficiency value. The green curve shows the absolute efficiency when the dead layer of the detector crystal is increased to twice its original size. The filled circles show those lines used by the ERL to determine activity concentrations in soil and sand samples, which are prone to coincidence summing.

The filled circles represent those lines used by the ERL to determine activity concentrations in soil and sand samples, which are prone to coincidence summing. The blue circles show the lines that sum to give sharp peaks by summing out (Figure 5.14), whereas the red circles show lines that are prone to summing in (i.e. summing that contribute to a photopeak).

For environmental studies, the lines in the naturally occurring radionuclides uranium, thorium and actinium series that are prone to coincidence summing, need to be considered [Tor05]. In the uranium series the most intense gamma emissions in the spectra are from the radionuclides  $^{214}\text{Pb}$  and  $^{214}\text{Bi}$ . For  $^{214}\text{Pb}$  the principal gamma line is 351.9 keV, and is not expected to need much correction

for coincidence summing [Gar01]. Therefore this line is used by the ERL in the determination of activity concentrations for soil and sand samples. However the other intense gamma line of 242.0 keV found in the experimental spectra, which is affected by coincidence summing is not used by the ERL. For  $^{214}\text{Bi}$  the most probable gamma emissions occur from the 609.3 keV and 1120.3 keV gamma lines. Both these gamma lines suffer summing out, because they are emitted in cascade with other photons. Therefore the 609.3 keV gamma line is not used by the ERL for activity concentration determination. The 1120.3 keV line was used because it was not expected to need much correction for coincidence summing [Gar01], however this line is now no longer used since the findings of Joseph [Jos05].

In the thorium decay series the most intense emissions are from the radionuclide  $^{228}\text{Ac}$ . The gamma lines associated with  $^{228}\text{Ac}$  are 911.2 keV and 969.0 keV, which may suffer coincidence summing due to cascades with photons from other energy levels. Another significant gamma emission in the thorium series is the 727.3 keV gamma line from the  $^{214}\text{Bi}$  radionuclide, which also shows some coincidence summing [Gar01]. Although other gamma emissions do occur in the thorium series, only these lines have been mentioned because they are used by the ERL to determine activity concentrations.

Another line that is of concern to the ERL is that of the 186.1 keV gamma-ray, which occurs from the  $^{226}\text{Ra}$  radionuclide in the actinium decay series. This peak appears as a doublet with the gamma line of the  $^{235}\text{U}$  occurring at 185.7 keV. At present the software used by the ERL is not able to distinguish between these two gamma lines.

Evidence for coincidence summing can be found in the experimental spectrum of the soil sample as shown in Figure 5.15.

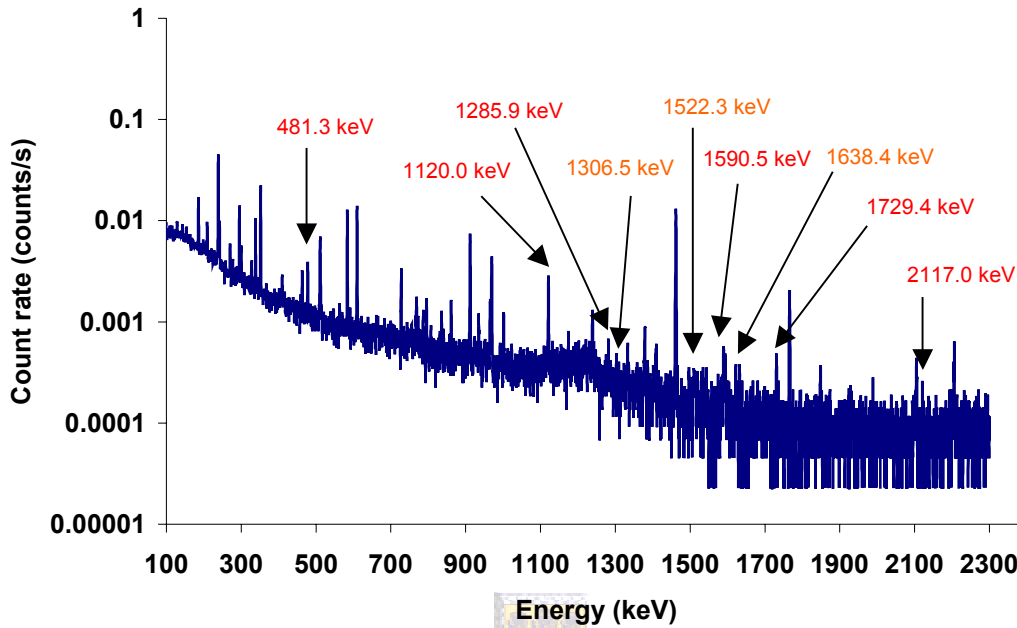


Figure 5.15: Peaks in soil sample spectrum that show evidence of coincidence summing in the  $^{238}\text{U}$  and  $^{232}\text{Th}$  decay series.

The combinations of gamma lines in the uranium and thorium series that make up the peaks shown in Figure 5.15 are given in Tables 5.6 and 5.7.

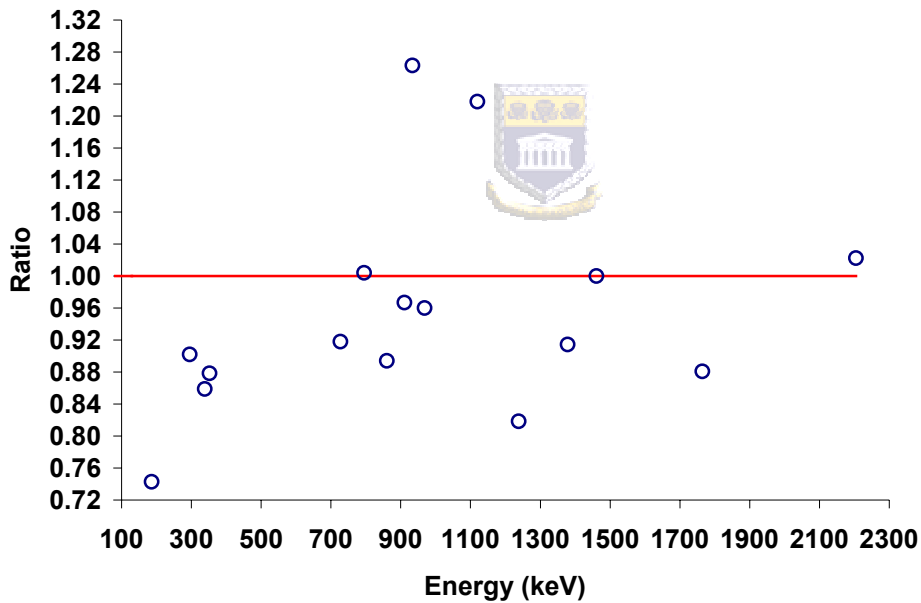
<b>KeV</b>	<b>295.2</b>	<b>352</b>	<b>933.9</b>	<b>1120.4</b>
<b>186.1</b>	481.3		1120.0	1306.5
<b>352</b>			1285.9	
<b>1238.5</b>		1590.5		
<b>1377.4</b>		1729.4		
<b>1765</b>		2117.0		

Table 5.6: Combinations of gamma-rays (keV) that undergo coincidence summing in the  $^{238}\text{U}$  series. The shaded grey boxes indicate those peaks that undergo summing in.

<b>keV</b>	<b>795</b>	<b>911.1</b>	<b>968.1</b>
<b>338.4</b>			<b>1306.5</b>
<b>727.3</b>	<b>1522.3</b>	<b>1638.4</b>	

*Table 5.7: Combinations of gamma-rays (keV) that undergo coincidence summing in the <sup>232</sup>Th series.*

In order to determine what effect coincidence summing may have on the absolute photopeak efficiency of the gamma lines used by the ERL to determine activity concentrations in soil and sand samples, the ratio of the relative photopeak efficiencies of experimental and simulated data are plotted in Figure 5.16.



*Figure 5.16: Ratio of simulated to experimental relative photopeak efficiency values.*

It is evident in Figure 5.16 that there is a deviation of up to 14 % between most of the simulated and experimental values. Although there is evidence from the experimental spectrum that the 351.9 keV gamma line is prone to coincidence summing, the difference between experimental and simulated values is 12 %.

The work of Laborie showed deviations of less than 10 % between experimental and simulated data to be acceptable, for low-energy gamma-ray spectrometry when calculating a photopeak efficiency calibration curve and coincidence summing corrections in volume sources. This would suggest that if a 2 % coincidence summing effect is considered for the 351.9 keV gamma line as suggested by the findings of Garcia-Talavera [Gar01], the difference between experimental and simulated values would be within 10 %. Therefore no significant correction has to be made for the 351.9 keV, 1377.4 keV and 1765.0 keV gamma lines. The 1120.3 keV gamma line suffers from coincidence summing out effects, since it is emitted in cascade with a large number of photons [Gar01]. The work of Joseph has shown that by omitting the 1120.3 keV gamma line when determining uranium activity concentrations in soil sample, the risk of underestimating the uranium activity concentration by up to 15 % is removed. Therefore this gamma line is no longer used by the ERL for uranium activity concentration determination.



In the case of the gamma lines of the thorium series, the effect of coincidence summing for the 911.1 keV and 968.1 keV was found to be in the order of 5 % and 7 %, respectively [Gar01, Jos05]. The difference in the simulated and experimental values shown in Figure 5.16, show a difference of 3 % and 4 %, respectively and are therefore in good agreement with the findings of Garcia-Talavera and Joseph. It is therefore essential to introduce correction factors for the gamma lines from the thorium series to obtain accurate absolute photopeak efficiencies for activity concentration determination.

It should however be noted that although the simulated absolute photopeak efficiency curves mainly lie within the uncertainties of the experimental data in this case, there may be discrepancies due to the fact that there is a systematic problem in the simulations, since it may miss some important information on the precise details of the detector (section 5.1.2) and more especially, the composition of the soil sample.

### 5.3.2 Volume effect

A source of error in efficiency measurements that is usually neglected is the effect of insufficient reproducibility of filling height when using Marinelli beakers [Cro99]. Although Marinelli beakers of similar dimensions are available, variations in the filling heights may introduce errors of a few percent. Reproducing filling heights is only a matter of care but it is important to check the effect that this may have on determining absolute photopeak efficiency values. Another important reason for this study is the fact that in the ERL, we sometimes have limited sample material, which results in us not being able to fill the Marinelli beaker to the 1 litre mark and it is therefore essential to understand what effect this may have on determining accurate photopeak efficiencies.

In order to investigate the effect of volume (filling height) on the photopeak efficiency, the  $^{40}\text{K}$  gamma-ray (1460.8 keV) was looked at in a beach sand sample in Marinelli beakers filled in 100 ml increments from 400ml up to and including 1000 ml. This gamma – ray was chosen in order to avoid the effect of coincidence summing. From the relative efficiency curves of Figure 5.17, it can be seen that the relative photopeak efficiency curves do not follow similar trends as in the case of the KCl sample (section 5.2.1).

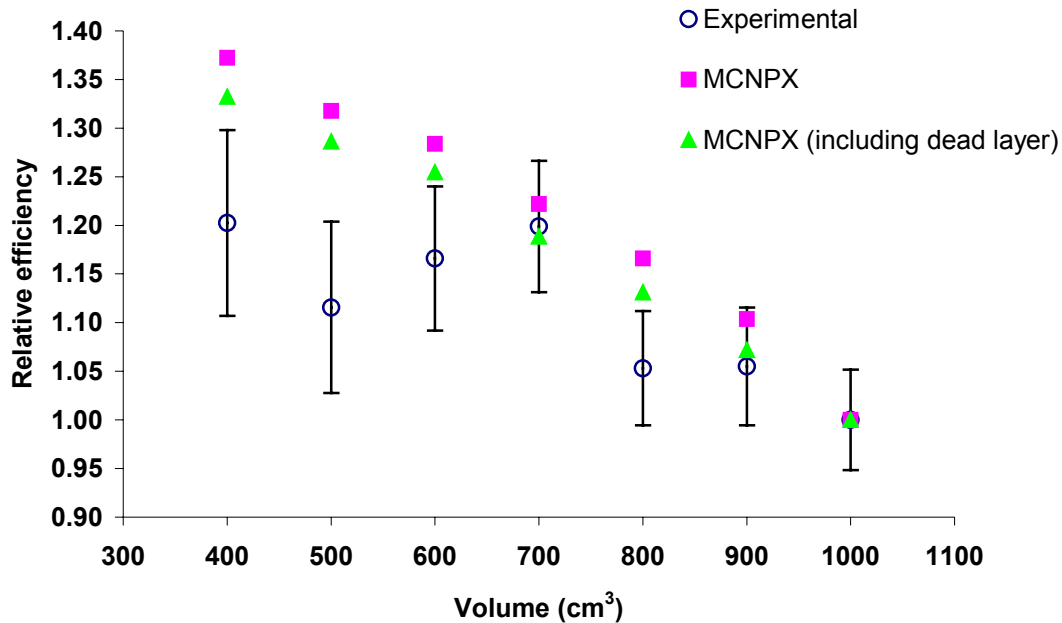


Figure 5.17: Relative photopeak efficiency curve at 1460.8 keV as a function of volume for beach sand sample.

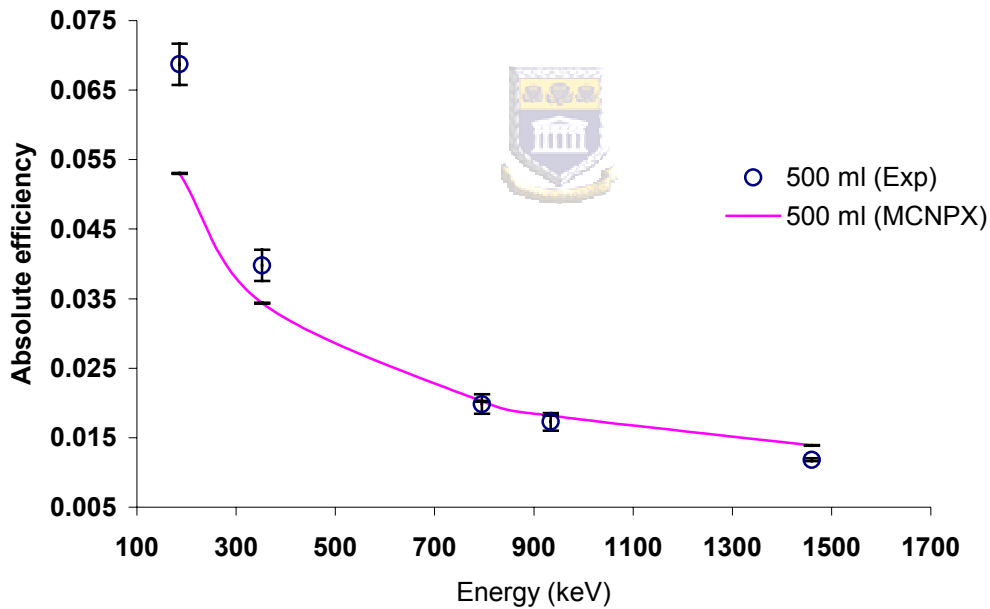
The discrepancy in the trends of the curves in Figure 5.17, could be a result of homogeneity. Although the sample was mixed before being transferred to the Marinelli beakers, only one sand sample was used in this study. It is therefore suggested that other sand samples be obtained and measured for a longer period of time (up to 24 hours), to verify if the homogeneity of the sample was indeed the cause of the discrepancy.

It has already be mentioned that the ERL sometimes does not have sufficient sample material to fill a Marinelli beaker and it is therefore important to establish an idea of the effect of volume on absolute photopeak efficiencies, which are needed to determine accurate activity concentrations. With this in mind the natural gamma energies shown in Table 5.8 were simulated to determine the effect of volume on absolute photopeak efficiency at different filling heights.

Energy keV	Volume (ml)					
	500	600	700	800	900	1000
	$\epsilon$	$\epsilon$	$\epsilon$	$\epsilon$	$\epsilon$	$\epsilon$
186	$0.0530 \pm 0.00006$	$0.0521 \pm 0.00007$	$0.0493 \pm 0.00007$	$0.0465 \pm 0.00007$	$0.0436 \pm 0.00007$	$0.0401 \pm 0.00006$
352	$0.0344 \pm 0.00006$	$0.0337 \pm 0.00006$	$0.0319 \pm 0.00006$	$0.0302 \pm 0.00006$	$0.0284 \pm 0.00005$	$0.0262 \pm 0.00005$
795	$0.0203 \pm 0.00004$	$0.0198 \pm 0.00004$	$0.0188 \pm 0.00004$	$0.0179 \pm 0.00004$	$0.0169 \pm 0.00004$	$0.0156 \pm 0.00004$
934	$0.0182 \pm 0.00004$	$0.0178 \pm 0.00004$	$0.0169 \pm 0.00004$	$0.0161 \pm 0.00004$	$0.0151 \pm 0.00004$	$0.0141 \pm 0.00004$
1460	$0.0139 \pm 0.00004$	$0.0135 \pm 0.00004$	$0.0129 \pm 0.00004$	$0.0123 \pm 0.00003$	$0.0116 \pm 0.00003$	$0.0105 \pm 0.00003$

*Table 5.8: The natural gamma – ray energies simulated at different volumes for the beach sand sample.*

Figures 5.18 – 5.20 show the absolute photopeak efficiency curves for three (3) of the different volumes, 500 ml, 800 ml and 1000 ml, respectively.



*Figure 5.18: Absolute photopeak efficiency curves for 500 ml beach sand sample in Marinelli beaker.*



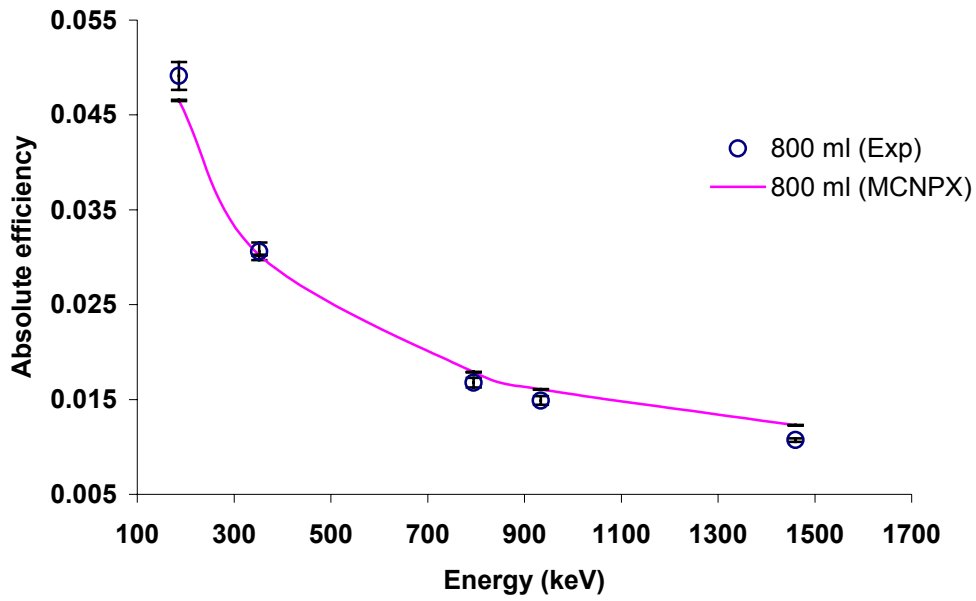


Figure 5.19: Absolute photopeak efficiency curves for 800 ml beach sand sample in Marinelli beaker.

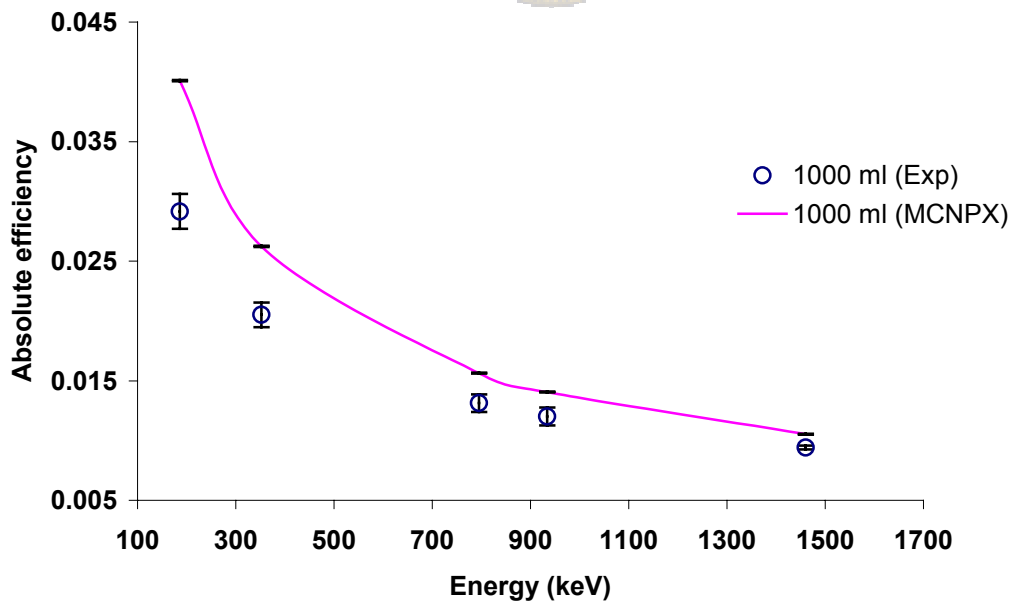


Figure 5.20: Absolute photopeak efficiency curves for 1000 ml beach sand sample in Marinelli beaker.

It is evident from these figures that the low energy gamma-rays are affected (< 500 keV) the most by filling height. This is a result of self-attenuation in the sample [Sim92, Jos05].

### 5.3.3 Sensitivity analysis

#### 5.3.3.1 Moisture in volume source

Although the soil and sand samples used in this study were dried, a check was done to determine whether there may still have been moisture in the soil and sand samples and if there was, how would this effect the photopeak efficiency. Moisture content of 15 % was assumed to be present in the 1 litre soil and sand sample in a Marinelli beaker. It is believed that if there were moisture in the samples when measured with the HPGe it would not have exceeded this amount.

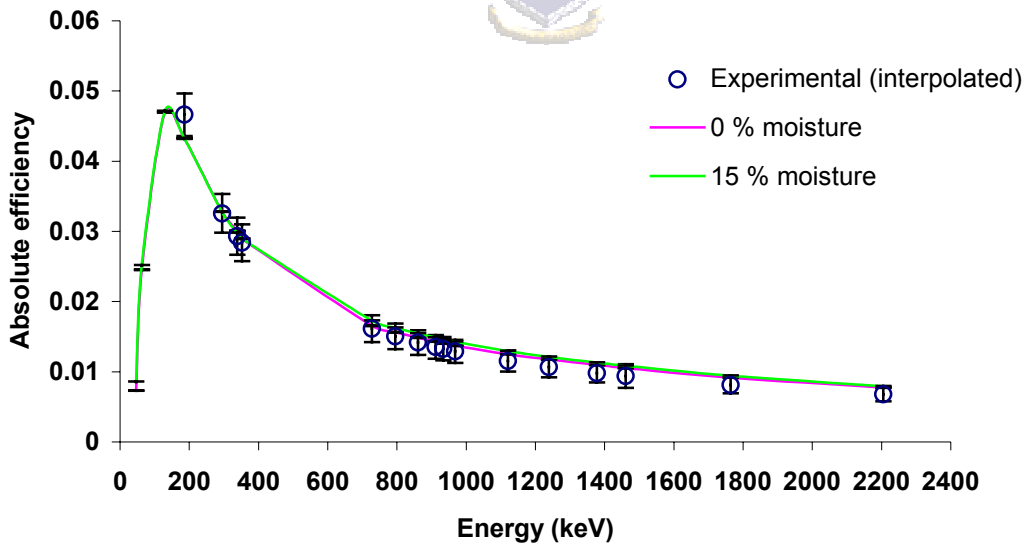
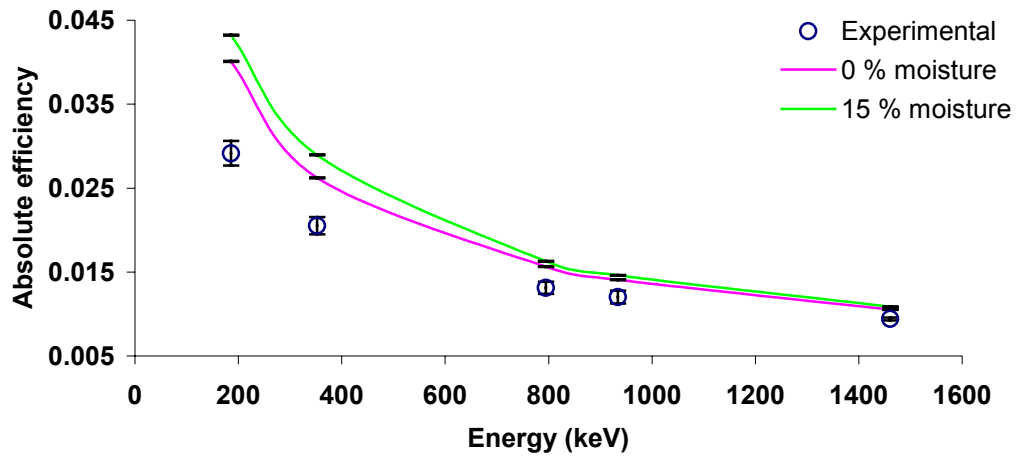


Figure 5.21: Absolute efficiency curves for soil sample when there is 15 % moisture in the volume sample.



*Figure 5.22: Absolute efficiency curves for sand sample when there is 15 % moisture in the volume sample.*

It can be deduced from Figures 5.21 and 5.22 that moisture does not make a large difference in the simulated results and therefore does not explain why the simulated results are larger than the experimental results.



#### **5.4. Z effect**

When the chemical composition or density of a sample is changed, the attenuation of photons within the source, also called “self-attenuation”, will be different [Sim92]. In light of the fact that a chemical analysis of the beach sand and soil sample used in this work was not done; the actual element composition of the soil was unknown. It was decided that a theoretical investigation should be undertaken to check whether these differences in attenuation within the source are significant in view of the desired measuring accuracy. The results of this investigation will be presented here.

In order to get an idea of the effect of the composition on the absolute photopeak efficiency, two different situations were looked at. In the first case the Al in the composition of generic soil 1 (Table 3.7) was changed to Pb and the density ( $\rho = 1.63 \text{ gm.cm}^{-3}$ ) of the sample kept the same. This was done in order to avoid any density effects (section 5.2.2). In the second case the absolute efficiency curve for generic soil 2 (Table 3.8) was simulated and compared to the absolute efficiency curves of the first case (generic soil 1 with Al and Pb). Once again the density of the soils were kept the same to avoid any density effects.

Figures 5.23 – 5.25 show the absolute efficiency curves for the different soil compositions.

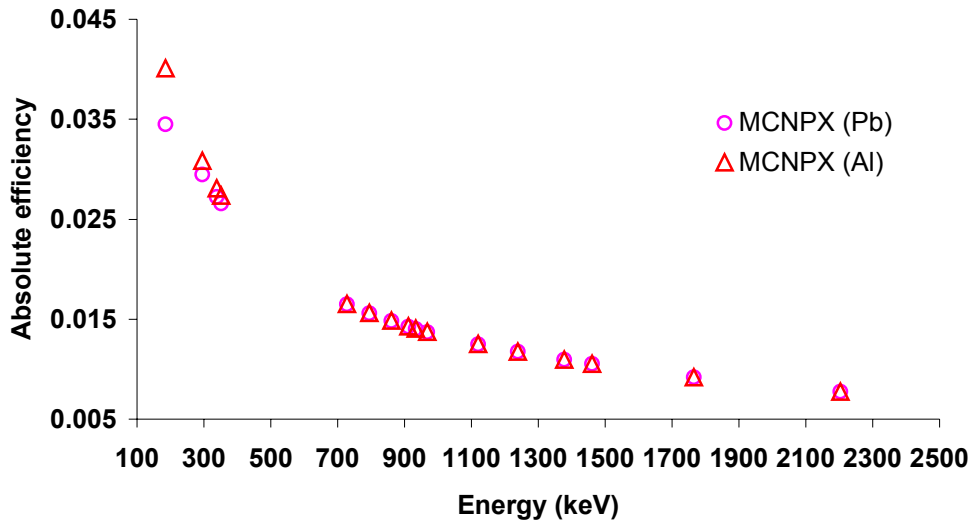


Figure 5.23: Absolute efficiency curves for generic soil sample 1 and when there is a change of one element (Al to Pb) in its composition.

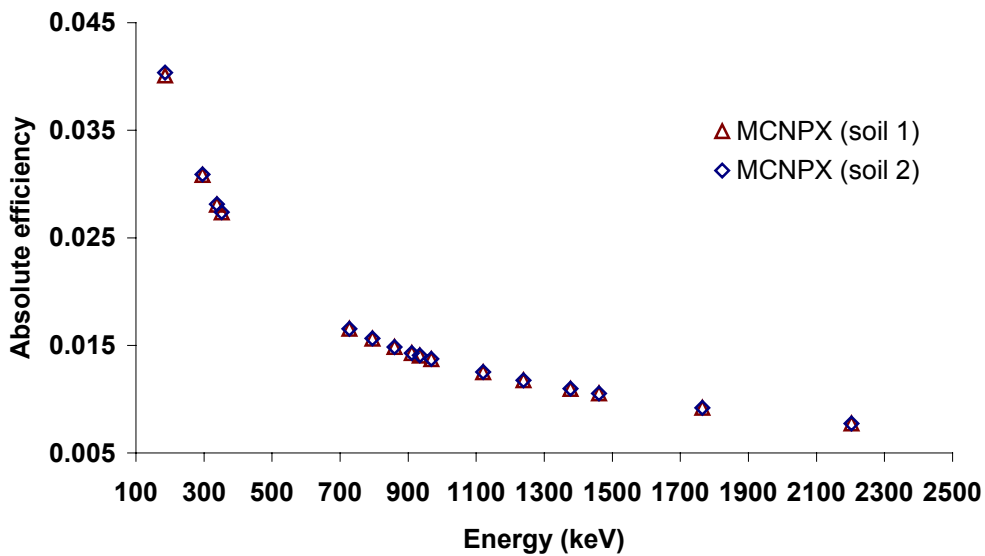
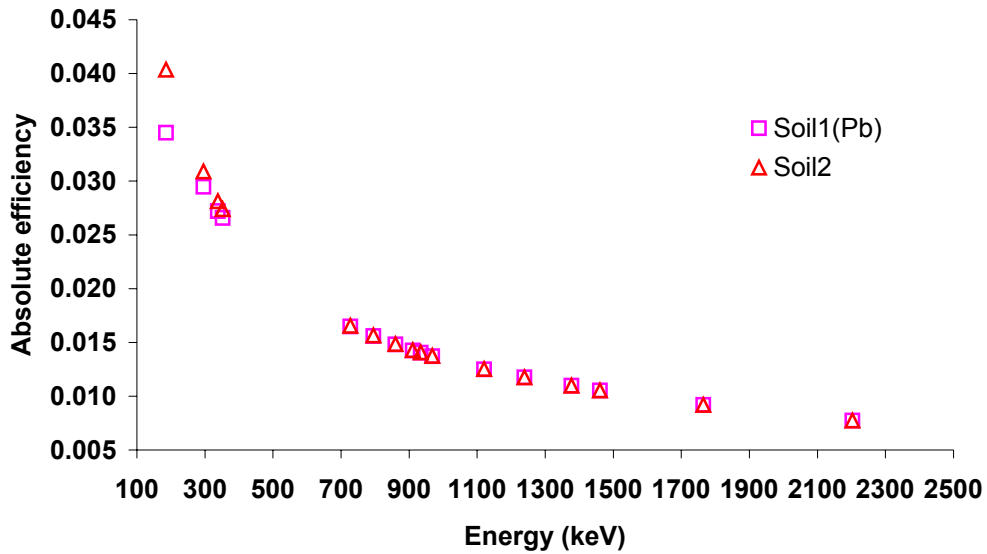


Figure 5.24: Absolute efficiency curves for generic soil samples 1 and 2. Their element compositions are given in Tables 3.7 and 3.8.



*Figure 5.25: Absolute efficiency curves for generic soil sample 1, where Al is changed to Pb, and generic soil sample 2.*



It is evident from the absolute photopeak efficiency curves in Figures 5.23 – 5.25, that the soil samples are prone to self-attenuation in the energy region below 400 keV. In this energy region (< 400 keV) photoelectric absorption, which is strongly dependent on the atomic number  $Z$  of the absorbing material, predominates (Figure 1.8).

The effective atomic number  $Z_{\text{eff}}$  is characteristic of a compound or mixture of elements and in the energy range 0.1 MeV – 3.0 MeV, is approximated by the expression

$$Z_{\text{eff}} = m \sqrt{\frac{\sum w_i \frac{Z_i}{A_i} Z_i^m}{\sum w_i \frac{Z_i}{A_i}}} \quad (5.2)$$

where  $m = 3.2$  and  $Z_i$  represents the atomic number of element  $i$  and  $A_i$  represents the average atomic mass element  $i$  [Jos05]. The effective atom numbers for the generic soils used in this study and that of KCl are presented in Table 5.9.

Sample	$Z_{\text{eff}}$	density g.cm <sup>-3</sup>
Soil 1 (Al)	10.1	1.63
Soil 1 (Pb)	25.7	1.63
Soil 2	13.2	1.63
KCl	18.1	1.21

*Table 5.9: The effective atomic numbers calculated from equation 5.2 for the generic soils and KCl used in this study.*

The ratio of the efficiency values for each of the curves in Figures 5.23 – 5.25 are plotted in Figure 5.26.

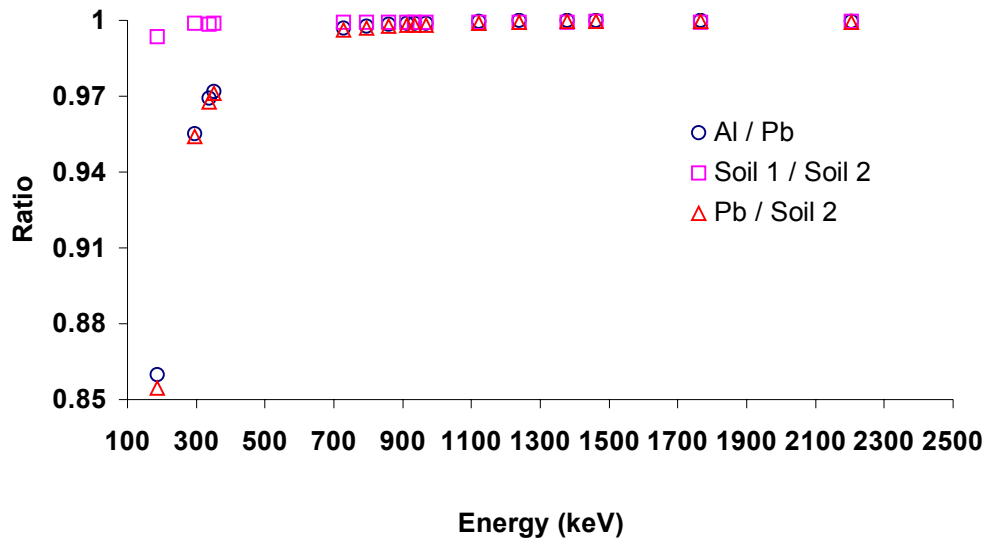


Figure 5.26: Ratio of the efficiency values of the absolute photopeak efficiency curves for the different generic soil compositions.



From Figure 5.26 it is evident that gamma-rays of energies below 400 keV are prone to self-attenuation; this is in agreement with Figure 3.9, which shows that high-energy gammas have a larger possibility of passing through the material than low-energy gammas [Sán91]. This figure also stands as evidence that self-attenuation of gamma-rays in soil samples decreases as the gamma energy increases and is in agreement with the energy dependence of the linear absorption coefficients (Figure 3.10).



## Chapter 6

### Summary and Outlook

The work presented in this dissertation is based on the investigation into the possibility of determining an understanding, through computational means, of the effect of various parameters on the absolute photopeak efficiency for the HPGe detector in the ERL at iThemba LABS. This is of importance in obtaining accurate laboratory activity concentration measurements using the HPGe detector in the ERL. The findings of this study are first summarised, thereafter further possible work is outlined.

#### 6.1 Summary

A test case study was done, where the results from the MCNPX code and a DeV – C++ program (developed for this study) were compared. The geometry that was simulated, was that of a Ge sphere with a point source of gamma-rays at its centre. The results for the deposition of energy in the sphere, showed deviation between the codes of up to 30 %. The deviations between the results can probably be attributed to the assumptions made in the C++ program (section 3.2.3.1). For energies below 400 keV photoelectric absorption predominates (Figure 1.8) and the strong Z dependence of this interaction would explain the difference of less than 10 % between C++ and MCNPX. However for energies above 400 keV, Compton scattering begins to dominate (Figure 1.8) and therefore the large differences shown in Figure 3.14 are due to the fact that the photons in the C++ program are assumed to scatter isotropically, whereas in MCNPX the Klein-Nishina formula is used which predominately causes forward scattering (section 3.1.3). This forward scattering would cause more photons to likely escape the sphere after undergoing Compton scattering, whereas the random scattering in the C++ simulations is more likely to cause the photon to

scatter back into the sphere. This results in a greater probability that the photon will undergo a further interaction and deposit all of its energy in the sphere and therefore contributing to higher photopeak efficiency.

The MCNPX code was used to simulate the photopeak detection efficiency of a HPGe detector (45 % relative efficiency) used in conjunction with volume sources of gamma-rays. The samples were water (spiked with the radionuclides  $^{152}\text{Eu}$ ,  $^{60}\text{Co}$  and  $^{137}\text{Cs}$ ), soil, sand and KCl. Gamma-ray lines associated with the decay of the  $^{238}\text{U}$ ,  $^{232}\text{Th}$  and  $^{40}\text{K}$  series, were considered in the simulation of soil, sand and KCl samples. KCl is of interest since it is used to set the relative photopeak efficiency curve on an absolute scale at 1460.8 keV. For the liquid source the average deviations between the absolute experimental and simulated efficiencies were found to be 12 %. The data were normalised to the 662 keV ( $^{137}\text{Cs}$ ) value in order to look for evidence of coincidence summing. There are indications that the lines, 121.8 keV, 244.7 keV, 444.1 keV and 1085.8 keV of the  $^{152}\text{Eu}$  series are particularly prone to summing. This is in agreement with the finding of Gilmore [Gil95]. For the 1173.2 keV and 1332.5 keV gamma lines of the  $^{60}\text{Co}$  series, Figure 5.5 shows a difference of 9 % and 11 %, respectively, between simulated and experimental results. This is in good agreement with the findings of Garcia-Torano [Tor05], who found that the correction factor for these gamma energies is of the order of 10 % (see discussion in Appendix D).

A sensitivity analysis of the simulated results (section 5.1.2) was conducted for the liquid source and it was found that the simulated results were most sensitive to the detector dead layer. It was found that if the dead layer of the detector was doubled from its original size of 0.05 cm, this resulted in an average decrease in the detection efficiency by 8 %.

For the soil sample the deviation between simulated and experimental data for most efficiencies was found to be less than 14 %. This study has shown that for  $^{238}\text{U}$  decay series, no significant coincidence correction factors are needed. For

the 186.1 keV and 933.9 keV gamma lines, which show differences of greater than 14 % between simulated and experimental values, the discrepancies can largely be attributed to some systematic error in the simulations. This is still to be investigated. The findings of Joseph, show that when the 1120.3 keV gamma line is omitted from determining the activity concentration of uranium in soil samples, the risk of underestimating the uranium activity concentration by up to 14 % is removed. The large difference shown in Figure 5.16 for this gamma line confirms the need to remove this photopeak when determining the activity concentration of uranium in soil samples.

The effect of coincidence summing on the 911.1 keV and 968.1 keV, from the thorium decay series, was found to be 3 % and 4 %, respectively. This is in good agreement with the work of Garcia-Talavera, who found the effect of coincidence summing for the 911.1 keV and 968.1 keV to be in the order of 5 % and 7 %, respectively [Gar01]. This study has therefore shown the need for coincidence summing correction factors for the gamma lines of the  $^{232}\text{Th}$  series.



The effect of filling height, when dealing with a close geometry setup like that of the Marinelli beaker, is sensitive to changes at the mm level. Experimentally it has been determined that the approximate filling height variation of efficiency for the  $1.29 \text{ g.cm}^{-3}$  KCl sample in a Marinelli beaker is about 0.5 % per mm [Jos05, Deb89] and in this study the variation when simulated was found to be 0.6 % per mm. This figure is not expected to vary appreciably with photon energy and therefore the estimated uncertainty of the sample activity measurement due to the effect of filling heights is estimated in this range of 0.6 % per mm. However it is important to note that for filling heights below 600 ml care should be taking to sufficiently reproduce filling heights because this region of filling lies around the borehole of the Marinelli beaker. If care is not taken the geometrical setup may be comprised i.e. at 500 ml the sample may not completely cover the detector crystal and the effect of self-attenuation on the low-energy gamma rays causes a

decrease in the photopeak efficiency. Evidence for this is found in Figure 4.7 and Figures 5.18 – 5.20.

For the beach sand sample it was found that there is a large discrepancy between the trends of the simulated and experimental relative efficiency curves. The discrepancy in Figure 5.17, could be a result of homogeneity. Although the sample was mixed before being transferred to the Marinelli beakers, it should be noted that only one sand sample was used in this study. It is therefore suggested that other sand samples be obtained and measured for a longer period of time (up to 24 hours), to verify if the homogeneity of the sample was indeed the cause of the discrepancy.

The MCNPX results for the effect of density on photopeak efficiency, in the density range  $0.6 \text{ g.cm}^{-3} - 1.6 \text{ g.cm}^{-3}$ , show the same density dependence as the experimental values, but there is an overall normalisation difference (Figure 5.10). Figure 5.11 shows that the relative efficiency (for both interpolated experimental and simulated) decreases approximately directly proportional to the densities of the KCl standards and this is in agreement with the theory that postulates that self-attenuation of gammas increases with increasing sample density [Sim92, Deb89].

The percentage drop in efficiency in the density range  $0.6 - 1.6 \text{ g.cm}^{-3}$ , which covers the region of interest for the densities of the environmental sand and soil samples that are analysed in the ERL, was calculated with respect to the stearic + KCl standard ( $0.66 \text{ g.cm}^{-3}$ ). For the MCNPX simulations, the percentage drop in photopeak efficiency at 1460.8 keV was found to be 4.2 % and is in good agreement with the value of less than 5 % that was obtained in the work of Joseph and Croft [Jos05,Cro99].

The effect of atomic number,  $Z_{\text{eff}}$ , (i.e. the chemical composition) for the generic soil samples simulated in this study has been found to be negligible for energies

above 400 keV (Figure 5.26). This study has shown that knowledge of the element composition of a sample is important when simulating the photopeak detection efficiency of a detector in a close geometry setup. If the composition of the heavy elements is not properly considered when simulating soil and sand samples, the effect of atomic number on the absolute photopeak efficiency in the low energy (< 400 keV) areas is of the order of approximately 14 % (Figure 5.26). This is due to the strong dependence of photoelectric absorption, in the low-energy range (< 400 keV), on  $Z$ . This is important in explaining the discrepancies found in the simulations for the lower energies described in this work.

## **6.2 Outlook**

To improve the results of the intercomparison exercise undertaken in this study, improvements will have to be made to the assumptions formulated in the C++ code. This would involve the addition of the Klein-Nishina formula for the C++ code and therefore to extend the code to a cylindrical geometry.

This study has demonstrated that MC simulations provide a useful means of studying the systematic effects (associated with sample and detector properties) that impinge on the photopeak detection efficiency. The results for the liquid source will enable coincidence summing corrections to be made for selected lines. The accuracy of measured activity concentrations for liquid samples will therefore be improved. Further improvements to the photopeak detection efficiency for liquid sources can be obtained by implementing calculation similar to the efficiency transfer method of Jurado Vargas [Var03] (see Appendix E for discussion).

One source of uncertainty when simulating soil and sand samples is the chemical composition of the soil/sand. Obtaining a soil/sand sample that has been analysed by a certified laboratory can eliminate this uncertainty. The result for the

soil sample will enable coincidence summing corrections to be made for selected lines and therefore improve the accuracy of measured activity concentrations for soil/sand samples. These coincidence summing corrections would then have to be validated with methods, such as Full Spectrum Analysis [Hen01, Map05], which is already under investigation in the ERL. This method requires no coincidence summing corrections.



## Appendices

### Appendix A

#### MCNPX input file for intercomparison exercise

The input file presented here is for a 661.8 keV point source at the centre of a germanium ( $\rho = 5.323 \text{ g.cm}^{-3}$ ) sphere with a radius of 1 cm.

662 keV Point Source in sphere

```
c
c
c -- cell cards
c *****
c *****Sphere*****
c *****
c Germanium sphere
  1 1 -5.323 -1          imp:p=1
c whole universe
  999 0 1              imp:p=0
c *****
c -- Surface cards
  1 so 1 $ Ge sphere

c -- Data cards
mode p
c
sdef pos=0 0 0 erg=0.6618 par=2
si1 1
c
f8:p 1
e0 0 0.001 663i 0.665
c
m1 32000. 1
c
nps 10000000
ctme 60
print
```




## Appendix B

### MCNPX input files for Marinelli geometry

The schematic of the Marinelli geometry in Figure 3.16 shows the surfaces (cm), which are defined in the MCNPX input files shown here as **surface cards**. These surfaces are combined to forms cells (Table 3.5 and 3.6), which describe the geometry (**cell cards**) through which the radiation (**photons**) in transported. The source, type of estimator (i.e. calculation to be carried out) and the materials of the different components of the geometry are defined in the **data cards**. It should be noted that there is a difference in the definition of the sample in the **cell cards** in the case of the 1 litre and the 0.4 litre Marinelli setup, this is because the 0.4 litre sample lies below the bore hole of the Marinelli beaker.

Germanium detector and 1.0 liter Marinelli beaker setup (soil sample)



```
c
c
c -- cell cards
c *****
c *****Detector*****
c *****
c Germanium crystal
1 1 -5.323 (33:-18:34) -1 18 -3          imp:p=1
c Core cavity
14 0 -33 18 -34 imp:p=1
c Dead layer
3 1 -5.323 (1:-18:3) -4 19 -6          imp:p=1
c Al holder
4 6 -2.700 (4:-19:6) -7 -6 19          imp:p=1
c Vacuum space
5 0 (7:-19:6) -10 -2 5          imp:p=1
```



c Al cryostat

13 6 -2.700 (10:2:-5) -30 -31 32 imp:p=1

c \*\*\*\*\*

c \*\*\*\*\*Marinelli Beaker\*\*\*\*\*

c \*\*\*\*\*

c Air between detector and beaker

2 5 -1.20484e-3 (30:31) 32 -16 -15 imp:p=1

c Marinelli beaker

6 3 -1.65 (16:15) -17 20 -21 imp:p=1

7 3 -1.65 (22:-18) 17 -23 20 -25 imp:p=1

8 3 -1.65 -23 25 -26 imp:p=1

c Sample and air inside

9 4 -1.63 (17:21) 18 -22 -24 imp:p=1

10 5 -1.20484e-3 -22 24 -25 imp:p=1

c Air outside

11 5 -1.20484e-3 16 -27 -20 32 imp:p=1

12 5 -1.20484e-3 (23:26) 20 -27 -29 imp:p=1



c whole universe

999 0 27:29:-32 imp:p=0

c \*\*\*\*\*

**c -- Surface cards**

33 cy 0.425 \$ core diameter

34 py 4.58 \$ top plane

1 cy 3.125 \$ Ge crystal

3 py 6.13 \$ top plane

18 py 0.18 \$ bottom plane of Ge

4 cy 3.175 \$ Dead layer

6 py 6.18 \$ top plane

19 py 0.08 \$ bottom plane of Dead layer

10 cy 3.353 \$ vacuum space

2 py 6.53 \$ top plane  
 5 py -0.27 \$ bottom plane  
 7 cy 3.251 \$ Al holder  
 c 9 py 0.01 \$ bottom plane  
 c 11 py 6.34 \$ top plane  
 15 py 7.50 \$ Marinelli  
 16 cy 4.25 \$  
 17 cy 4.43  
 20 py 0.00  
 21 py 7.68  
 22 cy 6.42  
 23 cy 6.60  
 24 py 11.276  
 25 py 13.00  
 26 py 13.18  
 27 cy 8.00  
 29 py 15.00  
 30 cy 3.503 \$Al cryostat  
 31 py 6.68 \$top plane  
 32 py -0.42 \$bottom plane



**c -- Data cards**

mode **p**

c

sdef cel=9 rad=d1 ext=d2 erg=1.4608 axs=0 1 0 par=2

si1 0 13.019 \$ thickness

si2 0.18001 11.276 \$ extent

c

f8:p 1

e0 0 0.001 1463i 1.465

c

```
m1 32000. 1
m3 6000. -0.3844
    1000. -0.0484
    7000. -0.5672
m4 1000. -.00380
    6000. -0.01283
    8000. -.49912
    11000. -0.00668
    12000. -0.01568
    13000. -0.07727
    14000. -0.27906
    19000. -0.02656
    20000. -0.03431
    26000. -0.04469
m5 8000. -0.231781
    7000. -0.755267
    6000. -0.000125
    18000. -0.012827
m6 13000. 1
c
nps 10000000
ctme 60
print
```



Germanium detector and 0.4 Liter Marinelli beaker setup (soil sample)

c

c

c -- **cell cards**

c \*\*\*\*\*

c \*\*\*\*\*Detector\*\*\*\*\*

c \*\*\*\*\*

c Germanium crystal

1 1 -5.323 (33:-18:34) -1 18 -3 imp:p=1

c Core cavity

14 0 -33 18 -34 imp:p=1

c Dead layer

3 1 -5.323 (1:-18:3) -4 19 -6 imp:p=1

c Al holder

4 6 -2.700 (4:-19:6) -7 -6 19 imp:p=1



c Vacuum space

5 0 (7:-19:6) -10 -2 5 imp:p=1

c Al cryostat

13 6 -2.700 (10:2:-5) -30 -31 32 imp:p=1

c \*\*\*\*\*

c \*\*\*\*\*Marinelli Beaker\*\*\*\*\*

c \*\*\*\*\*

c Air between detector and beaker

2 5 -1.20484e-3 (30:31) 32 -16 -15 imp:p=1

c Marinelli beaker

6 3 -1.65 (16:15) -17 20 -21 imp:p=1

7 3 -1.65 (22:-18) 17 -23 20 -25 imp:p=1

8 3 -1.65 -23 25 -26 imp:p=1

c Sample and air inside

9 4 -1.63 17 -22 18 -24 imp:p=1

10 5 -1.20484e-3 -22 24 -25 (17:21) imp:p=1

c Air outside

11 5 -1.20484e-3 16 -27 -20 32 imp:p=1

12 5 -1.20484e-3 (23:26) 20 -27 -29 imp:p=1

c whole universe

999 0 27:29:-32 imp:p=0

c \*\*\*\*\*

**c -- Surface cards**

33 cy 0.425 \$ core diameter

34 py 4.58 \$ top plane

1 cy 3.125 \$ Ge crystal

3 py 6.13 \$ top plane

18 py 0.18 \$ bottom plane of Ge

4 cy 3.175 \$ Dead layer

6 py 6.18 \$ top plane

19 py 0.08 \$ bottom plane of Dead layer

10 cy 3.353 \$ vacuum space



2 py 6.53 \$ top plane

5 py -0.27 \$ bottom plane

7 cy 3.251 \$ Al holder

c 9 py 0.01 \$ bottom plane

c 11 py 6.34 \$ top plane

15 py 7.50 \$ Marinelli

16 cy 4.25 \$

17 cy 4.43

20 py 0.00

21 py 7.68

22 cy 6.42

23 cy 6.60

24 py 6.10

25 py 13.00

26 py 13.18  
27 cy 8.00  
29 py 15.00  
30 cy 3.503 \$Al cryostat  
31 py 6.68 \$top plane  
32 py -0.42 \$bottom plane

**c -- Data cards**

mode **p**

c

sdef cel=9 rad=d1 ext=d2 erg=1.4608 axs=0 1 0 par=2

si1 0 13.019 \$ thickness

si2 0.18001 7.62 \$ extent

c

f8:p 1

e0 0 0.001 1463i 1.465

c

m1 32000. 1

m3 6000. -0.3844

1000. -0.0484

7000. -0.5672

m4 000. -.00380

6000. -0.01283

8000. -.49912

11000. -0.00668

12000. -0.01568

13000. -0.07727

14000. -0.27906

19000. -0.02656

20000. -0.03431

26000. -0.04469



m5 8000. -0.231781  
7000. -0.755267  
6000. -0.000125  
18000. -0.012827  
m6 13000. 1  
c  
nps 10000000  
ctme 60  
print



## Appendix C

### C++ Source Code

The C++ program written for the intercomparison exercise is listed here. The program produces an energy deposition spectrum for a point source of gamma ray (10 keV – 1.2 MeV) in a germanium sphere. The user determines the radius of the sphere, energy and number of the gamma-rays that are to be simulated.

```
#include <iostream.h>
#include <cstdlib>
#include <math.h>
#include <time.h>
#include <fstream.h>
```

```
double main()
```

```
{
```

```
    ofstream try4 ("try4");
    ofstream coordinates ("coordinates");
    ofstream energy ("energy");
    ofstream spectrum ("spectrum");
    ofstream spec2 ("spectrum2");
    ofstream angle ("angle");
```

```
    float E[10], E_gamma[10], tetha[10], phi[10], alpha[10];
    float X_alpha[10], Y_alpha[10], Z_alpha[10];
    float X_origin[10], Y_origin[10], Z_origin[10];
    float r_alpha[10], r_origin[10], X[10], Y[10], Z[10], r[10];
    float E_tot, E_abs, E_sing, sigma, rho, dot_r, mag_prod;
    int sphere_Rad, nsp, i, j, bin;
```





```

int N_bins = 1500;
int E_max = 1500;
int spec_E[N_bins];
int spec_S[N_bins];

const double pi = 3.14159;
cout << " Enter energy of incident gamma-ray less then 1.5 MeV "<<endl;
cin >> E_gamma[0];
cout<< " Enter the radius of the circle "<<endl;
cin >> sphere_Rad;
cout << " Enter number of source particles "<<endl;
cin >> nsp;
cout << " ***** ";
srand((unsigned)time(0));

for (i=0; i<N_bins+1; i++)
    {
        spec_E[i] = 0;
        spec_S[i] = 0;
    }

for (j = 1; j<=nsp; j++)
    {
        X[0] = 0.00;
        Y[0] = 0.00;
        Z[0] = 0.00;
        r[0] = 0.00;
        E[0] = 0.00;

        int n = 1;
        try4 << " Particle "<< j << endl;

```



```

try4 << " Energy of incident photon " << E_gamma[0]<< " MeV"<< endl;
try4 << " Radius of sphere " << sphere_Rad<< " cm"<< endl;
E_gamma[n] = E_gamma[0];

```

```

coordinates <<X[0]<<"      "<<Y[0]<<"      "<<Z[0]<< endl;
float r_tot = 0.0;

```

```

// constants for attenuation curve

```

```

double o = -12.8023;
double p = -11.1733;
double q = 54.76261;
double s = -227.001;
double t = -430.608;
double u = -1603.66;
double v = -171.599;

```



```

// Calculation of attenuation coefficient

```

```

double EG4= pow(E_gamma[n],2.0);
double EG5= pow(E_gamma[n],3.0);
double mu1 = o+(q*E_gamma[n])+(t*EG4)+(v*EG5);
double mu2 = 1+(p*E_gamma[n])+(s*EG4)+(u*EG5);
double mu = mu1/mu2;
try4 << " attenuation coefficient = "<< mu << " cm-1"<<endl;
float vec = (float) rand( ) / RAND_MAX;
double path_l = -log(vec)/mu;
try4 << " path length = "<< path_l << " cm "<< endl;

```

```

// Calculate interaction length
    //float vec = (float) rand( ) / RAND_MAX;
    //float inter_l = vec * path_l;
    //try4 << " interaction length = "<< inter_l << " cm"<< endl;
// insert random function to calculate x and y here

    float tetha1 = (float) rand( ) / RAND_MAX;
    tetha[n-1]= tetha1 * 360;
    // angle<< tetha[n-1]<< endl;
    float phi1 = (float) rand( ) / RAND_MAX;
    phi[n-1] = phi1 * 180;
    // angle<< phi[n-1]<< endl;
    X[n] = X[n-1] + (path_l* sin(phi[n-1])* cos(tetha[n-1]));
    try4 << " x coordinate = "<< X[n] << endl;
    Y[n] = Y[n-1] + (path_l* sin(tetha[n-1])* sin(phi[n-1]));
    try4 << " y coordinate = "<< Y[n] << endl;
    Z[n] = Z[n-1] + (path_l* cos(phi[n-1]));
    try4 << " z coordinate = "<< Z[n] << endl;
    double x_squared = (X[n]*X[n]);
    double y_squared = (Y[n]*Y[n]);
    double z_squared = (Z[n]*Z[n]);
    r[n] = sqrt(x_squared + y_squared + z_squared);
    r_tot = r[n-1] + r[n];
    try4 << " r_tot = "<< r_tot<<endl;

    coordinates <<X[n]<<" "<<Y[n]<<" "<<Z[n]<< endl;

    E_tot = 0;

```

```
while (E_gamma[n] > 0.01 && r[n] < sphere_Rad)
{
```

```
    E_sing = 0;
```

```
    E_abs = 0;
```

```
// constants for probability curve
```

```
double a = 1.018913;
```

```
double b = -1.200447;
```

```
double c = -1.9143239;
```

```
double d = -2.2094495;
```

```
double e = 1.6566923;
```

```
double f = 1.8394588;
```

```
double g = -0.31875457;
```

```
double h = 36.399731;
```



```
// insert probability function for PE here
```

```
double EG1 = pow(E_gamma[n],0.5);
```

```
double EG2 = pow(E_gamma[n],1.5);
```

```
double EG3 = pow(E_gamma[n],2);
```

```
double prob_1 = a+(c*EG1)+(e*E_gamma[n])+(g*EG2);
```

```
double prob_2 = 1+(b*EG1)+(d*E_gamma[n])+(f*EG2)+(h*EG3);
```

```
double prob_PE = prob_1/prob_2;
```

```

// insert random function to calculate sigma
float sigma = (float) rand( ) / RAND_MAX;
try4 << " PE probability = "<< prob_Pe<< endl;
try4 << " Cross Section = "<< sigma << endl;
if (0 < sigma && sigma < prob_Pe)
{
n = n+1;
try4 << "*****" << endl;
try4 << " Photoelectric Effect " << endl;
try4 << "*****" << endl;
E[n-1] = E_gamma[n-1];
try4 << " Energy deposited = "<< E[n-1] << "MeV"<< endl;
energy << " Energy deposited = "<< E[n-1] << endl;
E_gamma[n] = E_gamma[n-1] - E[n-1];

```

// Histogram for energy deposited



```

E_abs = E[n-1] * 1000;
E_tot = E_tot + E_abs;

```

```

if (E_abs > 0.0)
{
bin = (E_abs/E_max) * N_bins;
spec_S[bin] = spec_S[bin] + 1;
}
}
else

```

```

// insert randon function to calculate x and y
{

try4 << "*****" << endl;
try4 << " Compton Scattering " << endl;
try4 << "*****" << endl;

n = n+1;
float tetha1 = (float) rand( ) / RAND_MAX;
tetha[n-1]= tetha1 * 360;
angle<< tetha[n-1]<< endl;
float phi1 = (float) rand( ) / RAND_MAX;
phi[n-1] = phi1 * 180;
angle<< phi[n-1]<< endl;
X_alpha[n-1] = sin(phi[n-1])* cos(tetha[n-1]);
Y_alpha[n-1] = sin(phi[n-1]) * sin(tetha[n-1]);
Z_alpha[n-1] = cos(phi[n-1]);

X_origin[n-1] = sin(phi[n-2])* cos(tetha[n-2]);
Y_origin[n-1] = sin(phi[n-2]) * sin(tetha[n-2]);
Z_origin[n-1] = cos(phi[n-2]);

double dot_X = (X_alpha[n-1]* X_origin[n-1]);
double dot_Y = (Y_alpha[n-1]* Y_origin[n-1]);
double dot_Z = (Z_alpha[n-1]* Z_origin[n-1]);
double dot_r = dot_X + dot_Y + dot_Z;
alpha[n-1] = acos(dot_r);
double s_angle = (alpha[n-1]*360)/(2*pi);
try4 << " scattering angle = "<< s_angle<<" degrees " << endl;
angle<< " scattering angle = "<< s_angle<<" degrees " << endl;
rho = cos(alpha[n-1]);

```

```

angle << rho<< endl;
E_gamma[n] = E_gamma[n-1]/(1+((E_gamma[n-1]/0.511)*(1- rho)));
E[n-1] = E_gamma[n-1] - E_gamma[n];
try4 << " Energy deposited = "<< E[n-1] << " MeV"<< endl;
energy << " Energy deposited = "<< E[n-1] << endl;
try4 << " Energy after scattering = " <<E_gamma[n] <<" MeV"<<endl;

```

```

E_abs = E[n-1] * 1000;

```

```

E_tot = E_tot + E_abs;

```

```

// Histogram for energy deposited

```

```

if (E_abs > 0.0)

```

```

{

```

```

    bin = (E_abs/E_max) * N_bins;

```

```

    spec_S[bin] = spec_S[bin] + 1;

```

```

}

```

```

double o = -12.8023;

```

```

double p = -11.1733;

```

```

double q = 54.76261;

```

```

double s = -227.001;

```

```

double t = -430.608;

```

```

double u = -1603.66;

```

```

double v = -171.599;

```



```
// Calculation of attenuation coefficient
double EG4= pow(E_gamma[n],2.0);
double EG5= pow(E_gamma[n],3.0);
double mu1 = o+(q*E_gamma[n])+(t*EG4)+(v*EG5);
double mu2 = 1+(p*E_gamma[n])+(s*EG4)+(u*EG5);
double mu = mu1/mu2;
try4 << " attenuation coefficient = "<< mu << " cm-1"<<endl;
float vec = (float) rand( ) / RAND_MAX;
double path_l = -log(vec)/mu;
try4 << " path length = "<< path_l << " cm "<< endl;
```

```
// Calculate interaction length
```

```
//float vec = (float) rand( ) / RAND_MAX;
//float inter_l = vec * path_l;
//try4 << " interaction length = "<< inter_l << " cm"<< endl;
```

```
X[n] = X[n-1] + (path_l* sin(phi[n-1])* cos(tetha[n-1]));
```

```
try4 << " x coordinate = "<< X[n] << endl;
```

```
Y[n] = Y[n-1] + (path_l* sin(tetha[n-1])* sin(phi[n-1]));
```

```
try4 << " y coordinate = "<< Y[n] << endl;
```

```
Z[n] = Z[n-1] + (path_l* cos(phi[n-1]));
```

```
try4 << " z coordinate = "<< Z[n] << endl;
```

```
double x_squared = X[n]* X[n];
```

```
double y_squared = Y[n]* Y[n];
```

```
double z_squared = Z[n]* Z[n];
```

```
r[n] = sqrt(x_squared + y_squared + z_squared);
```

```
r_tot = r[n-1] + r[n];
```

```
try4 << " r_tot = "<< r_tot<<endl;
```

```
coordinates <<X[n]<<" "<<Y[n]<<" "<<Z[n]<< endl;
```



```

// return to energy and radius check

    }

}

// Histogram for energy deposited
    bin = (E_tot/E_max) * N_bins;
    spec_E[bin] = spec_E[bin] + 1;

    energy<< "Total Energy deposited " << E_tot<< endl;
    //coordinates << "R_tot " << r_tot<< endl;

    try4 << " ***** " << endl;
}

for (i=0; i< N_bins; i++)
{
    spectrum<< (i+1) << " " << spec_E[i+1]<< endl;
    spec2<< (i+1) << " " << spec_S[i+1]<< endl;
}
}

```



## Appendix D

### Coincidence summing corrections

Garcia-Torano used the MC code, PENELOPE, with a cylindrical geometry tool to model two measurement systems and calculate the photopeak efficiency for liquid volume sources of  $\gamma$  emitters affected by coincidence summing. The radionuclides that were modelled, that is of interest to this study is that of  $^{60}\text{Co}$  and  $^{152}\text{Eu}$ . The efficiency curves shown in Figure A1, show that the correction factors for the nuclides of interest are in the order of 10 % [Tor05], which is in good agreement with the differences in the simulated and experimental data of section 5.1 in this study.

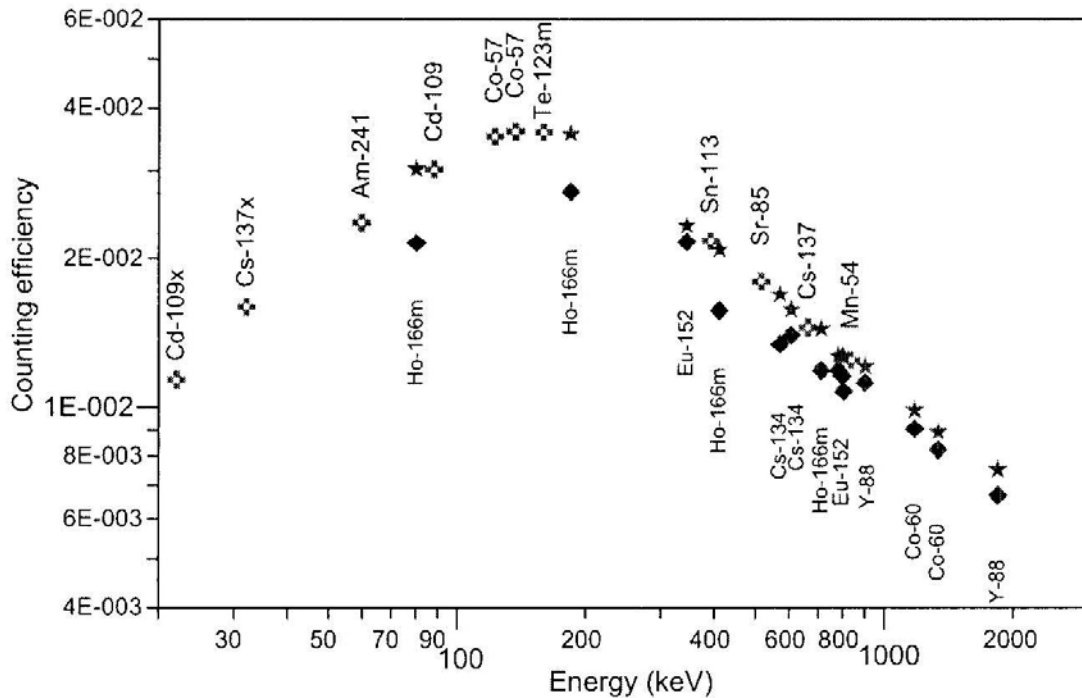


Figure A1: Measured efficiency curves for liquid sources in a 1 litre Marinelli beaker. Crosses correspond to  $\gamma$ -rays lines not affected by coincidence summing and diamonds to the values obtained for  $\gamma$  lines with significant coincidence summing effects. Efficiencies obtained in the simulations for multi- $\gamma$  emitters, corrected by coincidence summing, are represented by stars [Tor05].

## Appendix E

### Efficiency transfer Method

Jurado Vargas used the Monte Carlo code, DETEFF, which was developed by himself and his colleges to calculate the photopeak efficiencies for a HpGe detector in the energy range 60 keV – 2000 keV. The efficiency values were calculated in two ways: (1) by the direct calculation taking into account the physical dimensions of the detector provided by the supplier, and (2) by means of relative computation (efficiency transfer) taking also into consideration the known efficiency values for a reference source. In this work, simulations for two source configurations (point source and cylindrical source) were made for several discrete values in the energy range 60 keV – 2000 keV (60, 80, 100, 150, 200, 500, 1000, 1500 and 2000 keV).

#### E.1 Reference point source



The efficiency values for a point source measured at 10 cm source to detector window distance, using the detector dimensions given by the supplier was computed as a reference geometry. The experimental and calculated efficiencies showed significant discrepancies of greater than 10 %, especially for the 60 keV photons and for the high-energy photons (1000 keV – 2000 keV). The efficiency values for point sources located at 2 cm, 5 cm and 20 cm from the detector window in the same way as performed for the reference point (direct computation with the data obtained from the supplier) was also computed. The deviations found at these distances followed the same trend as obtained in the simulation of the reference source at 10 cm. However in the case of the 20 cm point source, the deviations reached as high as 20 % for the 2000 keV photons.

A efficiency transfer from the reference point source to the point sources at the different distances for a given energy in the geometry of interest was performed with the use of the following equation:

$$\epsilon_i = \epsilon_r \left( \frac{S_i}{S_r} \right)$$

where  $\epsilon_i$  is the efficiency in the geometry of interest,  $\epsilon_r$  the known experimental efficiency for the reference point source,  $S_i$  and  $S_r$  denotes the computed efficiency for the geometry of interest and for the reference geometry, respectively. The results show that the efficiency transfer from a reference point source, using Monte Carlo simulations, reproduces adequately the detection efficiencies for the point source at all the distances considered in this work to less than 5 % from experimental data.

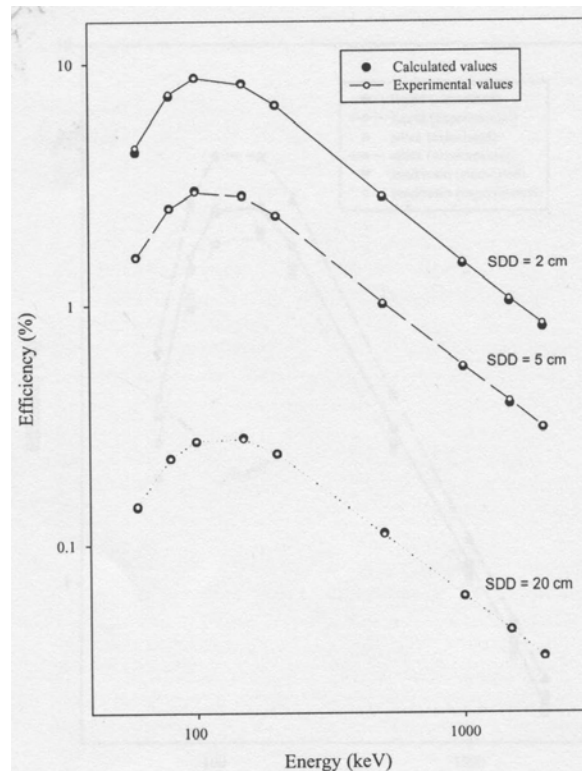


Figure A2: Results of the efficiency transfer for the point sources located at 2cm, 5 cm, and 20 cm from the detector window [Var03]

## E.2 Cylindrical samples

Simulations were also performed for the cylindrical sources, which included three matrices; low-density silica ( $\rho = 0.25 \text{ g/cm}^{-3}$ ), liquid ( $1.016 \text{ g.cm}^{-3}$  hydrochloric acid solution), and a sand/resin mixture ( $\rho = 1.54 \text{ g.cm}^{-3}$ ) in cylindrical vials. The peak efficiencies for these geometries were computed in the same way as for the point sources, but now the photon attenuation in each matrix and in the vial walls was also considered. The results of the direct computation showed significant deviations with respect to experimental values for the three cylindrical geometries and showed similar behaviour to that shown by the point sources. For example, in the case of the sand/resin sample the relative deviation between simulated and experimental values were greater than 20 % for the photons of 60 keV, 1500 keV and 2000 keV.

The results obtained by performing the efficiency transfer (in the same manner as for the point sources) from the reference geometry to the three cylindrical matrices, showed reasonably good agreement with the experimental efficiencies. The deviations between simulated and experimental values were found to be below 5 %.

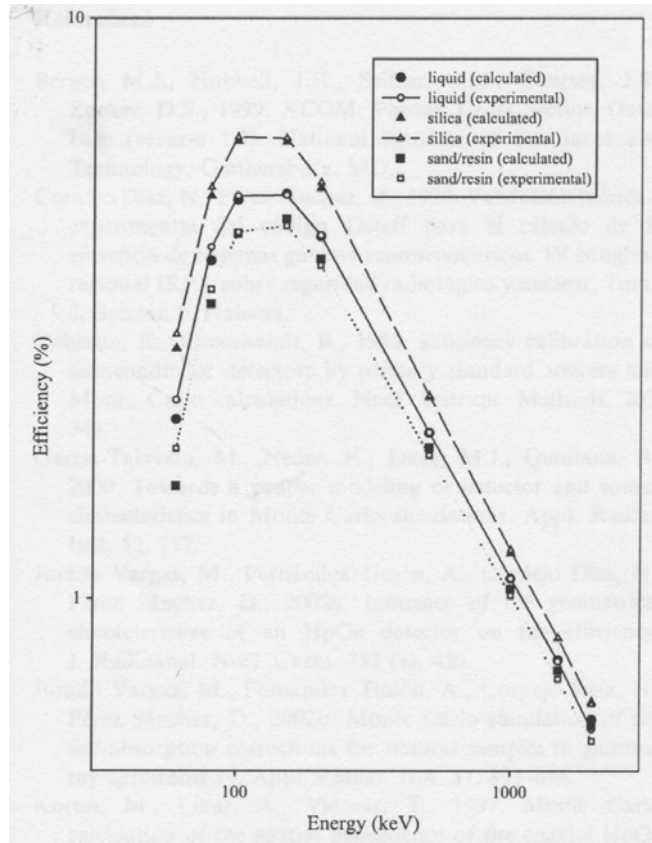


Figure A3: Results of the efficiency transfer for the cylindrical sources [Var03].

## References:

- [Ame00] Amersham QSA catalogue, (2000).
- [Bea78] Beam G.B., Wielopolski L., Gardner R.P., Monte Carlo calculation of  $\varepsilon$  of right – circular cylindrical NaI detectors for arbitrarily located point sources, Nuclear Instrumentation and Methods 154 (1978), pp. 501 – 508 .
- [Bei95] Beiser A., Concepts of Modern Physics, 5th Ed., McGraw – Hill (1995).
- [Can99] Canberra Detector specification and performance data sheet supplied with the detector user's manual, (1999).
- [Cle94] Van Cleef D.J., Determination of  $^{226}\text{Ra}$  in soil using  $^{214}\text{Pb}$  and  $^{214}\text{Bi}$  immediately after sampling, Health Physics 67 (1994), pp. 288.
- [Cro99] Croft S., Hutchinson I.G., The measurement of U, Th and K concentrations in building materials, Applied Radiation and Isotopes 51 (1999), pp. 483.
- [Deb82] Debertin K., Grosswendt B., Efficiency calibration of semiconductor detectors by primary standard sources and Monte Carlo calculations, Nuclear Instrumentation Methods in Physics Research A203 (1982), pp. 343.
- [Deb89] Debertin K., Jianping R., Measurement of the activity of radioactive samples in Marinelli beakers, Nuclear Instrumentation and Methods in Physics Research A278 (1989), pp. 541 – 549.
- [Dec92] Decombaz M., Gostely J.J., Laedermann J.P., Coincidence – summing corrections for extended sources in gamma-ray spectrometry using Monte Carlo simulations, Nuclear Instrumentation Methods in Physics Research A312 (1992), pp.152.
- [Eva55] Evans R. D., The Atomic Nucleus, McGraw – Hill Book Company, Inc (1955), pp. 672-711.

- [Ewa01] Ewa I.O.B., Bodizs D., Czifrus Sz., Molnar Zs., Monte Carlo determination of full energy peak efficiency for a HPGe detector, *Applied Radiation and Isotopes* 55 (2001), pp. 103 – 108.
- [Fir96] Firestone R.B., Chu S.Y.F., Baglin C.M., and Zipkin J., *Table of Isotopes*, (Ed. Shirley V.S), John Wiley and Sons, New York (1996).
- [Gar00] Garcia – Talavera M., Neder H., Daza M.J., Quintana B., Towards a proper modelling of detector and source characteristics in Monte Carlo simulations, *Applied Radiation and Isotopes*, Vol. 52 (2000), pp. 777 – 783.
- [Gar01] Garcia – Talavera M., Laedermann J.P., Decombaz M., Daza M.J., Quintana B., Coincidence summing corrections for the natural decay series in  $\gamma$  – ray spectrometry, *Applied Radiation and Isotopes*, Vol. 54 (2001), pp. 769 – 776.
- [Gar71] Garrels R.M., Mackenzie F.T., *Evolution of Sedimentary Rocks*, Norton, John Wiley & Sons, New York (1971).
- [Gil95] Gilmore G., Hemingway J.D., *Practical Gamma – Ray Spectrometry*, John Wiley & Sons, New York (1995).
- [Hen00] Hendricks J.S., Adams K.J., Booth T.E., Briesmeister J.F., Present and future capabilities of MCNP, *Applied Radiation and Isotopes*, Vol. 53 (2000), pp 857 – 861.
- [Hen01] Hendriks P.H.G.M., Full – spectrum analysis of natural  $\gamma$  – ray spectra, *Journal of Environmental Radioactivity* 53 (2001), pp. 365.
- [Hen02] Hendricks P.H.G.M., Maučec M., de Meijer R.J., MCNP modelling of scintillation – detector  $\gamma$  – ray spectra from natural radionuclides, *Applied Radiation and Isotopes* 57 (2002), pp. 449 – 457.
- [Hen03] Hendriks P.H.G.M., In – depth  $\gamma$  – ray studies – Borehole measurements, University of Groningen, PH.D Thesis (2003), pp 62 – 63, 69 – 71.



- [Hub82] Hubbell J. H., Photon Mass Attenuation and Energy – absorption coefficients from 1 keV to 20 MeV, International Journal of Applied Radiation and Isotopes, Vol. 33 (1982), pp. 1269-1290.
- [Iso98] Isotrak Catalogue, Calibration standards and Instruments for measuring radioactivity, 2<sup>nd</sup> edition (1998).
- [Gon01] Gonzalez J.E., Simulation of Highly segmented HPGe Detectors, Michigan State University, REU Summer Research Project (2001).
- [Jos05] Joseph A. D., Radiometric Study of Soil: The Systematic Effect, forthcoming Masters Thesis, University of the Western Cape (2005).
- [Kno79] Knoll G. F., Radiation Detection and Measurement, John Wiley & Sons (1979), pp. 63 – 70, 92 – 95, 308-313.
- [Kra88] Krane K.S., Introductory Nuclear Physics, John Wiley & Sons, New York (1988) , pp198 – 204.
- [Lab00] Laborie J.M., Le Petit G., Abt D., Girarad M., Monte Carlo calculations of the efficiency calibration curve and coincidence – summing corrections in low – energy gamma – ray spectrometry using well – type HPGe detectors, Applied Radiation and Isotopes 53 (2000), pp. 57 – 62.
- [Leh51] Lehmer D.H., Ralston A., Wilf H.S., Mathematical methods for Digital Computers, Vol. 2, John Wiley & Sons, New York (1951), pp. 249 – 263.
- [Lin79] Lindsay, W.L., Chemical equilibra in soils, Wiley & Sons, New York (1979).
- [Man01] MCNP4C User's Manual, Radiation Safety information Computational Centre, Los Alamos Laboratory, Los Alamos, New Mexico, April 2000.
- [Map05] Maphoto K.P., Determination of Natural Radioactivity Concentrations in Soil: a comparative study of Windows and Full Spectrum Analysis, Masters Thesis, University of the Western Cape (2005), unpublished.

- [Mar50] Marinelli L.D., Hine G.J. and Hill R.F., The Quantitative Determination of Gamma Radiation in Biological Research, Am. J. Roentg. and Radium Therapy, February 1950, pp. 160.
- [Met56] Metropolis N., Meyer H.A., Symposium on Monte Carlo Methods, John Wiley & Sons, New York (1956), pp. 29 – 36.
- [Mod05] Modisane T.J.D., Correlation between Natural radionuclide concentrations in soil and vine – yard growth, Masters Thesis, North West University (2005), unpublished.
- [Mor02] Morris W.M., Simpson B.R.S., CSIR mixed radionuclide source, Certificate of Measurement, RS\02 – 2, CSIR National Metrology Laboratory, Cape Town (2002).
- [Ove93] Overwater M.W., Bode P., de Goeij J., Gamma – ray spectroscopy of voluminous sources: corrections for source geometry and self – attenuation, Nuclear Instrumentation Methods in Physics Research A390 (1993), pp. 203.
- [Rig02] Rigollet C., de Meijer R.J., PHAROS: A pluri – detector, high – resolution, analyser of radiometric properties of soil, Nuclear Instrumentation Methods in Physics Research (Sect. A), in press.
- [Ron02] Keyser R. M., Hensley W.K., Efficiency and Resolution of Germanium Detectors as a Function of Energy and Incident Geometry, New Product Development, ORTEC, 801 South Illinois Avenue, Oak Ridge, TN 37831 (2002).
- [Sán91] Sánchez F., A Monte Carlo based method of including gamma self-absorption for the analysis of environmental samples, Nuclear Instrumentation Methods in Physics Research A188 (1991), pp. 133.
- [Sim92] Sima O., Photon Attenuation for samples in Marinelli Beaker Geometry: An Analytical Computation, Health Physics 62 (5) (1992), pp. 445.
- [Sto70] Storm E. and Israel H.I., Nuclear Data Tables A7 (1970), pp. 565 – 681.

- [Tyk95] Tykva R., Sabol J., Low Level Environmental Radioactivity Sources and Evaluation, Technomic Publishing Company, Lancaster, Pennsylvania (1995).
- [Tor05] Garcia – Torano E., Pozuelo M., Salvat F., Monte Carlo calculations of coincidence summing corrections for volume sources in gamma – ray spectrometry with Ge detectors, Nuclear Instrumentation Methods in Physics Research A544 (2005), pp. 577 – 583.
- [Var03] Vargas M. J., Diaz N. C., Sanchez D. P., Efficiency transfer in the calibration of a coaxial p – type HpGe detector using the Monte Carlo method, Applied Radiation and Isotopes, Vol. 58 (2003), pp. 707 – 712.

Other:

[WWW01] <http://www.yale.edu/lawweb/avalon/abomb/mp01.htm>.

[WWW02] <http://csep1.phy.ornl.gov/mc/node1.html>.

